COMPUTATIONAL STUDIES OF LIPID OXIDATION AND SIGNALING

by

Dariush Mohammadyani

B.S. in Materials Science, Amirkabir University of Technology, Tehran, Iran, 2005

M.S. in Materials Science, University of Tehran, Tehran, Iran, 2008

M.S. in Bioengineering, University of Pittsburgh, Pittsburgh, USA, 2014

Submitted to the Graduate Faculty of

Swanson School of Engineering in partial fulfillment

of the requirements for the degree of

Doctor of Philosophy in Bioengineering

University of Pittsburgh

2016

UNIVERSITY OF PITTSBURGH

SWANSON SCHOOL OF ENGINEERING

This dissertation was presented

by

Dariush Mohammadyani

It was defended on

February 18th, 2016

and approved by

Ivet Bahar, Ph.D., Professor, Department of Computational and System Biology

Hulya Bayir, Ph.D., Professor, Department of Critical Care Medicine

Bruce Pitt, Ph.D., Professor, Department of Environmental and Occupational Health

Partha Roy, Ph.D., Associate Professor, Departmental of Bioengineering

Patrick van der Wel, Ph.D., Assistant Professor, Department of Structural Biology

Dissertation Advisors: Valerian E. Kagan, Ph.D., Professor, Department of Environmental and Occupational Health

Judith Klein-Seetharaman, Ph.D., Professor, Division of Metabolic and Vascular Health, University of Warwick

COMPUTATIONAL STUDIES OF LIPID OXIDATION AND SIGNALING

Dariush Mohammadyani, Ph.D.

University of Pittsburgh, 2016

Introduction: Lipid signaling refers to events involving lipid messengers that bind proteins, which in turn mediate the effects of these lipids on specific cellular responses. The identification of lipid messengers and mechanisms of their interactions with the target proteins are the main pillars of understanding lipid signaling. Lipids function as signals in two ways: (i) chemical modifications of lipids, and (ii) asymmetric distribution of lipids.

Methodology: We utilized computational approaches, including molecular docking, molecular dynamics simulations and bioinformatics, to explore the mechanism of lipid signaling in several cellular pathways.

Oxygenated (ox-)lipid signaling in anti-cancer immunity: Oxygenation is the major metabolic modification generating numerous new molecular species of lipids, which can be involved in signaling processes. The structural role of ox-lipids in lipid droplets (LDs) present in tumor environments was examined. The presence of polar oxygenated functional group(s) in oxygenated lipids (ox-lipids) resulted in to their localization in the LD surface. We then explored possible interactions of ox-lipids with the heat shock protein 70 (HSP70), one of the key-proteins in antigen-cross presentation. Our data revealed that HSP70 specifically recognizes the neutral ox-lipids on the LD surface leading to tight binding and deep penetration into the phospholipid monolayer of the LD.

Lipoxygenase-driven phospholipid peroxidation signaling: we explored the catalytic and inhibition mechanisms of lipoxygenases (LOX's), the main generators of ox-lipids in ferroptosis cell death. We revealed the mechanism of peroxidation of esterified fatty acid via LOX's and provided a possible mechanism of inhibition of LOX's, particularly by vitamin E's.

Lipid signaling due to asymmetric distribution of cardiolipin: The mitochondrial signature phospholipid, cardiolipin (CL), is asymmetrically distributed in the inner mitochondrial membrane. CL asymmetry is disrupted through a process called "CL externalization", which can be recognized by many proteins. We described the molecular details of cardiolipin interactions with cytochrome c and LC3, the key players of apoptosis and mitophagy pathways, respectively. The CL-binding site(s) on these proteins were identified. Our data suggested that the strong interactions of cyt-c/LC3 with CL-containing membranes lead to CL clustering. This clustering in turn induces a negative curvature on the membrane surface.

TABLE OF CONTENTS

LIST OF TABLES

LIST OF FIGURES

ABBREVIATION

AA	Arachidonic acid
ACP	Antigen cross-presentation
ACSL4	Acyl-CoA synthase
AdrA	Adrenic acid
CGMD	Coarse-grained molecular dynamics
ChE	Cholesterol ester
CL	Cardiolipin
COM	Center of mass
Cyt-c	Cytochrome c
DC	Dendritic cell
DHA	Docosahexaenoic acid
DMPC	1,2-Dimyristoyl-sn-glycero-3-phosphocholine
DOPC	1,2-Dioleoyl-sn-glycero-3-phosphocholine
DSC	Differential scanning calorimetry
EPA	Eicosapentaenoic acid
FFA	Free fatty acids
GPX4	Glutathione peroxidase 4

HSP70	Heat shock protein 70
IMM	Inner mitochondrial membrane
LAXA	Low-angle X-ray scattering
LC3	Microtubule-associated protein 1 light chain 3
LD	Lipid Droplet
LOX	Lipoxygenase
MD	Molecular dynamics
NDPK-D	Nucleoside diphosphate kinase - D
OMM	Outer mitochondrial membrane
PA	Phosphatidic acid
PC	Phosphatidylcholine
PE	Phosphatidylethanolamine
PG	Phosphatidylglycerol
PI	Phosphatidylinositol
PL	Phospholipid
PLAT	Polycystin-1, LOX, Alpha-Toxin
PS	Phosphatidylserine
PS	Phosphatidylserine
PUFA	Poly-unsaturated fatty acids
ROS	Reactive oxygen species
TAG	Triacylglycerol
TLCL	Tetra-linoleoyl-CL
TMCL	Tetra- myristoyl -CL

TOCL	Tetra-oleoyl-CL

ACKNOWLEDGEMENTS

I would like to acknowledge my advisors, Dr. Judith Klein-Seetharaman and Dr. Valerian E. Kagan, for their constant support, and encouragement throughout this process. They provided an opportunity for me to apply my computational skills to study the significant and challenging biophysical questions in several lipid signaling pathways.

I would like to extend my thanks to Prof. Sanjeev Shroff, Chair, Prof. William Federspiel, Graduate Chair and Prof. Parta Roy, Biophysics track Director of Bioengineering Department. I am thankful to Nick Mance for his quick responses and patience as a Graduate Coordinator of Bioengineering Department. Moreover, I appreciate the collaboration of Dr. Klein-Seetharman and Dr. Kagan: Dr. Bayir, Dr. Bahar, Dr. van der Wel, Dr. Schluttner, Dr. Conrad, Dr. Gabrilovich and Dr. Sadovsky. Thank you to all my colleagues and friends in both laboratories. I acknowledge Dr. Balasubramanian, Dr. Sparvero, Dr. Maguire, Dr. Amoscato, and Ms. Clark, who kindly helped me in editing the text.

Finally, I would like to thank my mother with deep appreciation for her inspiration and motivation in every aspect of my life. Also, many thanks to my lovely son, Cyrus. Indeed, his cute smile and inspiring personality mitigated the hardships during this path. Last but not least, I whole-heartedly thank my beautiful wife, Zolfa, for her constant love, support and ALWAYS being there for me. I dedicate my Ph.D. dissertation to Zolfa, my soul mate and beautiful wife, Cyrus, my lovely son, and my Mother and memory of my Father.

JOURNAL PUBLICATIONS

Parts of this thesis have been published in below journal articles:

1. **Mohammadyani D.**, Tyurin V.A., Sadovsky Y., Gabrilovich D.I., Klein-Seetharaman J., Kagan V.E., Molecular speciation and dynamics of oxidized triacylglycerols in lipid droplets: Mass spectrometry and coarse-grained simulations, Free Radical Biology and Medicine, 76, 53-60 (2014).

2. Planas-Iglesias J., Dwarakanath H., **Mohammadyani D.**, Yanamala N., Kagan V.E., Klein-Seetharaman J., Cardiolipin interactions with proteins, Biophysical Journal, 109 (6), 1282-1294 (2015).

3. Balasubramanian K., Maeda A., Lee J.S., **Mohammadyani D.**, Dar H., Jiang J.F., Croix C.M.S., Vatkins S., Tyurin V., Tyurina Y.Y., Klöditz K., Polimova A., Kapralova V.I., Xiong Z., Ray P., Klein-Seetharaman J., Mallampalli R.K., Bayir H., Fadeel B., Kagan V.E., Dichotomous roles for externalized cardiolipin in extracellular signaling: Promotion of phagocytosis and attenuation of innate immunity, Science Signaling, 8 (395), 1-13 (2015).

4. Barneda D., Planas-Iglesias J., Gaspar M.L., **Mohammadyani D.**, Prasannan S., Dormann D., Han G., Jesch S.A., Carman G.M., Kagan V.E., Parker M.G., Ktistakis N.T., Dixon A.M., Klein-Seetharaman J., Henry S., Christian M., The brown adipocyte protein CIDEA promotes lipid droplet fusion via a phosphatidic acid-binding amphipathic helix, eLife, 4, 1-24 (2015).

5. Kagan V.E., Tyurina Y.Y., Tyurin V., **Mohammadyani D.**, Angeli J.P.F., Baranov S.V., Klein-Seetharaman J., Friedlander R.M., Mallampalli R.K., Conrad M., Bayir H., Cardiolipin signaling mechanisms: collapse of asymmetry and oxidation, Antioxidants & Redox Signaling, 22(18) 1667-1680 (2015).

6. Tyurina Y.Y., Poloyac S.M., Tyurin V.A., Kapralov A.A., Jiang J., Anthonymuthu T.S., Kapralova V.I., Vikulina A.S., Jung M., Epperly M.W., **Mohammadyani D.**, Klein-Seetharaman J., Jackson T.C., Kochanek P.M., Pitt B.P., Greenberger J.S., Vladimirov Y.A.,

Bayır H., Kagan V.E., A mitochondrial pathway for biosynthesis of lipid mediators, Nature Chemistry, 6, 542–552 (2014).

7. Boscia, A.L., Treece, B.W., **Mohammadyani D.**, Klein-Seetharaman, J., Braun, A.R., Wassenaar, T.A., Klösgen, B., Tristram-Nagle, S., X-ray structure, thermodynamics, elastic properties and MD simulations of cardiolipin/dimyristoylphosphatidylcholine mixed membranes, Chemistry and Physics of Lipids, 178, 1–10 (2014)

8. Chu, C.T., Ji, J., Dagda, R.K., Jiang, J.F., Tyurina, Y.Y., Kapralov, A.A., Tyurin, V.A., Yanamala, N., Shrivastava, I.H., **Mohammadyani D.**, Wang, K.Z.Q., Zhu, J., Klein-Seetharaman, J., Balasubramanian, K., Amoscato, A.A., Borisenko, G., Huang, Z., Gusdon, A.M., Cheikhi, A., Steer, E.K., Wang, R., Baty, C., Watkins, S., Bahar, I., Bayır, H., Kagan, V.E, Cardiolipin externalization to the outer mitochondrial membrane acts as an elimination signal for mitophagy in neuronal cells, Nature Cell Biology 15, 1197–1205 (2013).

9. Cao, W., Ramakrishnan, R., Tuyrin, V.A., Veglia, F., Condamine, T., Amoscato, A., **Mohammadyani D.**, Johnson, J.J., Zhang, L.M., Klein-Seetharaman, J., Celis, E., Kagan, V.E, Gabrilovich, D.I., Oxidized lipids block antigen cross-presentation by dendritic cells in cancer: oxidized lipids and DCs in cancer, Journal of Immunology, 192 (10), 4935-4935 (2014).

10. Schlattner, U., Tokarska-Schlattner, M., Ramirez, S., Tyurina, Y.Y., Amoscato, A.A., **Mohammadyani D.**, Huang, Z., Jiang, J., Yanamala, N., Seffouh, A., Boissan, M., Epand, R.F., Epand, R.M., Klein-Seetharaman, J., Lacombe, M., Kagan, V.E, Dual function of mitochondrial Nm23-H4 protein in phosphotransfer and intermembrane lipid transfer: a cardiolipin-dependent switch, Journal of Biological Chemistry, 288:111-121 (2013).

1.0 CHAPTER 1: INTRODUCTION

1.1 BACKGROUND

1.1.1 Lipidome and Lipid Diversity

According to the International Lipid Classification and Nomenclature Committee, lipids are described as "hydrophobic or amphipathic small molecules that may originate entirely or in part by carbanion-based condensations of thioesters (fatty acyls, glycerolipids, glycerophospholipids, sphingolipids, saccharolipids, and polyketides) and/or by carbocation-based condensations of isoprene units (prenol lipids and sterol lipids) [1]." These eight lipid classes are further subdivided based on chemical structures. Although structurally lipids are apparently composed of limited number of 'building blocks', they potentially can generate 9,000–100,000 various molecular species [2]. The totality of lipids in cells is referred as the lipidome [3].

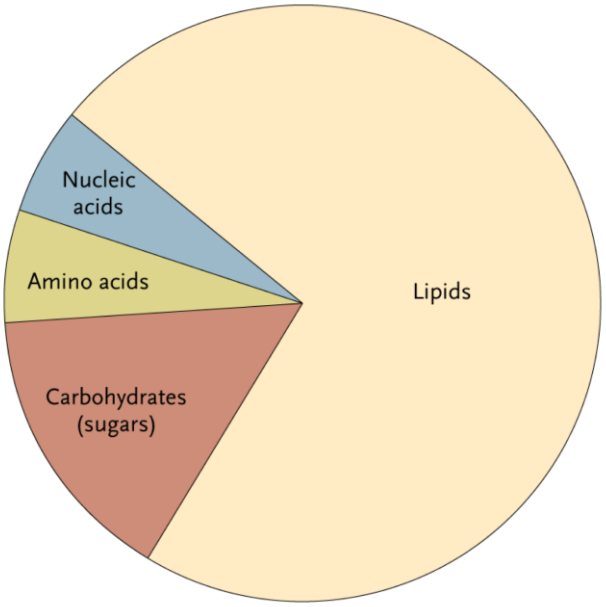

Figure 1-1 Relative distribution of lipids comparing other biological building blocks in human plasma. Amino acids and nucleic acids are demonstrated without consideration of their contribution in proteins and DNA/RNA. The relative distribution is based on weight (grams per deciliter) (adapted from [3]).

Lipids are one of the four major molecular components of the metabolome, along with nucleotides, sugars and amino acids (Figure 1-1). Lipids represent more than 60% in the relative weight distribution of the metabolome's components. The word "lipidome" has been coined in the context of omics in modern biology, within the area of lipidomics [4].

1.1.2 Lipid Signaling

Lipids have many key roles enabling them to function as energy storage compartments, structural moieties and signaling molecules [4]. Although the role of lipids in energy storage systems and structural organization have been widely explored for a long time, the role of lipids in cellular signaling pathways still is an open area to study. Lipid signaling refers to events involving lipid messengers that bind proteins/enzymes, which in turn mediate the effects of these lipids on specific cellular responses [5]. Accordingly, the identification of lipid messengers and the mechanisms of their interactions with target proteins are the key focal points in understanding the lipid signaling. In general, there are two ways that lipids function as signals: (i) via collapse of asymmetric distribution, and (ii) via chemical modification [6].

1.1.2.1 Asymmetric distributions of lipids

Lipid asymmetry is a general property of biological membranes. The type of asymmetry can vary from one membrane to another [7]. The maintenance of this asymmetry and its disturbances are used for signaling purposes. For example, in the plasma membrane, phosphatidylserine (PS) is exclusively located at the cytoplasmic side. However, the externalization of PS on the plasma

membrane of the apoptotic cell acts as a recognition signal for macrophages [8]. The asymmetrical distributions are typically pronounced in cases of cardiolipin (CL)-containing membranes as well. The mitochondrial signature phospholipid (PL), CL, possesses four acyl chains instead of two and is a universal component of mitochondria in all eukaryotes [9, 10]. In addition to trans-membrane asymmetry, CLs also display molecular asymmetry. The latter is due to the chirality of the CL molecule. Even apparently structurally symmetrical CL species with identical fatty acid residues such as tetra-linoleoyl-CL or tetra-oleoyl-CL have two chemically distinct phosphatidyl moieties, i.e., two chiral centers in the pro-R and pro-S positions relative to the central carbon of the glycerol bridge. The potential role of this difference in the ionization states of CLs in the microenvironment facing the mitochondrial matrix, which exhibits a basic pH, may be quite significant [11]. It is tempting to speculate that this propensity of CLs may be responsive to changes in intra-mitochondrial pH/membrane potential which affect CL distribution and trans-membrane asymmetry. For CL species with non-identical acyls, the molecular asymmetry may lead to even more "dramatic" consequences resulting not only in structural "fitness" to accommodate the optimal conformations of the CLs bound to proteins but also in altered metabolic fate realized via (per)oxidation and hydrolysis reactions and accumulation of oxidatively modified CL species and lyso-CLs [10].

In bacteria and in eukaryotes, the cellular distribution of CLs is asymmetric. Normally, CLs are found predominantly in the inner membranes of bacterial cells [12, 13]. It is known that accumulation of CL at the poles of bacteria induce negative curvature, which is analogous to the curved region of cristae in the inner mitochondrial membrane (IMM). Coarse-grained molecular dynamics simulations proved that asymmetric distribution of CL between leaflets of a bilayer induces negative curvature on the CL enriched-side (Figure 1-2).

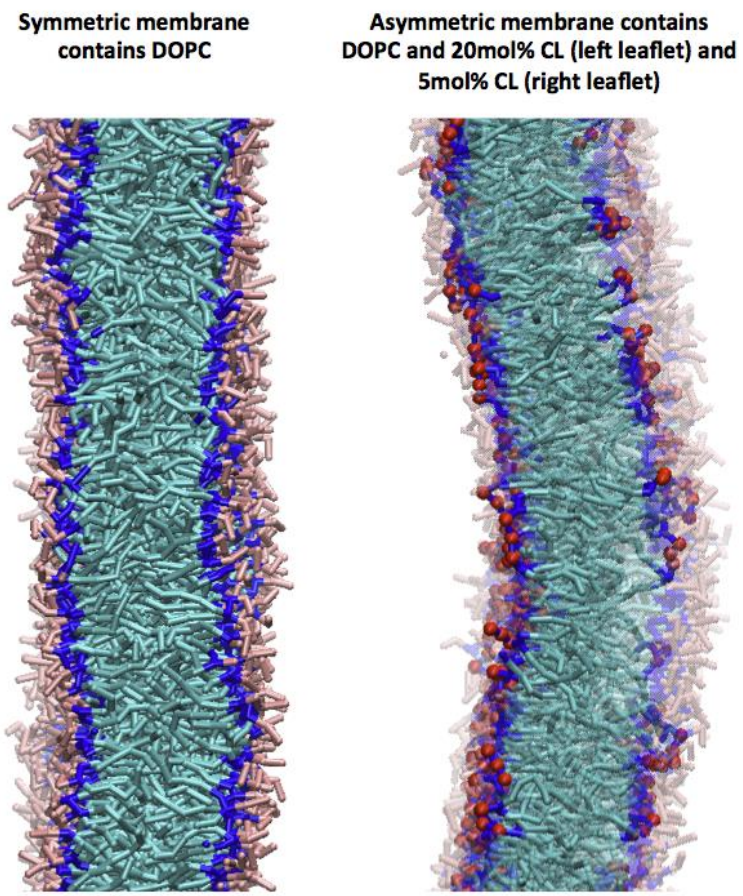

Figure 1-2 Asymmetric distribution of CL between two leaflets induces membrane curvature, characteristic of the IMM and bacterial poles.

The final configuration (at t=500 ns) of CGMD simulations from the symmetric distribution of DOPC in the membrane **(left)** does not display significant curvature, while the asymmetric insertion of CL **(right)** leads to a substantial negative curvature toward the CL enriched side. Representation guide: pink, choline and phosphate groups of DOPC; cyan, acyl chains of CL and DOPC; blue, glycerol moiety of DOPC and CL; red, phosphate groups of CL; DOPCs have been represented as transparent in the asymmetric membrane; water and ions have been removed for clarity. CGMD, coarse-grained molecular dynamics simulations; DOPC, 1,2-dioleoyl-sn-glycero-3-ethylphosphocholine; IMM, inner mitochondrial membrane [14].

In eukaryotes, this asymmetry is even more robust: CLs are mitochondria-specific and, in functional mitochondria maintaining a "healthy" membrane potential, CLs are confined almost exclusively to the inner mitochondrial membrane (IMM) with a higher abundance in the matrix leaflet [15]. Indeed, recent studies have revealed that both in bacteria and in mitochondria, the collapse of CL asymmetry represents a signaling event. The exact meaning of this signaling and its significance for bacteria/host interactions have not yet been fully deciphered [16-18] although

biochemical mechanisms involved in CL translocation have been partially identified [19, 20]. It has been demonstrated that gram-negative bacteria externalize their CLs on the membrane surface as they encounter host cells [20].

This asymmetry has been used as an important recognition mechanism to distinguish the healthy mitochondria —capable of maintaining the CL trans-membrane gradient— from injured organelles where this asymmetry is collapsing. This results in CL externalization on the surface of mitochondria, recognition of CLs by components of the autophageal system (LC3) and elimination of the damaged mitochondria, analogous to the recognition of externalized phosphatidylserine on the cell surface for elimination by professional phagocytes (Figure 1-3). Diversification of CLs in eukaryotic cells yielded multiplicity of its polyunsaturated species whose oxidation may serve additional signaling purposes. Indeed, peroxidation of CLs and accumulation of oxCLs is essential for the completion of the cell death program, thus offering new opportunities for drug discovery. Our understanding of mitochondrial functions – in addition to being a powerhouse of cells – is currently extended to a concept of their role as a major regulatory platform involved in numerous intra- and extracellular functions, from coordination of metabolism and cell death to immune responses in which CLs/oxCLs are considered as important signaling molecules. There is an intuitive perception that the remarkably diversified CLs/oxCLs species in eukaryotes relative to prokaryotes may represent a unique mitochondrial communication language. The biochemical and signaling principles of this language, its vocabulary and meaning of its words are yet to be deciphered.

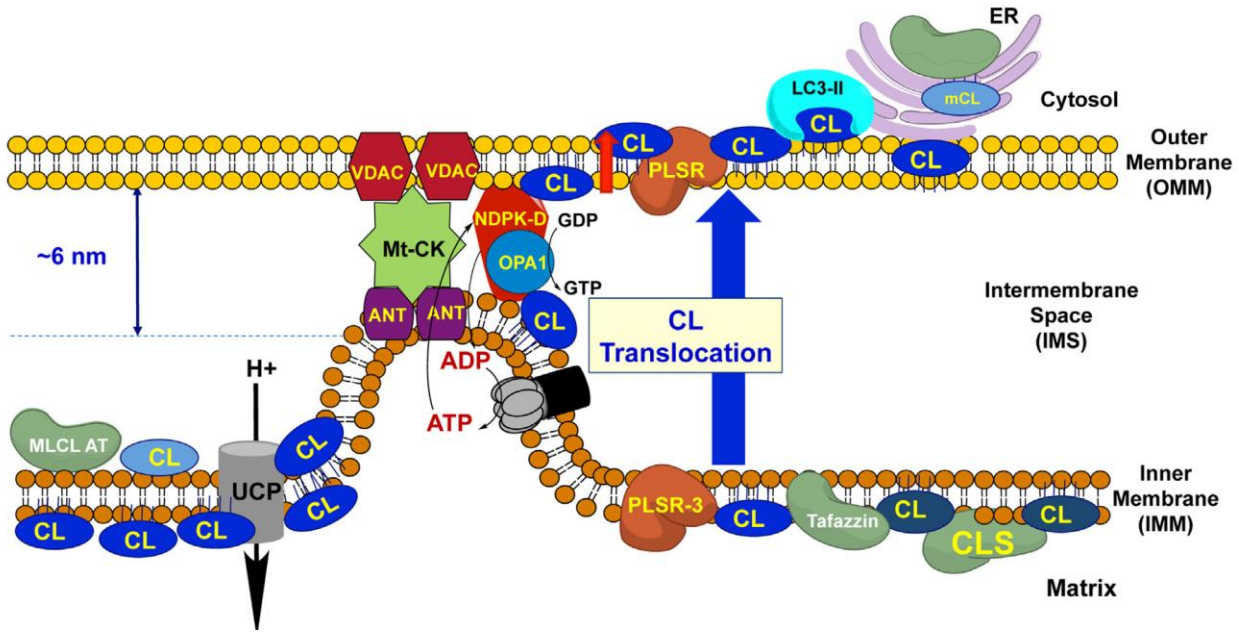

Figure 1-3 Mitophagic translocation of cardiolipin: cardiolipin (CL) is synthesized by cardiolipin synthase (CLS) in the inner leaflet to of the IMM.

Externalization of cardiolipin to the mitochondrial surface through a mechanism involving phospholipid scramblase-3 (PLS3) is a prerequisite for its recognition by LC3 as a mitophagic "eat-me signal" that targets dysfunctional mitochondria to the autophagosomal machinery. Nucleoside diphosphate kinase (NDPK-D) may physically facilitate CL trans-membrane transfer. NDPK-D regulates the balance between di- and tri-phospho-nucleotides, providing GTP for the GTPase activity of OPA1. By forming a hexamer in the intermembrane space, NDPK-D can physically bridge the IMM and OMM. The switch from a phosphotransfer to a cardiolipin-translocator would thus facilitate the redistribution of cardiolipins between the IMM and the OMM (adapted from [21]).

1.1.2.2 Lipid modifications

In addition to an already broad spectrum of different lipids, further diversification is achieved through chemical modification, mainly oxygenation, of free/esterified poly-unsaturated fatty acids (PUFA's) [10]. Correspondingly, both free and esterified oxygenated lipid (ox-lipid) species can be involved in the signal transduction processes by interacting with target proteins/enzymes. The presence of one or more very polar oxygenated groups in the structure of

ox-lipids induces a significant change in the LogP (the partition coefficient). Hence, ox-lipids can change the lipid partitioning, and consequently the structure of lipid-containing compartments such as lipid membranes and lipid droplets (LDs).

In a lipid bilayer, it has been documented that the truncated oxidized sn-2 fatty acid moiety protrudes into the aqueous phase, rendering it accessible for recognition by various proteins, e.g CD36 [22]. The addition of a polar oxygenated group on numerous peroxidized fatty acids reorients the acyl chain, whereby it flips out of the membrane and protrudes into the aqueous compartment, which is called the "lipid Whisker model" (Figure 1-4) [22]. Additionally, lipid oxidation can affect the membrane fluidity. It has been shown that a highly oxidized membrane is susceptible to losing its integrity [22].

While presence of ox-lipids in LDL and HDL has been reported, the structural and functional roles of ox-lipids in LD have never been studied. We have recently documented that oxidatively modified triacylglycerols (ox-TAGs) of LDs alters their partitioning whereby oxidized lipids migrate into the outer monolayer of the LD. We proposed that the ox-lipids located on the LD surface may be involved in anti-tumor immune suppression [23, 24]. Additionally, we suggested that these ox-lipids can be recognized by heat shock protein 70 (HSP70) —a key player in exogenous antigen processing.

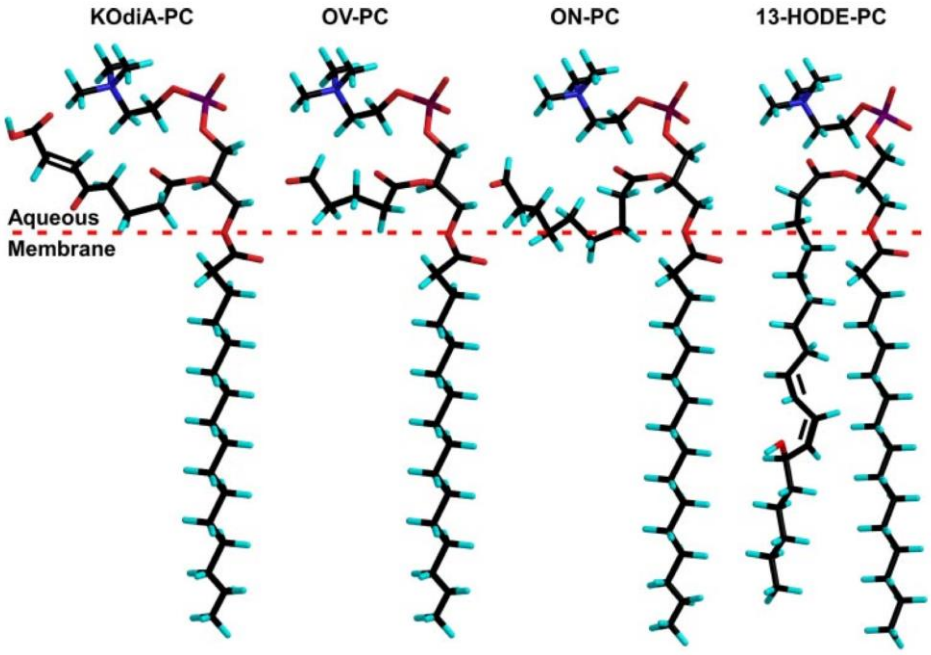

Figure 1-4 Predicted conformational models of oxidized choline glycerophospholipid inside the membranes, containing DMPC or DPPC/cholesterol.

Representation guide: Light blue: hydrogen; black: carbon; dark blue: nitrogen; red: oxygen; purple: phosphorus (adapted from [22]).

1.2 OPEN QUESTIONS, GOALS AND ACCOMPLISHMENTS

1.2.1 Open Questions and Goals

Compelling evidence suggests that lipid signaling events are involved in many cellular pathways, demanding answers to the important questions: Which types of lipid species play an active role in lipid signaling and what are these roles? How does the asymmetric distribution of lipids affect the structures of membranes? How does lipid oxygenation change the LD structure? What is the mechanism of interaction of proteins/enzymes with LDs and membranes containing lipid

signals? To address these biophysical questions in molecular detail for several cellular pathways — antigen-cross presentation, ferroptosis, apoptosis and mitophagy— we applied a combination of molecular dynamics (MD) simulations, molecular docking, and bioinformatics tools.

1.2.2 Significance of the Study

Maintaining or perturbing lipid asymmetry, and/or chemical modifications of lipids can trigger signaling events. The application of computational approaches provides capable tools to perform such mechanistic studies.

Chemical modifications of lipids, mainly peroxidation, generate an array of lipid signals. These ox-lipids may contain a chemically reactive compound such as aldehyde. A myriad of oxygenated products can be made through three lipid peroxidation mechanisms, (i) autoxidation by free radical reaction, (ii) photo-oxidation and (iii) enzyme action. The ox-lipids generated though any of the aforementioned pathways mostly convey lethal signals. It has been recently described that the presence of ox-lipids act as signals in cancer and the ferroptosis cell death pathways [25, 26]. For the former case, it has been established that LDs containing ox-lipids in a tumor environment suppress antigen cross-presentation (ACP), essential for anti-tumor immunity. In the latter case, we concentrated primarily on shedding light on the mechanism of lipid peroxidation via a large family of enzymes called, “lipoxygenases”. The lack of knowledge and proper tools to screen the lipid peroxidation products to determine those involved in signaling processes leave it an open and highly active research area.

In the first two chapters, we predominantly explored the mechanism of action of recently discovered lipid mediators involved in antigen-cross presentation and ferroptosis pathways. Since the MD simulations provide the thermodynamically favored state of the system (the local

or global minima in free energy landscape), this method is capable of predicting structural changes due to the presence of ox-lipids in membranes and LDs. Additionally, it is a proper tool to perform biophysical studies to understand the preferred binding sites, binding modes, and consequences these interactions on the involved proteins and lipid-containing organizations. We clearly demonstrated that the target proteins recognize these structural changes, which can be explored using computational methods.

Several machineries contribute to maintaining cardiolipin's asymmetry necessary in providing the desired membrane potential for healthy mitochondria [27], and inducing the membrane curvature that is involved in cristae formation. However, during apoptosis and mitophagy the collapse of asymmetry mediates the signal of "CL externalization". To this end, CL is translocated from the inner leaflet of IMM to the outer leaflet of OMM [26]. The externalized CL is initially recognized by cytochrome c (cyt-c), a key player of apoptosis and located in the IMS. Once CL migrates to the mitochondrial surface due to an injury, it can be recognized by microtubule-associated protein 1 light chain 3 (LC3), an essential protein of the autophagic machinery mainly localized on autophagosomes [28]. Due to lack of comprehensive mechanistic studies to discover the molecular details of CL-containing membrane interactions with known target proteins, we carefully examined the interactions of the emulated mitochondrial membranes, including the IMM and the OMM, with cyt-c and LC3 to determine how CL externalization triggers apoptosis and mitophagy.

Although the outcome of computational approaches needs to be validated directly/indirectly by experimental approaches, computer modeling likely provides trustworthy insights into the dominant mechanisms that are not accessible to experimentalists. Additionally,

the computational approaches are mainly inexpensive, fast and offer flexible methods to perform such mechanistic studies.

1.2.3 Summary of Thesis Contributions

Lipids function as signals in two ways: (i) chemical modifications of lipids, and (ii) asymmetric distribution of lipids. To understand the mechanism of action of lipid signals in the former, we conducted two studies, (i) ox-lipid signaling in cancer (chapter 3), and (ii) lipoxygenase-dependent lipid signaling in the ferroptosis cell death pathway (chapter 4). To investigate the mechanism of CL signaling in the latter, we performed two studies, (i) CL-signaling in apoptosis through interactions of CL/cyt-c, and (ii) CL-signaling in mitophagy through interactions of CL/LC3 (both in chapter 5).

The ox-lipid signaling in cancer (chapter 3): LDs —ubiquitous organelles in all cells— are comprised of two lipid phases, a neutral lipids core covered by a phospholipid monolayer. The hydrophobic core is mainly composed of triacylglycerols (TAGs). Notably, oxidizable PUFA-TAGs constitute a significant fraction of the total amount of neutral lipids in LDs. In the tumor microenvironment, LC-MS data proved the presence of a large amount of ox-lipids in LDs. While their origin and mechanisms of formation remain to be elucidated, the appearance of TAGs with these polar oxygenated groups in the hydrophobic core on LDs may act as an important factor shifting the equilibrium properties of the LD where the perturbed balance between hydrophobic and hydrophilic groups results in altered distributions of the constituent lipids. Indeed, our computational modeling of LDs containing oxidized neutral lipids indicated that the presence of oxTAGs inside the hydrophobic LD was thermodynamically unstable, resulting in their migration toward the hydrophilic surface. The ox-TAGs disturbed the stability

of the two distinctive LD phases, and their presence causes partitioning of oxTAGs into the phospholipid monolayer. The accumulation and presence of oxidized neutral lipids in the LD monolayer suggests their potential roles in lipid mediator signaling networks. In spite of the fact that this study presents a simplified model of oxidized lipid dynamics in LDs, our data suggest novel mechanisms of biochemical processing of TAGs and oxTAGs that raise challenging biophysical questions.

Next, we explored the possible target proteins to mediate the role of ox-lipids on the LD surface in antigen cross presentation (ACP). Among the many proteins involved in ACP, heat shock proteins —HSP70 and HSP90— play roles in translocation of exogenous antigens, either from the ER-endosome to the cytosol or from the cytosol to the proteasome. According to recent data that described the localization of HSP70 on the LD surface in a tumor environment, we explored the interactions of HSP70 with oxLD and LD. We demonstrated that ox-lipids on the LD surface are recognized by HSP70. Among three candidate oxTAGs-binding sites of HSP70, the site containing a beta-hairpin domain deeply penetrated into the phospholipid monolayer. We additionally proposed that these interactions might be irreversible due to possible covalent binding between aldehyde groups of ox-lipids and lysine residues present in the ox-lipid-biding site of HSP70. The anchoring of HSP70 on the oxLD surface alters HSP70 from its original function in ACP. In conclusion, using computational approaches, we suggest a novel mechanism of ACP suppression through interactions of HSP70 and oxLDs. Therefore, we propose a biological role and resulting pathological significance of oxidized neutral lipid accumulation at the LD surface monolayer.

The lipoxygenase-dependent lipid signaling in ferroptosis (chapter 4): Ferroptosis is a newly coined term for one of the programmed death pathways that emphasizes the mechanism of cell demise associated with the dysregulation of thiol and lipid oxidative metabolism controlled by GPX4. It has been shown that the accumulation of PE-OOH is confined to the extra-mitochondrial ER-associated compartments where several iron proteins —COX, LOX and CYP450— can generate PUFA hydroperoxy-intermediates as the primary molecular products of their reactions. Of those, only LOX's —non-heme-iron enzymes— are the prime candidate-catalysts and sources of the ferroptotic oxygenated PE-species. In this study, we aimed specifically to understand the mechanism of LOX-driven lipid signaling.

Molecular modeling showed that three types of free PUFA, including AA, AdaA and DHA bound similarly to the catalytic site of 15LOX-2 with almost equivalent binding energies (~ -7.0 kcal/mol). The availability and the accessibility of the substrate can affect the enzyme kinetics, which cannot be addressed using molecular modeling. Next, for the first time, we explored the probability of the oxygenation of PLs via 5, 12 and 15LOX, using computational methods. Our data proposed —five out of six— classes of SA-based PLs can effectively interact with the active site of LOXs. Only SA-PS demonstrated significantly low affinities toward all three LOX's. Following the experimental data, we tested two main lipid biomarkers of ferroptosis, SA-PE and SAdrA-PE. The analogous binding pose and binding affinities predicted that both species are equally susceptible to be a substrate of 15LOX-2. Yet, the selectivity of LOX towards PE species was not confirmed using our modeling data. In the case of esterified substrates, a question remains to be answered —how would LOX identify PUFA-PE species, among many other phospholipids with AA- and AdrA-residues for the selective peroxidation? The mechanism based on the formation of specific PE-LOX complexes is not compatible with

our computer modeling data indicating that diversified (phospho)lipid classes can effectively interact with LOX. The computer modeling indicates that PC displays a poor capacity for binding 15LOX as compared to PE.

To decipher the membrane binding mechanism of 15LOX-2, we ran long CGMD simulations and proved it bound with similar orientation for N-terminal membrane binding (NMB) domain, but quite different for the helical active site. These results can be ascribed to the presence of a coil-like structure functioning as a hinge and provide flexibility for the active site. This flexibility can change the accessibility of the active site opening to the substrate. This can affect the activation mechanism of LOXs, but needs further evaluations. Additionally, we found that a long loop in NMB domain with the highest degree of hydrophobicity is responsible for membrane binding —in line with previous studies [29].

The inhibition mechanisms of LOXs, particularly 15LOX, were examined using a known inhibitor, bacalein (as a positive control), and tested/specific inhibitors of ferroptotic cell death. In addition to the aforementioned group of the small molecules, vitamin Es —eight isoforms— also were inspected to possibly explain their mechanism of action on LOX —and indirectly on ferroptosis. Interestingly, all the tested compounds in this study bound to the active site of LOXs. The specific ferroptosis inhibitors, including Fer1, liproxstatin and SRS16-86 bound to the active site with a high affinity. Among them, SRS16-86 demonstrated the highest affinity, more than one unit higher than baclein and AA —the known inhibitor and substrate of 15LOX, respectively. Moreover, we established that different forms of vitamin Es are universally bound to the LOX catalytic site. Thus, one of the physiologically significant mechanisms of vitamin Es action may be stereospecific liganding of the LOX catalytic site outcompeting the oxygenation of free or esterified PUFAs, hence regulating ferroptosis.

CL-signaling in apoptosis through interactions of CL/cyt-c (chapter 5): The initiation and formation of the cyt-c/CL complex, which leads to cyt-c conformational changes and peroxidase activity of cyt-c is pivotal for its role in the early stages of apoptosis. The nature of binding of CL to cyt-c, including affinity, stoichiometry and location of binding sites remains unclear despite numerous studies.

To better understand the interplay of different binding sites and multiple modes of binding proposed previously, we used molecular modeling —in complement to available NMR data— to study the cyt-c/CL interaction and conformational heterogeneity of cyt-c structure. Molecular docking identified three possible locations for the interaction of CL with cyt-c, and available NMR spectroscopy data provides evidence that all of these sites are actually engaged. How can this be possible given the locations on opposite ends of the protein? The answer lies in the fact that the interaction of cyt-c with CL has to be seen in the context of the membrane. Our CGMD and OPM say that the two binding sites identified by docking are actually one when considering the extended size of the membrane and availability of multiple CL molecules within and that cyt-c embeds deeply into the membrane. The simulation further supports the notion that both, electrostatic and hydrophobic forces combined lead to form a tight CL/cyt-c complex and we no longer need to assume a two-step process as in prior models. The ability to bind cyt-c simultaneously at two opposing ends of the heme provides a natural path to formation of the peroxidase by opening the heme crevice through "pulling" by the membrane. We thus consider the simultaneous occupation of the distal and proximal sites as "productive" binding.

We cannot distinguish if membrane curvature enhances the binding of CL to cyt-c in this manner, or if the strain imposed on the membrane by binding is the driving factor for curvature

formation. Either way, our results support a model in which cyt-c is partially and stably embedded in a locally curved and CL-rich membrane patch.

The CGMD results are also in good agreement with the NMR and fluorescence results with respect to the ratio of CL needed to create a peroxidase. Increasing the CL concentration enhances the affinity of cyt-c for the membrane. Remarkably, cyt-c recruits CL to form a cluster in the membrane, which demonstrates that multiple CL molecules (not one alone) stabilize the cyt-c/CL complex.

Taking together the conformational studies of cyt-c and interaction studies with CL, we propose that gain of peroxidase activity by the cyt-c/CL complex is not a small molecule induced effect, but rather is mediated by the interaction with the extensive surface area involved in binding to the CL containing membrane bilayer. This has important biological implications for modulating cyt-c peroxidase activity. The extensive surface area formed between CL and cyt-c is reminiscent of protein-protein interaction interfaces and the inherent conformational flexibility of cyt-c identified by the NMR relaxation measurements is crucial for enabling this interaction.

CL-signaling in mitophagy through interactions of CL/LC3 (chapter 5): 1A/1B-light chain 3 protein mediates both autophagosome formation and cargo recognition during mitophagy. However, the mechanism of recognition of injured/damaged mitochondria is not known. Since it has been known that CLs are externalized in damaged mitochondria we have hypothesized that LC3 may recognize these CLs. To test our hypothesis we employed computational approaches (in complement with the available experimental data generated in our group) to predict the CL binding site(s) of LC3. Molecular docking analysis predicts CL-binding pockets at the LC3 surface, where Arg and Lys interact with the negative head groups of CL with two possible

conformations. The predicted coordinating amino acids include N-terminal residues of LC3 such as Arg 10 and Arg 11 for the top-ranked conformation or Gln 26 and His 27 for the alternative conformation. CGMD simulations of 1,000 ns implicate Arg 10 and Arg 11 in the initial interactions of LC3 with CL-containing membranes. Then, it was experimentally validated that truncation of the predicted CL binding domain or even mutation of the predicted key CL-binding residues impaired the mitophagic process.

Molecular modeling and simulations also predicted that clustering of CL around LC3 may serve to stabilize the initial electrostatic interactions, with the embedding of parts of the protein into the bilayer through hydrophobic interactions. If this is correct, such a clustering mechanism could help ensure that normal transient fluctuations due to lipid transport dynamics do not trigger mitophagy until a critical threshold of LC3–CL interaction density is achieved. It is possible that in some model systems, the threshold may be modulated by concurrent engagement of other cargo-targeting mechanisms.

2.0 CHAPTER 2: APPROACHES

2.1 OVERVIEW

To address the open questions of each part of this study, we mainly applied molecular docking and molecular dynamics simulations. Therefore, in this chapter these two methods will be introduced in general. The details of the approaches for each study will be described in the pertinent chapter. The other techniques, which were utilized for each particular study, will be explained accordingly.

2.2 MOLECULAR DOCKING

2.2.1 Protein-Ligand Docking

Protein-ligand docking is a fast and flexible approach to study the binding pose, bindings sites and approximate binding affinity of ligand with proteins. In the current study, we have applied lipids/ox-lipids as ligands. Considering the structure of lipids, including polar head group and hydrophobic acyl chains, the role of different types of bonds, including electrostatic, hydrophobic and hydrogen bonds can be studied. Although many molecular docking software and online servers are available, in these studies, lipids were docked to the proteins using

AutoDock Vina program, version 1.1.2 [30]. AutoDock Vina is approximately two orders of magnitude faster than AutoDock 4 (a similar, comparable and widely-used package), while the accuracy of the binding mode predictions has been improved as well. AutoDock Vina is benefited from parallelism by using multithreading on multicore machines [30]. Lipids and proteins structures were converted from pdb into pdbqt format using MGL Tools [31]. A grid box was centered to cover the entire protein, the desired domain or binding site of the protein (with maximum dimension of 126 × 126 × 126 points).

2.2.2 Analysis of the Docking Data

AutoDock Vina reports the nine lowest energy conformations (called "model #"), which were inspected using PyMOL software [32]. The best-fit model has been selected according to binding affinity (the highest), visual inspection and clustering the binding models. The residues were interacting with lipid —in 5Å distance to lipids— for each model has been extracted. The visual inspection on Pymol and residue analysis mainly used to cluster the models. All 9 models have been clustered in groups called "binding sites." The number of models in each pocket divided by 9 represents the correspondent probability of the binding site. The well-suited model demonstrated the highest probability of occurrence.

2.3 COARSE-GRAINED MOLECULAR DYNAMICS SIMULATIONS

Molecular dynamics (MD) simulations is a computational method to calculate the time dependent behavior of a molecular system [33]. There are now routinely used of MD to

investigate the structure, dynamics and thermodynamics of biological molecules and their complexes. Molecular dynamics can be run mainly in two resolutions, i. atomistic and, ii. coarse-grained (CG). Atomistic MD considers all the atoms in the system to build an accurate model. CGMD employs approximation to group several heavy atoms in an interaction site called "bead." Considering the relatively large total number of atoms in the systems studied here, which comprise several hundred lipid molecules, protein and water and ions, CGMD simulations, rather than full atomistic MD simulations, offer advantages of greater length and time scales. Moreover, it is the well-suited approach to characterize the dynamic behavior of lipids/ox-lipids, and to examine the biophysics of lipids-proteins interactions [34].

Initially, all the systems were minimized, before NVT ensemble followed by NPT ensemble equilibration runs. According to the system and anticipated properties, each MD run was carried out for a certain time period from 100 ns to several μs. A 5-20 fs time step was used to integrate the equations of motion depends on the system composition. Mainly, due to presence of elastic networks in protein models, which destabilize the system, smaller time step is recommended to use. Non-bonded interactions have a cutoff distance of 1.2 nm. The long-range Coulomb interactions were calculated via the particle-mesh Ewald method [35]. Temperature and pressure were controlled using the Nosé-Hoover [36] and Berendsen [37] algorithms, respectively. All production runs are at 310 K and at 1 atm using NPT ensemble.

2.3.1 Martini Force Field

In the current study, CGMD simulations were based on the MARTINI force field for biomolecular simulations [38]. This model was systematically parameterized based on thermodynamic data, especially experimental data for partitioning behaviors of the molecules.

The calculated free energies presented in Table 2-1 are compared to experimental values for representative small compounds —denoting chemical building blocks. Most of the chosen compounds contain four heavy atoms, following the CG model mapping principles. There are some exceptions, i.e. building blocks containing three or five heavy atoms, which are included either due to the lack of other representative compounds or for comparative reasons.

Table 2-1 Thermodynamic properties of the CG particle types in MARTINI force field [a] [38].

			ΔG^{vap}		ΔG^{hyd}		ΔG^{part}_{HW}		ΔG^{part}_{CW}		ΔG^{part}_{EW}		ΔG^{part}_{OW}	
type	building block	examples	exp	CG	exp	CG	exp	CG	exp	CG	exp	CG	exp	CG
Q_{da}	$H_3N^+—C_2—OH$	ethanolamine (protonated)				−25		< −30		−18		−13		−18
Q_d	$H_3N^+—C_3$	1-propylamine (protonated)				−25		< −30		−18		−13		−18
	NA^+OH	sodium (hydrated)				−25		< −30		−18		−13		−18
Q_a	PO_4^-	phosphate				−25		< −30		−18		−13		−18
	CL^-HO	chloride (hydrated)				−25		< −30		−18		−13		−18
Q_0	C_3N^+	choline				−25		< −30		−18		−13		−18
P_5	$H_2N—C_2=O$	acetamide	sol	sol	−40	−25	−27	−28	(−20)	−18	−15	−13	−8	−10
P_4	HOH (× 4)	water	−27	−18	−27	−18	−25	−23		−14	−10	−7	−8	−9
	$HO—C_2—OH$	ethanediol	−35	−18	−33	−18	−21	−23		−14		−7	−8	−9
P_3	$HO—C_2=O$	acetic acid	−31	−18	−29	−18	−19	−21	−9	−10	−2	−6	−1	−7
	C—NH—C=O	methylformamide	−35	−18		−18		−21		−10		−6	−5	−7
P_2	$C_2—OH$	ethanol	−22	−16	−21	−14	−13	−17	−5	−2	−3	1	−2	−2
P_1	$C_3—OH$	1-propanol	−23	−16	−21	−14	−9	−11	−2	−2	0	1	1	−1
		2-propanol	−22	−16	−20	−14	−10	−11	−2	−2	−1	1	0	−1
N_{da}	$C_4—OH$	1-butanol	−25	−16	−20	−9	−5	−7	2	0	4	2	4	3
N_d	$H_2N—C_3$	1-propylamine	−17	−13	−18	−9	(−6)	−7	(1)	0	(−3)	2	(3)	3
N_a	$C_3=O$	2-propanone	−17	−13	−16	−9	−6	−7	1	0	−1	2	−1	3
	$C—NO_2$	nitromethane	−23	−13	−17	−9	−6	−7		0		2	−2	3
	$C_3=N$	proprionitrile	−22	−13	−17	−9	−5	−7		0		2	1	3
	C—O—C=O	methylformate	−16	−13	−12	−9	(−6)	−7	(4)	0	(−1)	2	(0)	3
	$C_2HC=O$	propanal		−13	−15	−9	−4	−7		0	2	2	3	3
N_0	$C—O—C_2$	methoxyethane	−13	−10	(−8)	−2	(1)	−2		6	(3)	6	(3)	5
C_5	$C_3—SH$	1-propanethiol	−17	−10		1		5		10		10		6
	$C—S—C_2$	methyl ethyl sulfide	−17	−10	−6	1	(7)	5		10		10	(9)	6
C_4	$C_2=C_2$	2-butyne	−15	−10	−1	5		9		13		13	9	9
	C=C—C=C	1,3-butadiene		−10	2	5	11	9		13		13	11	9
	$C—X_4$	chloroform	−18	−10	−4	5	(7)	9	14	13		13	11	9
C_3	$C_2=C_2$	2-butene		−10		5		13		13		13	13	14
	$C_3—X$	1-chloropropane	−16	−10	−1	5	12	13		13		13	12	14
		2-bromopropane	−16	−10	−2	5		13		13		13	12	14
C_2	C_3	propane	gas	−10	8	10		16		15		14	14	16
C_1	C_4	butane	−11[b]	−10	9	14	18	18		18		14	16	17
		isopropane	gas	−10	10	14		18		18		14	16	17

[a] Free energies of vaporization ΔG^{vap}, hydration ΔG^{hydr}, and partitioning G^{part} between water (W) and organic phases (H, hexadecane; C, chloroform; E, ether; O, octanol) are compared to experimental values. The experimental vaporization free energy was calculated from the vapor pressure p_{vap} using ΔG^{vap}) $k_BT \ln(p_{vap}/k_BTc_M)$, where c_M denotes the molar concentration of the liquid. The experimental free energies of hydration and partitioning were compiled from various sources based on log P values. The temperature for the experimental data is in the range 298-300 K, except where indicated. Simulation data were obtained at 300 K. Experimental properties between parentheses are estimates obtained from comparison to similar compounds. The statistical accuracy of the free energies obtained from the simulations is ±1 kJ mol^{-1}. [b] The temperature for the experimental data is 273 K [38].

This force field is the most widely used CG available force field for lipids. Bonded parameters are optimized by comparison to lipid conformations sampled with an atomistic force field. CGMD simulations of model membranes demonstrate good agreement with atomistic simulations as well as available experimental data, especially concerning structural properties such as electron densities, area per lipid and membrane thickness [39]. The MARTINI can model the behavior of lipid bilayers in terms of the stress profile across the bilayer and its tendency to form pores quite consistent with full atomistic simulations [38]. Figure 2-1 illustrate three examples of Martini force field for two lipids.

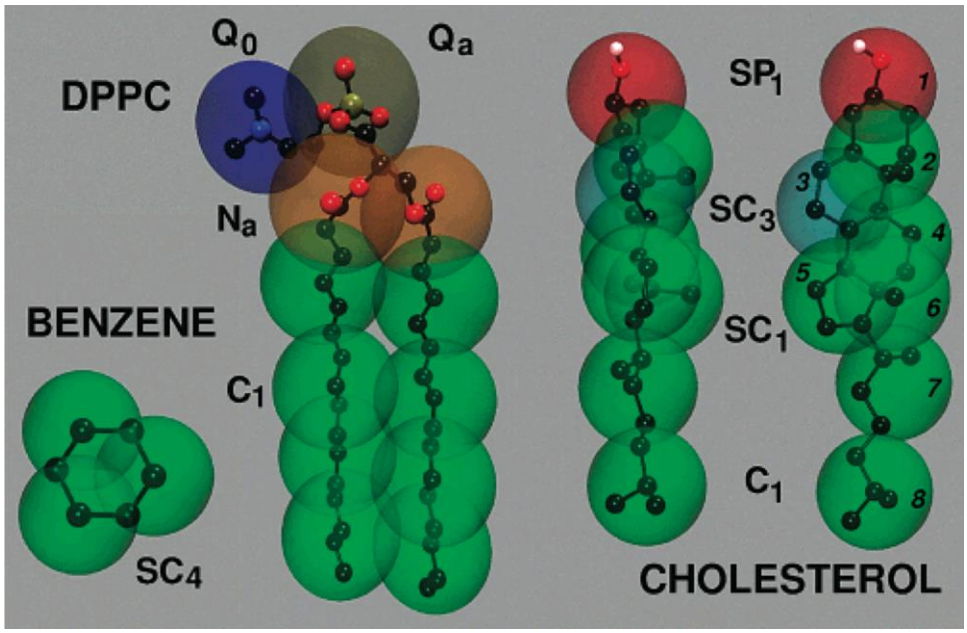

Figure 2-1 MARTINI CG mapping of DPPC, cholesterol, and benzene. The prefix "S" denotes ring structures [38].

The MARTINI force field has been extended to protein [40] considering elastic network to preserve the protein structure [41], DNA [42] and nanoparticles [43]. The MARTINI group has

developed tools to set up CG model for protein, considering elastic networks called “martinize.” The current version of martinize is 2.5 that was released in 2015. Moreover, “insane” can be used to set up the membrane with various lipid classes and species. However, we mostly used Packmol [44] software to building the lipid containing organizations, including bilayer and LD various lipid compositions. Packmol is able to pack millions of atoms and grouped them in arbitrarily complex molecules inside a variety of 3D regions. The final packing shape can be sphere, ellipse, cylinder, plane, or cubic. The only inputs of Packmol are the structure of one molecule of each class and the geometrical constraints that each class of molecule must satisfy. The complexes easily can be solvated in water, other solvents, or mixtures of them. The packing time for MD systems varies from a few seconds to a few hours using a personal computer.

2.3.2 Analysis of the CGMD trajectories

Visual Molecular Dynamics (VMD) has been developed by the Theoretical and Computational Biophysics group at the University of Illinois and the Beckman Institute in 1995 [45]. VMD is a molecular graphics program designed for visualizing and analyzing of molecular dynamics trajectories. VMD can display several structures using a wide variety of rendering styles and coloring methods. Molecules are shown as one or more “representations.” It is the most capable visualizing package with MARTINI force field CGMD simulations. Since the bond definition in CGMD simulation is different from full atomistic system, VMD is not able to recognize the bonds. Therefore, the script called “cg_bonds.tcl” was employed to represent the bonds in MARTINI. The “cg_secondary_structure.tcl” tool was also used to draw protein secondary structure in VMD. Various scripts and tools —mainly available in GROMACS package— have

been employed to measure divers properties of the system. For instance, to measure the distance variation of molecules during trajectory we employed “g_dist” script.

3.0 CHAPTER 3: COMPUTATIONAL STUDIES OF LIPID SIGNALING IN A TUMOR ENVIRONMENT

3.1 SUMMARY

Lipid droplets (LDs) are ubiquitous and physiologically active organelles regulating the storage and mobilization of lipids in response to metabolic demands. Among the constituent LD neutral lipids, such as triacylglycerols (TAGs), cholesterol esters (ChEs), and free fatty acids (FFAs), oxidizable polyunsaturated molecular species may be quite abundant, yet the structural and functional roles of their oxidation products have not been studied. The presence of these peroxidized species in LDs of dendritic cells in cancer has been documented. Assuming that hydrophilic oxygen-containing functionalities may markedly change the hydrophobic/hydrophilic molecular balance, here we utilized computational modeling to test the first hypothesis that "lipid peroxidation causes redistribution of lipids between the highly hydrophobic core and the polar surface (phospho)lipid monolayer—the area enriched with integrated enzymatic machinery".

Quantitative liquid chromatography/mass spectrometry (LC/MS) was used because of the choice of molecular species and amount of oxidized lipids (ox-lipids) in LDs. Using CG-MD simulations we established that oxidation of lipids changes their partitioning, whereby oxidized

lipids migrate into the outer monolayer of the LD. In the second part of this chapter, we evaluate our second hypothesis that "ox-lipids on the LD surface possibly lead to the formation of oxygenated lipid mediators to interact with particular target proteins/enzymes". Fluorescence microscopy of LDs in tumor environment revealed the localization of heat shock protein 70 (HSP70) on the LD surface. In addition to improving the overall protein integrity, HSP70 plays a crucial role in antigen cross presentation (ACP) —essential to anti-tumor immunity. Therefore, we employed computational approaches to decipher the mechanism of interactions of oxidized-lipid-containing LD (oxLD) and HSP70. Although HSP70 rarely interacts with LD, it tightly binds on the oxLD surface. We predicted that a β-hairpin motif in N-terminal region of HSP70 is responsible for anchoring HSP70 on oxLD surface.

3.2 SIGNIFICANCE

Chemical modifications of lipids, mainly peroxidation, generate an array of lipid signals. These ox-lipids are mostly chemically reactive compounds. A myriad of oxygenated products can be made through three lipid peroxidation mechanisms: (i) autoxidation by free radical reaction, (ii) photo-oxidation and (iii) enzyme action. The ox-lipids generated though any of the aforementioned pathways mostly convey lethal signals. It has been recently described that the presence of ox-lipids acts as signals in cancer to suppress ACP [23, 46]. The lack of knowledge and proper tools to screen the lipid peroxidation products to find out those involved in signaling processes leave it an open and highly active research area. Additionally, discovering the mechanism of action of ox-lipids in ACP suppression using the conventional methods is hard to achieve.

Here, we utilized computational methods to unearth the role of oxidized lipid in ACP suppression. To this end, we initially described the dynamics behavior of oxidized lipids in LD using molecular dynamics (MD) simulations. Since MD simulation provides the thermodynamically favored state of the system (local or global minima in free energy landscape), it is a capable method to predict structural changes due to the presence of ox-lipids in LDs. Subsequently, we examined the interactions of ox-lipids and HSP70 —a protein that is known to be involved in ACP. Our computer modeling data proposed that HSP70 recognizes the structural changes imposed by oxidized lipids in LD.

3.3 INTRODUCTION

Lipid droplets (LDs) are dynamic cytoplasmic organelles that can be found in nearly all eukaryotic cells [47]. They play important roles during changes in metabolism of intracellular neutral lipids, particularly free fatty acids [48]. Not surprisingly, LDs have been related to dyslipidemias that are characteristic of a number of chronic diseases, including obesity, diabetes, atherosclerosis, and the metabolic syndrome [49].

The structural organization and function of LDs are determined by the physico-chemical intermolecular interactions of neutral lipids with each other in the hydrophobic core and with phospholipids, particularly phosphatidylcholine (PC), as well as with proteins embedded in the surface monolayer (Figure 3-1A). The number of PCs and other polar molecules available to cover sufficient surface area of the LD defines its overall size in the aqueous cytosolic environment [50]. Moreover, the surface monolayer, along with its enzymatic machinery and

corresponding adapter proteins, is viewed as a locale of metabolic conversions of constituting LD lipids (Figure 3-1B) [51].

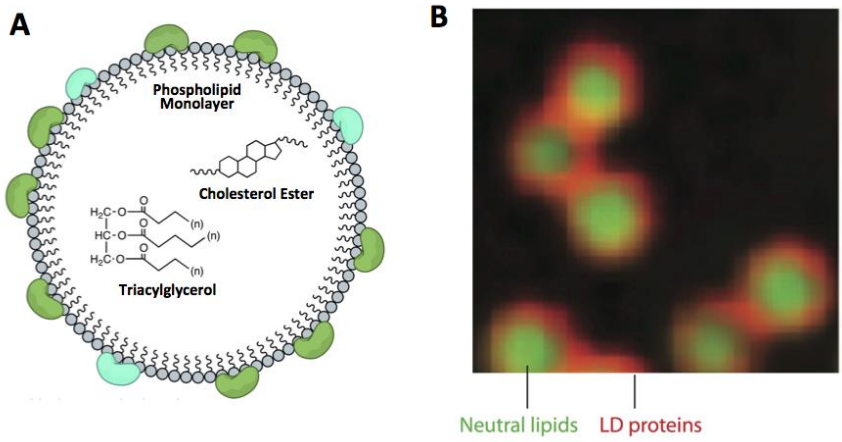

Figure 3-1 Lipid droplet structure.

A. LD hydrophobic core is separated from the aqueous cytosol by a monolayer of surface phospholipids. **B.** LDs are decorated with specific surface proteins localized on the LD surface. Neutral lipids (green) and LD-associated proteins (red) visualized by fluorescence microscopy (adapted from [47]).

In addition of the known functions of LDs, e.g. lipid storage, recently many novel roles of LDs have been emerged. Figure 3-2 shows a model of the emerging roles of LDs, including their role in immunity and host-pathogen interactions [52]. These functions highlight the role of lipid signaling through LDs in several immune-related pathways. It has been shown that LDs are involved in bacterial/viral infections and antigen-cross presentations (ACP). Although the details of former have been studies, how LDs participate in cross-presentation is not clear.

Among the neutral lipids comprising the hydrophobic core, TAGs, ChEs, FFAs—in different proportions—are the most prominent components of LDs [53]. While the composition and molecular identities of neutral lipids are influenced by extra- and intracellular metabolic

demands, a significant proportion of these molecules may be represented by polyunsaturated species with two or more double bonds [54]. This suggests that the vulnerability to oxygenation may lead to the appearance of polar functionalities in the hydrophobic acyls, shifting the molecular hydrophobic/hydrophilic balance [55], and causing significant modifications of LDs organization. Indeed, the presence of oxygenated TAGs, ChEs, and FFAs in immunologically impaired dendritic cells from tumor-bearing animals and cancer patients has been documented [23, 46].

Reasoning that these oxidative modifications of polyunsaturated fatty acid (PUFA)-containing LDs may be widespread, here we undertook a CGMD study of the effects triggered by the appearance of oxidized TAGs (oxTAGs) in LDs. Given the myriads of possible diversified oxygenated TAGs, our choice was based on the LC-MS-based detection of these species in dendritic cells of tumor-bearing mice [56]. We demonstrate that oxTAGs affect the hydrophobic–hydrophilic balance of LDs, leading to disturbances in phase separation between the neutral lipid core and the phospholipid outer monolayer. Therefore, they possibly can be recognized by proteins/enzymes on LD surface. Recent experimental data demonstrated that HSP70 localizes on LDs present in tumor environment, but not in wild type cells. Moreover, it is known that HSP70 is involved in exogenous antigen processing by facilitating their translocation to the proteasome [57]. We then hypothesized that HSP70 recognizes ox-lipids on oxLD surface. Hence, we have studied the interactions of HSP70 and oxLDs via molecular modeling to test our hypothesis and decode the mechanism of action of ox-lipids in ACP suppression.

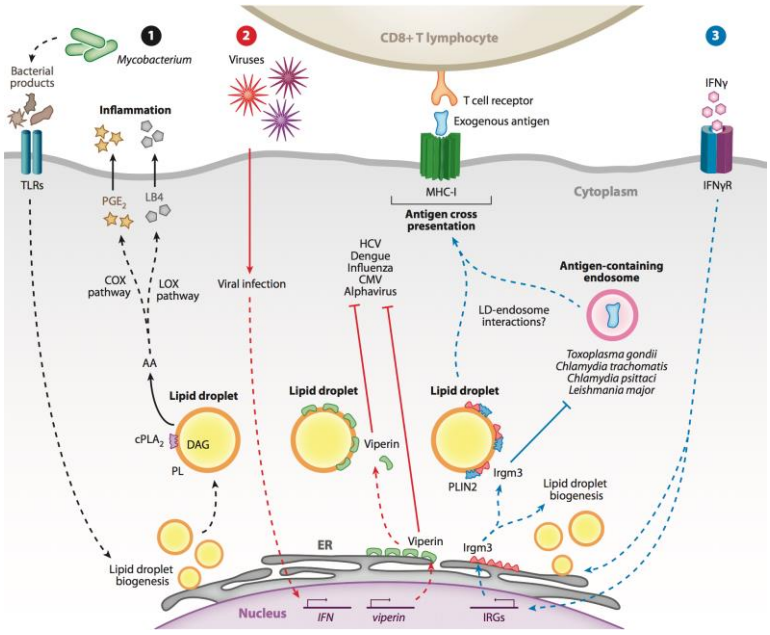

Figure 3-2 Novel emerging roles of LDs in immunity.

1. LDs participate in the biosynthesis and secretion of inflammatory mediators (black pathways). In this pathway accumulation of LDs can be triggered through Toll-like receptor (TLR) dependent manner. Eicosanoids prostaglandin E2 (PGE2) or leukotriene B4 (LB4) — cyclooxygenase (COX) or lipoxygenase (LOX) products of arachidonic acid metabolization— are released that potent inflammation mediators and immunity modulators. **2.** Due to viral infections (red pathways), cells respond by producing IFN, which induces the expression of IFN-stimulated factors. Viperin, one of such factors, localizes to LDs, exerts antiviral activity against a range of viruses. **3.** Involvement of LD in antigen-cross presentation (blue pathways). Upon IFNγ stimulation, a family of IFN-related GTPases (IRGs) proteins are induced. A member of this family, Irgm3, localizes to the ER and to LDs where it can interact with PLIN2 (ADRP). Irgm3 is essential for IFNγ-induced LD biogenesis and for antigen-cross presentation to CD8+ T lymphocytes (MHC-I) (adapted from [52]).

3.4 APPROACH

3.4.1 Setup and Optimization of CG Model of LD

To decipher the possible mechanism of ACP suppression, the experimental data were leveraged to set up models of LDs containing oxygenated lipid productions. The structural and conformational changes in LDs were assessed using CGMD simulations. To set up a LD system, the size of the LD is a crucial parameter. According to the study by Penno et al. [58] about the size of LD and the ratio of triacylglycerols/ phosphatidylcholine (TAG/PC) lipids, very small LD poorly represent the real system (LD size: 100 nm – 100 μm). As the authors proposed, the ratio of TAG/PC increases by increasing the LD radius (Eq. 3-1):

$$TAG = 0.215 nm^{-3} \times a \times (r - 2.5)^3 \times r^{-2} \times PC \qquad \text{(Eq.3-1)}$$

where *a* is the surface area per PC molecules in nm^2 (about 0.7 nm^2 is acceptable for different PC) and *r* is the LD radius measured in nm. To create the optimized LD model, we initially built CG models of POPC and TAG (Figure 3-3A). Then, we investigated the effect of phospholipid to TAG relative ratios on the shape of the resulting LD model (Figure 3-3B). The four different POPC:TAG ratios of 1, 2, 3, and 4 were chosen and subjected to simulation. The resulting shapes of the LDs with different lipid compositions, as inspected after 50 ns equilibration, are summarized in Table 3-1. A model that shows spherical characteristic shape and two distinct phases, containing 200 TAG and 400 POPC molecules (r = ~6.5 nm), has been chosen to evaluate role of oxTAGs on LD structure.

Table 3-1. LDs with four different lipid compositions and their shapes after 50 ns equilibration.

Composition		POPC:TAG Ratio	Shape
POPC	TAG		
800	200	4	Not Spherical - asymmetric
600	200	3	Close to spherical – asymmetric
400	200	2	Spherical
200	200	1	Close to spherical – asymmetric – POPCs did not cover the surface thoroughly

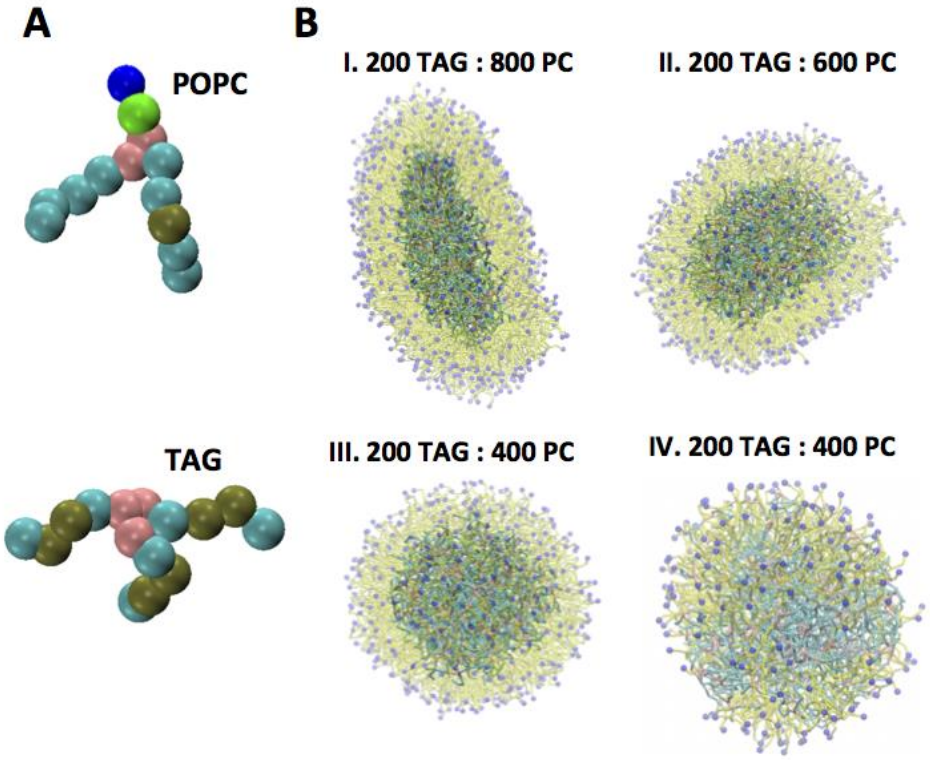

Figure 3-3 Effect of POPC:TAG ratio on LD shape.

A. CG model of triacylglycerol (upper panel) and POPC (lower panel). Color guide: cyan: ~4 carbons with saturated bonds; brown: ~4 carbons with one unsaturated bonds; pink: glycerol group; green: phosphate group; blue: choline group. **B.** CGMD snapshot of 50ns equilibrated lipid droplets structure containing 200 TAG and I. 800 POPC, II. 600 POPC, III. 400 POPC and IV. 200 POPC. Color guide: blue beads: choline group of POPC, transparent yellow: POPC; cyan: acyl chain of TAG, pink: head groups of TAG.

3.4.2 CGMD Simulations of LD Containing oxTAGs

The effects of adding oxidatively truncated- and dihydroxy-TAGs to the LD core on lipid partitioning in LDs were evaluated using CGMD simulations with the optimized LD model. Two different levels of oxidation have been assessed, 5 and 10 mol% oxTAGs. As controls, we simulated LDs without adding any oxidized TAG species. Thus, five fully hydrated systems were set up (Table 3-2).

Table 3-2. Composition of LDs used to study the role ox-TAGs on LD structure via CGMD simulations.

System	Composition			
	Dihydroxy-TAG	Truncated-TAG	TAG	POPC
5 mol% dihydroxy-TAG	10	--	190	400
10 mol% dihydroxy-TAG	20	--	180	400
5 mol% truncated-TAG	--	10	190	400
10 mol% truncated-TAG	--	20	180	400
Control	--	--	200	400

For each of the five systems, three different simulations were carried out by equilibrating them with three different random seeds to produce different initial velocities and thus different trajectories. In total, 15 simulations were run, 2 μs each.

3.4.3 Study Interactions of oxLD and HSP70

Then, a combination of sequence and 3D structure analysis, molecular docking and CGMD simulation were used to study the mechanisms of interaction of oxygenated products and HSP70.

Sequence and 3D structure alignments: Since the only available full-length structure of HSP70 belongs to *E. coli* (PDB ID: 2KHO) [59], the identity and similarity of this structure with human HSP70 were studied. The sequence alignment was carried out using the protein blast option of the BLAST server [60].

Molecular docking: The oxygenated truncated TAG (18:2/C9-OND/18:2-TAG) was docked to the crystal structure of *E. coli* HSP70 (PDB ID: 2KHO). Since the protein is not fitted in a grid box, it was split into two pieces, including the N-terminal ATPase domain (NAD) as one piece and the substrate binding domain (SBD) and C-terminal domain (CD) as another piece. In both cases, the top-ranked binding pose with the highest binding affinity was reported

CGMD simulations: Two types of LD have been set up, with and without oxygenated products, called oxLD and LD respectively. Here the oxLD model contains oxTAG (18:2/C9-OND/18:2), oxTAG (18:2/C9-OND/18:2) and 4-Hydroxynonenal (HNE) with corresponding concentrations of 7 mol%, 1 mol% and 2 mol%. *E coli*. The HSP70 chaperon was modeled based on the MARTINI force field. The elastic network was applied as a structural scaffold to maintain the overall shape of the protein [61]. For each of the two systems, three different simulations were performed by equilibrating them with three different alignments of HSP70 versus LD to consider the effects of protein orientation on the trajectories. In total, 6 simulations were run, 2 μs each. Initially, each system was minimized for 20 ps, before NVT and NPT ensemble equilibrations. A 20 fs time step was used to integrate the equations of motion.

3.5 RESULTS

3.5.1 Development of a CGMD Model for LD

CGMD modeling has been successfully applied to studies of lipoproteins – HDL and LDL [62-64], but not generic LDs. We therefore first developed and optimized a model for a LD without oxTAGs. In the initial simulations, we assessed the effects of varying the POPC:TAG ratios at a fixed number of TAGs on LD organization after 50 ns equilibration. The LDs shape was strongly dependent on the number of POPC molecules present. When the number of POPC was too high, elongated shapes were observed, and when the number of POPC was too low, there was not sufficient POPC to cover the surface of the LD.

Only at a POPC:TAG ratio of 2 was the characteristic spherical shape and two distinctively separated phases of core and surface monolayer were achieved. This equilibrated arrangement of LDs remained stable within 2 μs (Figure 3-4A) at which point several TAG molecules were found to be partitioned from the hydrophobic core into the more polar regions of the PC monolayer. Analysis of 1D and 2D number density graphs (Figure 3-4B and C, respectively) along the *z*-direction established that the approximate boundary of the LD core and monolayer was located at r= ~4 nm.

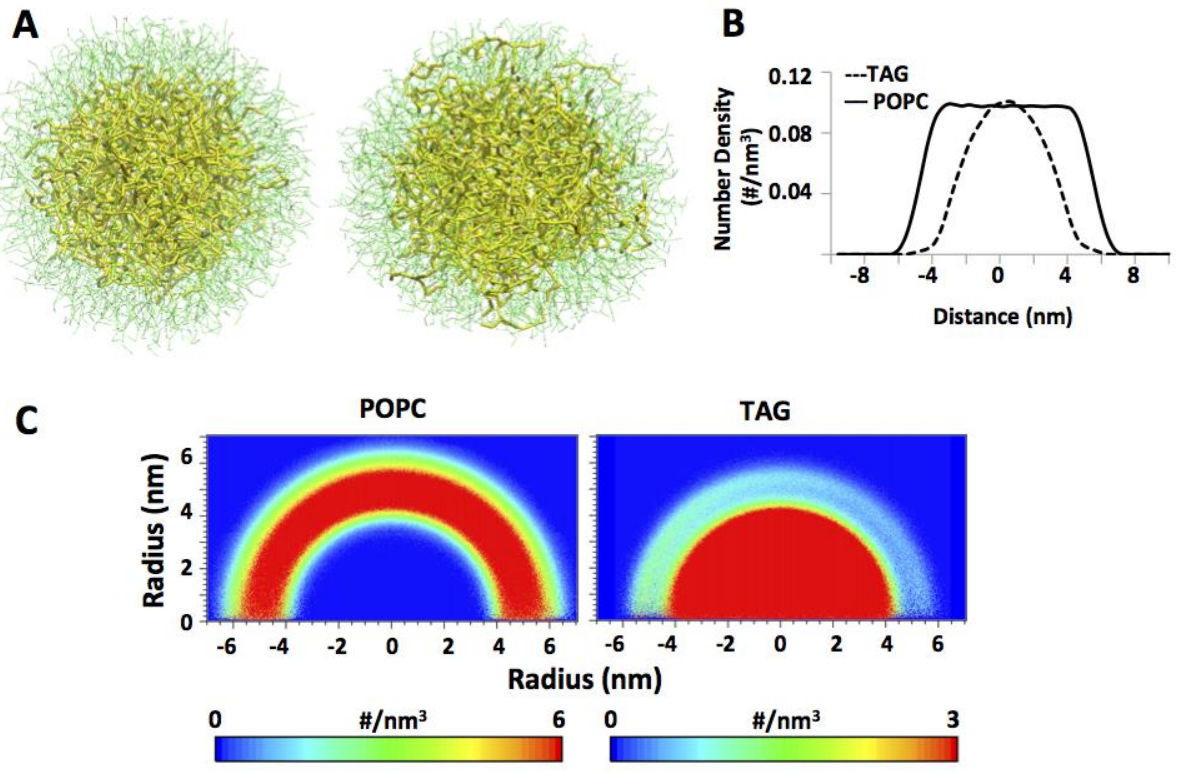

Figure 3-4 CG-MD simulations of lipid droplets containing POPC in monolayer and TAG in the core, without any oxidized lipids (control system).

A. CG-MD snapshot of the control system at t=0ns (left) and t=2μs (right). Color guide: thin green line: POPC; thick yellow line: TAG. **B.** 1D number density of lipids along the *z*-axis of the simulation box. **C.** 2D number density maps of POPC (left) and TAG (right) molecules along the *z* direction.

3.5.2 Effects of Lipid Oxidation on Lipids Dynamics in LD

To study the effect of lipid oxidation on lipid dynamics in LD, we used the LC-MS data to guide us in the choice of molecular species and the amounts of oxidized lipids to be modeled. The LC-MS data confirmed the presence of several oxygenated TAGs including truncated species. LDs containing two representative types of oxidized TAGs—with hydroxy-LA and oxidatively

truncated LA—at two different oxidization levels (5 and 10 mol% of total TAGs) have been employed in the CG-MD simulations (Figure 3-5).

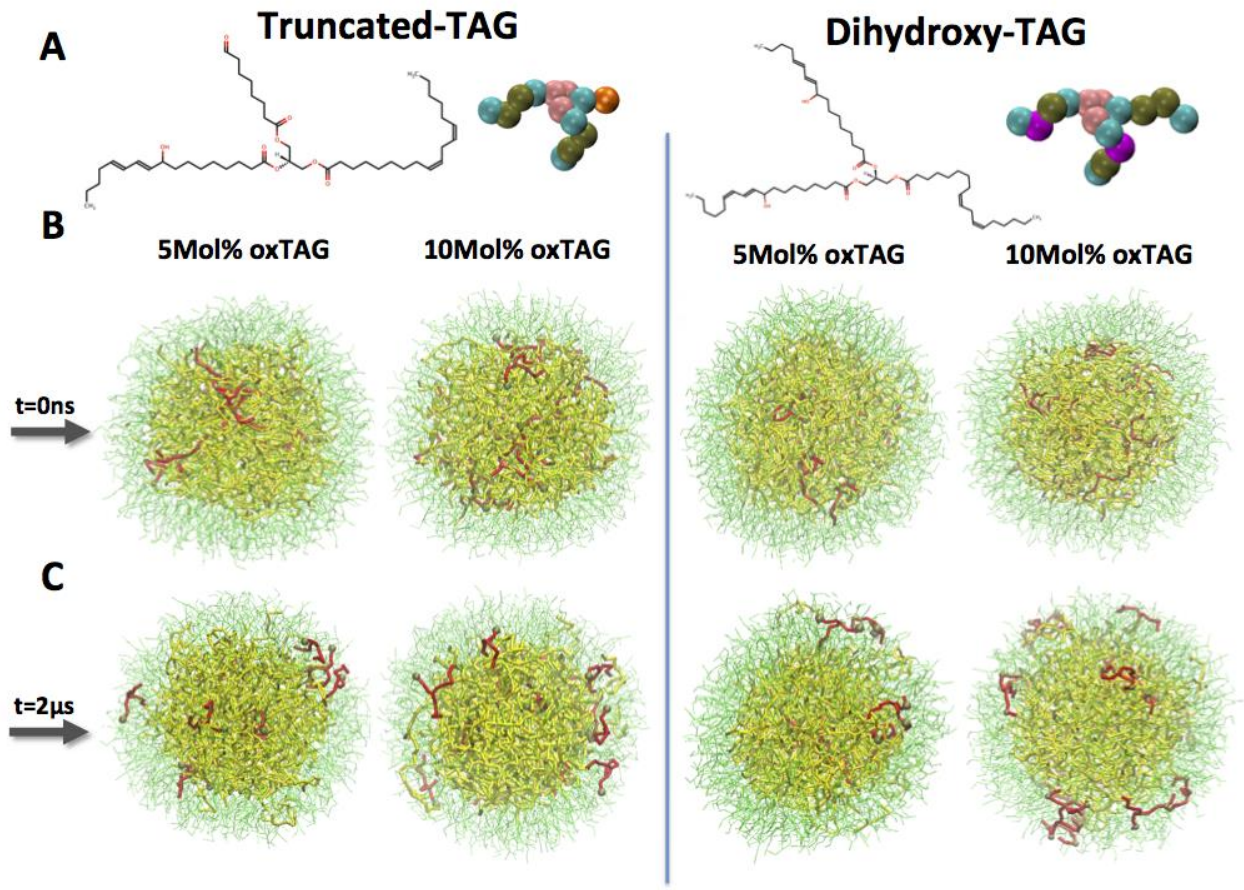

Figure 3-5 Initial and final configurations of LDs containing oxTAGs determine that significant amount of oxidized species move to the monolayer.

A. CG models of oxidized species. Color guide for CG model of oxidized TAG: cyan: ~4 carbons with saturated bonds; brown: ~4 carbons with one unsaturated bonds; pink: glycerol group; purple: part of the acyl chain in a dihydroxy-TAG containing –OH group; orange: part of acyl chain in a truncated-TAG containing =O group. **B.** and **C.** Initial and final configurations of LDs structure containing 5mol% (left) and 10mol% (right) trauncated- and dihydroxy-TAGs. Color guide for LD structure: thin green line: POPC; thick yellow line: TAG; thick red line: oxTAG; brown sphere: oxidized bead.

When compared to non-oxidized TAGs, we found that a significantly larger amount of oxidatively modified TAGs of both types partitioned into the phospholipid monolayer. 1D number density graphs of oxidatively truncated TAG displayed two shoulders on both sides of the graph, clearly revealing their tendency to partition into the PC monolayer (Figure 3-6A). 2D number density maps of oxTAGs uniformly confirmed their preferred redistribution from the hydrophobic core into the more polar surface monolayer (Figure 3-6B).

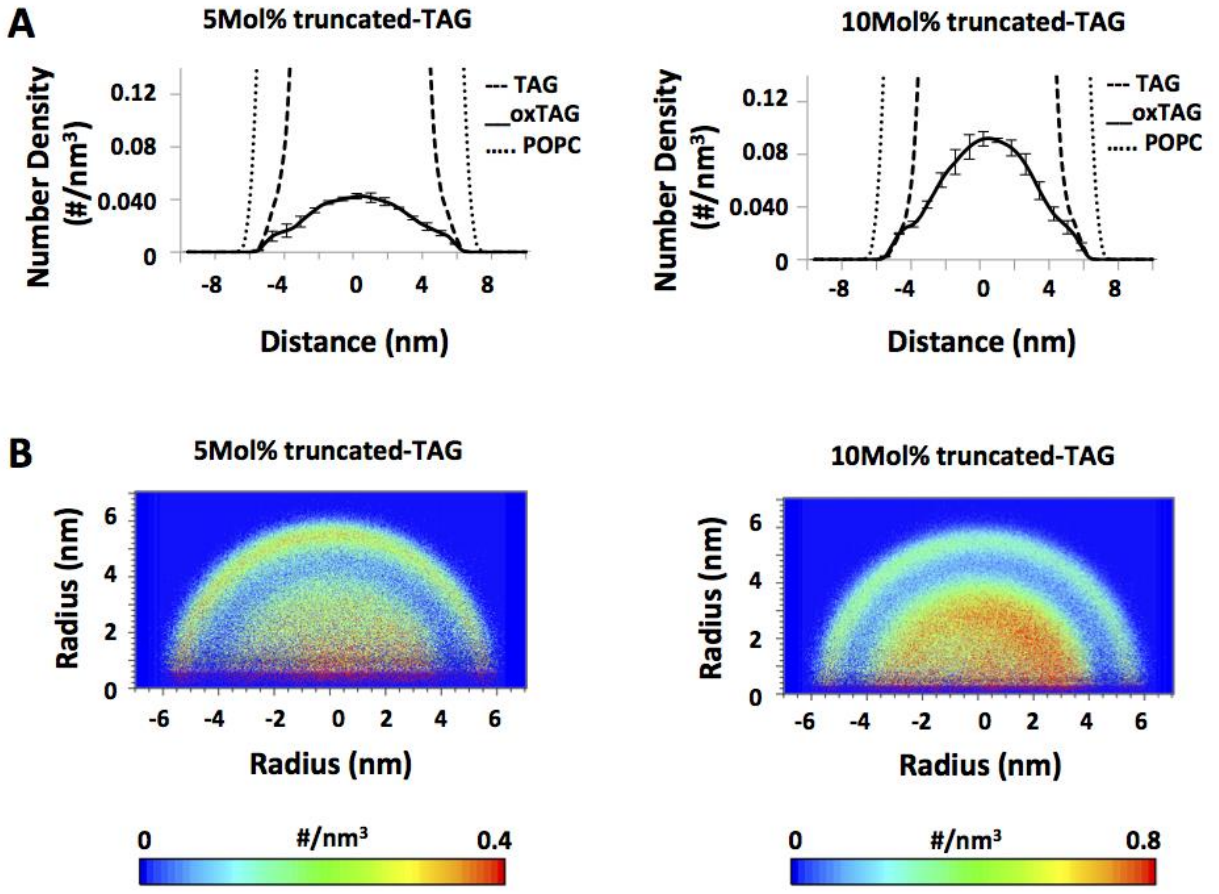

Figure 3-6 Number density of oxTAGs in the systems containing truncated-TAGs along the *z*-axis of the simulation box.

A. 1D and **B.** 2D number density of oxTAGs for systems containing 5 mol% (left) and 10 mol% (right) oxygenated truncated-TAGs.

Similar behavior was observed for LDs containing dihydroxy-TAG species (Figure 3-7). To compare the dynamics of non-oxidized TAGs and oxTAGs, 2D number density maps of TAGs for the entire systems were generated (Figure 3-8). They demonstrated that non-oxidized TAGs were preferentially located in the core region.

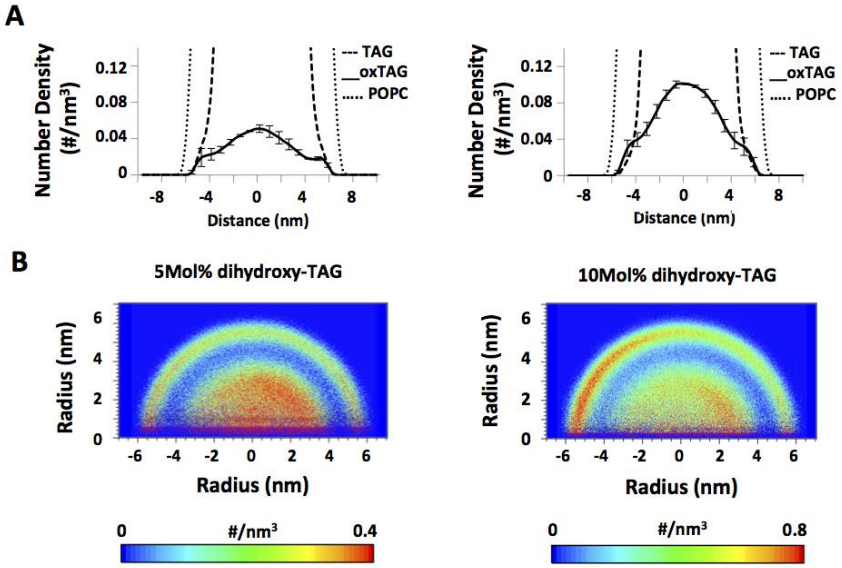

Figure 3-7 Number density of oxTAG in systems containing dihydroxy-TAGs along the z-axis of the simulation box.

A. 1D number density of oxTAGs in system containing 5mol% (left) and 10mol% (right) dihydroxy-TAGs. **B.** 2D number density of oxTAGs in system containing 5mol% (left) and 10mol (right) dihydroxy-TAGs.

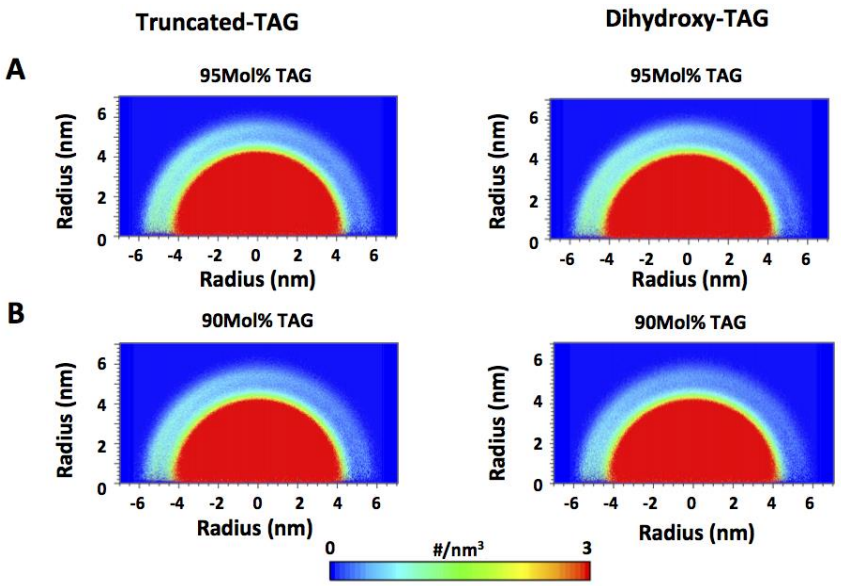

Figure 3-8 2D number density map of non-oxidized TAG molecules.

2D number density of four systems containing, **A.** 5mol% truncated-TAGs (left) and 5mol% dihydroxy-TAGs (right); **B.** 10mol% truncated-TAGs (left) and 10mol% dihydroxy-TAGs.

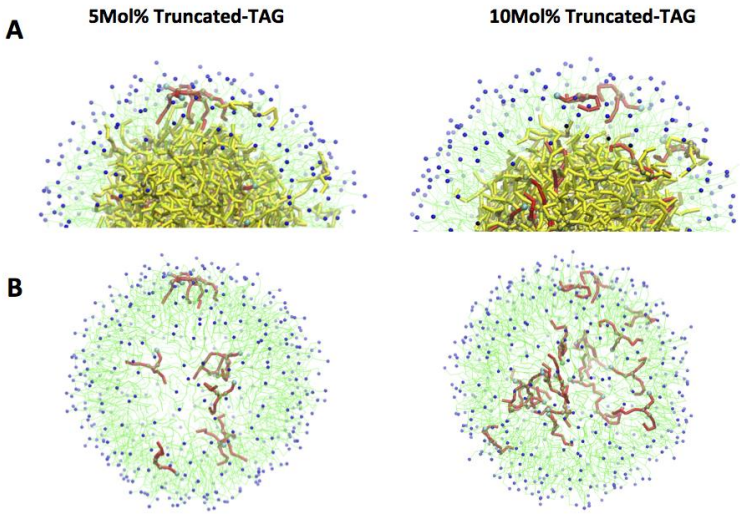

Figure 3-9 oxTAGs are located close to the surface, but below the head groups of POPC molecule.

A. CG-MD representation of TAGs and oxTAGs in POPC monolayer of LD containing 5mol% and 10mol% truncated-TAGs. TAGs and oxTAGs are located below the head groups of POPC molecules (blue spheres represents choline groups). They do not have access to water molecules directly; **B.** The final distribution of oxTAGs (TAGs removed for clarity). oxTAGs were distributed randomly, without detectable clustering. Color guide: thin green line: POPC; thick yellow line: TAG; thick red line: oxTAG; brown sphere: glycerol bead; green sphere: oxidized bead.

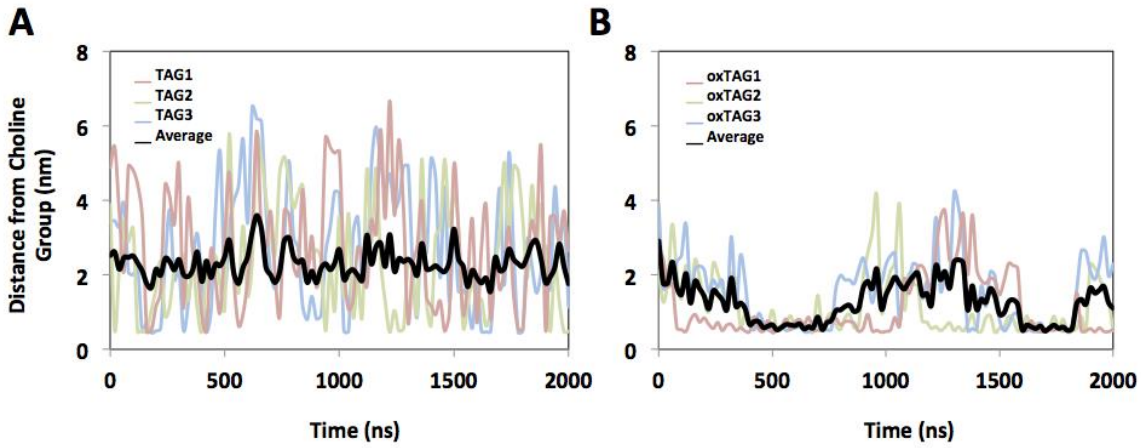

Figure 3-10 Distance of center of mass (COM) of TAG/oxTAG to choline groups of POPC (LD surface) vs. time; in 5mol% truncated-TAG system, A. TAGs, B. oxTAGs.

Three TAG and oxTAG molecules were randomly chosen to calculate their COM distance to choline groups of POPC —representing LD surface— was calculated. Averaged values of COM of these molecules show that oxTAGs preferentially stay for longer time in the proximity of the phospholipid monolayer over the entire trajectory while TAGs are not stable in the outer monolayer and fluctuate between the two LD phases.

The expanded view of the final configurations showed that TAGs and oxTAGs in the monolayer were located below the head groups of POPC molecules (Figure 3-9 A) and were distributed arbitrarily, without detectable clustering (Figure 3-9 B). The dynamics of several randomly selected oxTAGs and TAGs revealed that unlike TAGs, the oxTAGs preferred to remain in the monolayer (Figure 3-10).

3.5.3 Interactions of Oxidized LD and HSP70

According to our data, addition of hydrophilic oxygen-containing functionalities during peroxidation of polyunsaturated fatty acid residues of lipid molecules may markedly change the hydrophobic/hydrophilic balance of the latter. This may dramatically affect the structural

organization of lipid-enriched domains of membranes and lipid droplets. Our previous work has established the accumulation of neutral lipids and formation of lipid droplets in DC of tumor-bearing animals and cancer patients [24]. This has been accompanied with the important disturbances of one of the major DC functions – cross-presentation of antigens [23] whereby not only higher levels of neutral lipids and LDs but the obligatory presence of elevated levels of peroxidized TAGs, peroxidized ChEs and peroxidized FFAs were necessary for the characteristic immune-deficiency of DCs in cancer [24].

Based on the identified chemical structure of peroxidized neutral lipids accumulating in lipid droplets of DC affected by tumor-derived factors, we utilized computational modeling to decipher molecular mechanisms through the peroxidation products may affect the antigen cross-presentation. Three oxidatively truncated oxTAG species were examined in LD, including two TAGs species with esterified C9-ONA, as well as with 4-Hydroxynonenal (HNE). Using CG-MD simulations we endeavored to explore the motional behavior and preferred localizations of oxTAGs within lipid droplets. CG-MD demonstrated the higher likelihood of oxTAGs —versus non-oxidized lipids— to leave the LD hydrophobic core and re-locate into the phospholipid monolayer on the LD surface [65]. This migration of oxTAG to the LD outer monolayer makes them accessible for interactions with multiple cytosolic proteins, including those involved in antigen cross-presentation. Therefore, we were interested in exploring possible interactions of oxTAG with HSP70, one of the key-proteins in the foreign antigen processing [57]. To this end, we employed a combination of molecular docking with CG-MD simulations.

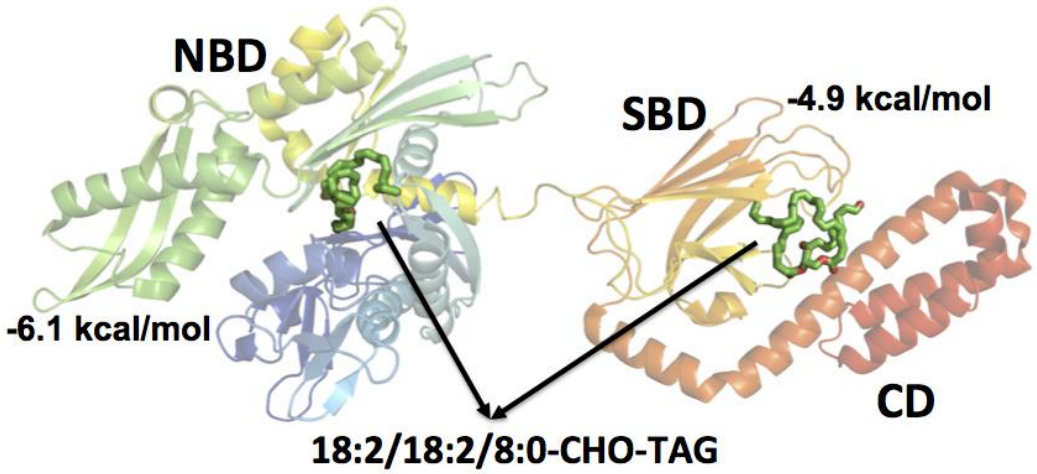

Figure 3-11 Molecular docking of truncated TAG to HSP70 domains.

Molecular docking shows a higher affinity interaction of the oxygenated truncated TAG with N-terminal ATPase domain (NAD) as compared with the substrate binding domain (SBD) or C-terminal domain (CD); Note the differences in binding energies -6.1 kcal/mol *vs.* -4.9 kcal/mol, respectively.

The molecular docking showed that oxTAG with esterified C9-ONA strongly interacted with N-terminal ATPase domain (NAD) of HSP70 with a binding energy of -6.1 kcal/mol (Figure 3-11), in contrast to a much weaker binding to the substrate binding domain (SBD) or C-terminal domain (CD) (binding energy of -4.9 kcal/mol). Thus, oxTAG displayed a higher affinity for the N-terminal domain of the HSP70 chaperon.

Next, we utilized CGMD simulations to explore the interactions of HSP70 with LD and oxLD. Since the full-length structure of human HSP70 has not been published, we employed the structure of *E coli.* HSP70 structure. The sequence analysis and alignment showed 46.5% identity and 26.3% similarity, which represent a high degree of resemblance. The CG model of *E. coli* HSP70 was built based on the MARTINI force field with application of the elastic network to maintain the overall shape of the protein [61]. To mitigate the effect of the protein alignment on the interactions with LD, the initial orientation of HSP70 was varied for each run to

generate three independent trajectories. We assessed the distance from center of mass of HSP70 to the surface of LD during 2 μs (Figure 3-12 A&B). In all three tested cases, the CGMD simulations demonstrated HSP70 interaction with oxLD – in contrast to only one out of three trials with LD. This reflects a higher probability of interactions of HSP70 with oxLD than with LD. Among three oxLD systems, HSP70 remained tightly bound to the surface of two oxLD (namely, OX1 and OX2 runs) by the end of the simulations. Interestingly, HSP70 was positioned on the oxLD surface in the same orientations for both OX1 and OX2 (Figure 3-12C).

The typical final configurations of the interactions of HSP70 with oxLD for OX1 and OX2 simulations are shown in Fig. 1D. The residue analysis of the final configuration of these simulations predicted three binding sites on HSP70 that were involved interactions with oxygenated lipid products. Binding site 3 penetrated almost 15 Å into the depth of the LD phospholipid monolayer to get in close proximity to the oxygenated lipids.

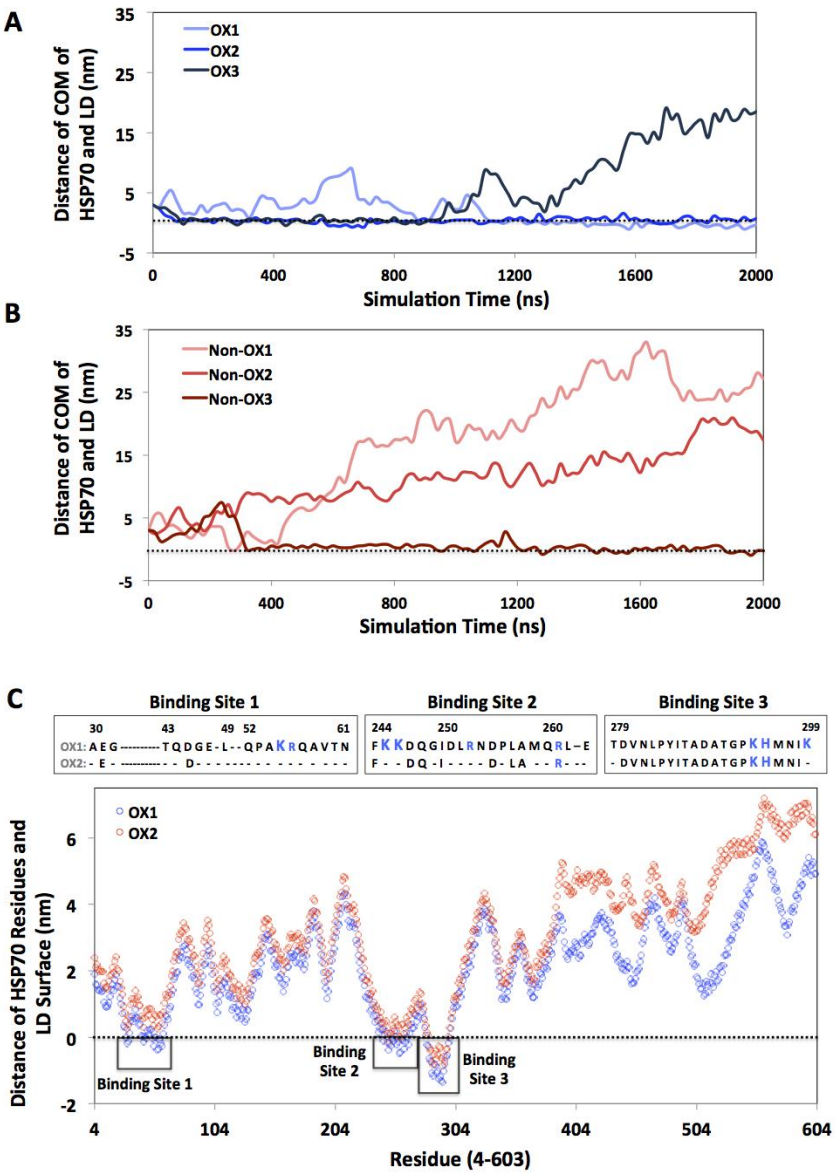

Figure 3-12 Distance analysis of HSP70/oxLD trajectories.

A&B. HSP70 interacts with oxLD in all three CGMD simulations during 2 μs runs, in which the initial orientations of HSP70 were varied as compared with the interactions in only one out of three runs with LD. C. Two out of three CGMD simulations (OX1 and OX2) showed strong interactions of HSP70 and oxLD throughout and until the end resulting in the similar final (at t = 2 μs) orientations.

The secondary structure of this binding site represents β-hairpin motif, which may facilitate the HSP70 positioning on the LD surface (Fig. 1E). Notably, all three binding sites contain at least one lysine residue that can chemically react with lipid oxidation products to yield covalent adducts such as Schiff bases [66]. Thus it is likely that interactions of HSP70 with LD containing peroxidation products will trigger "lipidation" of the protein that will "anchor" the protein to the LD.

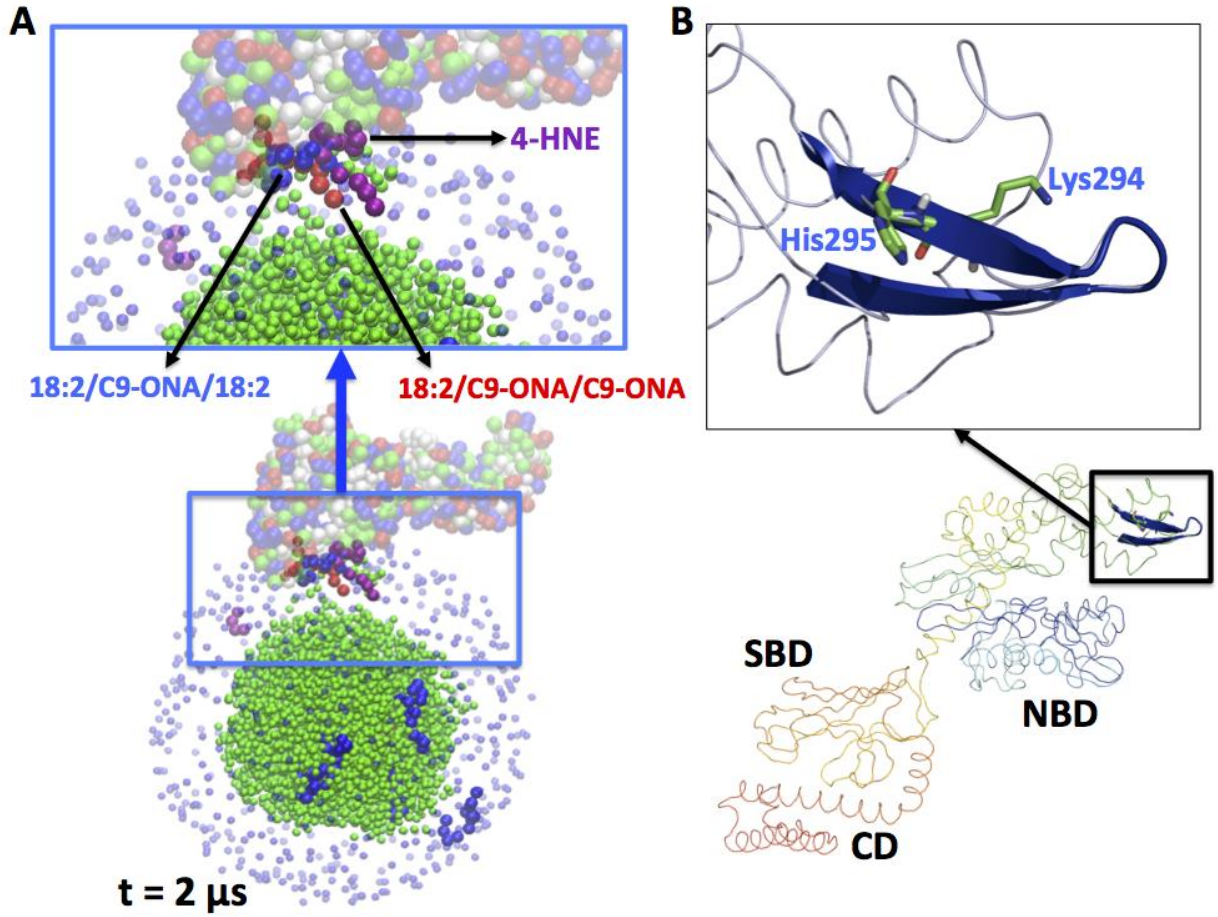

Figure 3-13 HSP70 anchored on oxLD surface using a sheet-turn-sheet like domain

A. Typical final configuration of CGMD simulations show that *E. coli* HSP70 interacts mainly with oxygenated products, including oxTAGs and HNEs present in oxLD. B. The main binding site responsible for the anchoring of HSP70 to the LD surface contains a sheet-turn-sheet motif and a positively charged Lys294 - likely involved in the covalent interactions with oxTAG.

3.5.4 Comparison with Experimental Results

Experimental results informed the computational model in several ways. First, to study the structural role of the oxygenated lipids in LD structure, we set up CGMD models of non-oxidized and oxidized LDs based on quantitative liquid chromatography/mass spectrometry (LC/MS). Specifically, the LC/MS data was used to choose the molecular species and amount of oxidized lipids (ox-lipids) in our model [65, 67].

Next, the study of the interaction of HSP70 with LD was based on experimental results. Fluorescence microscopy had shown that HSP70 co-localizes with LDs present in the tumor environment. Therefore, we studied interactions of HSP70 with oxLD to investigate how HSP70 mediates the role of ox-lipids in the ACP pathway.Our modeling data of the interactions of HSP70 and oxygenated TAGs suggested the possibility of covalent binding of HSP70 with oxTAGs, a finding that was not anticipated by the experimental studies. To validate my prediction, my laboratory colleages assessed covalent association of HSP70 with oxTAGs generated by pre-incubation of arachidonic acid (C20:4)-containing TAGs with myeloperoxidase by SDS-PAGE. This resulted in the detection of oxygenated adducts detectable in the monomeric form of HSP70 (70 kD) as well as with high molecular weight protein aggregates present in the gel (confirmed by silver staining). High molecular weight aggregates formed after interaction of HSP70 with the oxygenated products. Aggregated high molecular weight protein oligomers are characteristic products formed as a result of crosslinking of amino acid residues with lipid peroxidation products. This finding strongly validates my prediction.

3.5.5 Discussion and Conclusions

LDs are essential for the regulation of lipid homeostasis in both adipose and non-adipose tissues [49]. The dynamic features of LDs as organelles capable of changing their neutral lipids content in adaptive response to metabolic demands and conditions is maintained by a large number of catabolic and anabolic enzymes. These enzymatic assemblies are localized on the LD surfaces, and play a role in the regulatory interface between the hydrophobic core and the aqueous cytosol, as well as in membranes of other organelles, particularly endoplasmic reticulum (ER) and mitochondria [68]. Amphiphilic phospholipids, adsorbed at the interface between the interior of the LD and the surface as a monolayer, are essential for decreasing LD surface tension, creating high bending elasticity, stability, and most importantly allowing the accommodation and organization of the enzymatic lipid-metabolizing machinery [69]. The thorough control over the amounts of interface molecules between the two phases is critical to the cellular function of LDs.

Notably, oxidizable PUFA-TAGs may constitute a significant fraction of the total amount of neutral lipids in LDs. The available global lipidomic analysis of DCs present in tumor environment indicated that >60% of the total lipids comprised the oxidizable species. Remarkably, we detected significant amounts of oxidized TAGs that harbored oxygenated functionalities such as mono-oxygenated and di-oxygenated derivatives as well as oxidatively truncated TAG species. While their origin and mechanisms of formation remain to be elucidated, the appearance of TAGs with these polar oxygenated groups in the hydrophobic core on LDs may act as an important factor shifting the equilibrium properties of the LD where the perturbed balance between hydrophobic and hydrophilic groups results in altered distributions of the constituent lipids.

While lipid peroxidation has not been studied in LDs, their effects on membranes have been investigated previously [22, 70]. In particular, it has been shown that the addition of polar oxygen atom(s) to fatty acyl chains of phospholipids causes reorientation of the modified acyl chain, and results in its protrusion into the aqueous phase like "whiskers" [22, 70]. This finding suggests that peroxidation increases the affinity of hydrophobic lipid acyls for the polar aqueous phase. Indeed, our computational modeling of LDs containing oxidized neutral lipids indicated that the presence of oxTAGs inside the hydrophobic LD was thermodynamically unstable, resulting in their migration toward the hydrophilic surface. Both oxidatively-truncated TAGs and dihydroxy-TAGs disturbed the stability of the two distinctive LD phases, and their presence causes partitioning of oxTAGs into the phospholipid monolayer. Notably, increasing the content of oxTAGs from 5mol% to 10mol% enhanced the partitioning of oxTAGs into the POPC monolayer.

As a lipid storage organelle [71, 72], the neutral lipids deposited in the LD hydrophobic core should have access to lipases that facilitates their metabolism. Walther and Farese [72] hypothesized that this can be achieved via: i) an "extension" of lipases through the phospholipid monolayer to reach the required bonds of neutral lipids, or ii) penetration of neutral lipids in the PC monolayer. Our computer modeling data are compatible with the second hypothesis. Indeed, we found that a small fraction of non-oxidized TAGs also moved to the POPC monolayer. This is in line with a previous study [62] showing that in HDL cholesterol esters (ChEs) were also able to penetrate into the outer monolayer to reach to the ChE transferase protein, apolipoprotein A-1, on the surface.

The close-up snapshots of LD after 2 μs (Figure 3-9) demonstrated the presence of both oxTAGs and TAGs in close proximity to the LD surface, immediately below the choline and

phosphate groups of POPC molecules. This suggests that the "sensitive" bonds of these TAGs may be accessible to LD associated proteins. Notably, although both TAGs and oxTAGs are capable of moving into the POPC monolayer, the latter preferentially stay for a longer time in the proximity of the phospholipid monolayer over the entire time of the trajectory, while the former are not stable in the outer monolayer and fluctuate between the two LD phases.

Are the dynamics of oxTAGs and their partitioning into the LD monolayer physiologically relevant? The accumulation and presence of oxidized neutral lipids in the LD monolayer suggests their potential roles in lipid mediator signaling networks. Indeed, lipolysis of oxTAGs should generate oxFFAs – precursors of lipid mediators. In spite of the fact that this study presents a simplified model of oxidized lipid dynamics in LD, our data suggest novel mechanisms of biochemical processing of TAGs and oxTAGs that raise challenging biophysical questions.

Our CG-MD demonstration of preferred partitioning of oxidatively modified neutral lipids to the surface area is based on a model which corresponds to a relatively small LD size compared to the actual LD dimensions. Thus, our model depicts a higher curvature and a higher surface pressure at the interface, which can be addressed in future studies.

These peroxidized lipid species on LD surface could be located in the close molecular proximity to the contact sites with neighboring organelles, such as lysosomes. As a result of this proximity, the direct transfer of peroxidized lipids from LDs into lysosomes becomes possible. The exact mechanisms and pathways, through which these peroxidized lipids affect the cross presentation process, remain to be elucidated.

We found that TAGs with oxidatively modified PUFA constitute ~10% of the total amount of these neutral lipids in LDs in DCs in cancer [73]. The appearance of polar oxygenated

groups in TAGs in the hydrophobic core of LDs may be an important factor causing redistribution of LD lipids from the core towards the surface monolayer. Noteworthy, the hydrolysis of oxTAG by the LD lipases yields polyunsaturated non-oxidized and oxygenated FFA [74]. The latter can be utilized as precursors of lipid mediators with important signaling functions [75].

Among the many proteins involved in ACP, heat shock proteins —HSP70 and HSP90— play roles in translocation of exogenous antigens, either from the ER-endosome to the cytosol or from the cytosol to the proteasome. According to recent data that described the localization of HSP70 on LD surface in a tumor environment, we explored the interactions of HSP70 with oxLD and LD. We demonstrated that ox-lipids on LD surface are recognized by HSP70. Among three candidate oxTAGs-binding sites of HSP70, the site containing a β-hairpin motif deeply penetrated into the oxLD monolayer. We additionally proposed that these interactions might be irreversible due to possible covalent binding between aldehyde groups of ox-lipids and lysine residues present in the ox-lipid-biding site of HSP70. The anchoring of HSP70 on oxLD surface deviates HSP70 from its original function in ACP. In conclusion, using computational approaches, we suggest a novel mechanism of ACP suppression through interactions of HSP70 and oxLD. Therefore, we propose a biological role and pathological significance of oxidized neutral lipids accumulation at the LD surface, which block the antigen cross presentation.

4.0 CHAPTER 4: COMPUTATIONAL STUDIES OF LIPID SIGNALING IN FERROPTOSIS

4.1 SUMMARY

Ferroptosis is a newly discovered cell death pathway that is characterized by high levels of lipid hydroperoxides. Although the exact lipid peroxidation pathway is ill defined, recent findings indicated the involvement of lipoxygenases (LOXs), particularly, 15LOX. Here, a combination of computational approaches was used to identify preferred phospholipid (PL) substrates for LOXs. The catalytic mechanism of LOXs was studied as well. Using comprehensive molecular docking modeling, the binding poses and the binding affinities of various small molecules, including, esterified lipids and LOX inhibitors were assessed. The data revealed high affinity binding of vitamin E at the LOX active site compared to arachidonic acid (AA). Among phospholipids (PLs), phosphatidylethanolamine (PE) and phosphatidylinositol (PI) were predicted as the most likely substrates for 15LOX-2. Coarse-grained molecular dynamics (CGMD) simulations were applied to study the interactions of 15LOX-2 with the membrane composed of eight lipid species. Analyzing the final configuration of the bound 15LOX-2 in the membrane presented the key lipids and the main protein's residues involved in these interactions.

CGMD simulations also provided insight into the protein's orientation in the membrane. These data have been supported using orientation of protein in membranes (OPM) analysis.

4.2 SIGNIFICANCE

Ferroptosis is an iron-dependent cell death pathway discovered in 2012 by Dixon et. al. [76]. It is characterized by iron overload and enhanced levels of lipid hydroperoxides, leading to caspase- and necrosome-independent cell death. So far, glutathione peroxidase 4 (GPX4), a critical antioxidant enzyme, has been identified as a key regulator of this pathway. Depletion of intracellular glutathione results in impaired GPX4 function that is characterized by accumulation of lipid peroxides, leading to lipid peroxidation mediated cell death. Thus, identification of the pathways involved in lipid peroxidation is crucial for understanding the mechanism of ferroptosis. Current knowledge in this area implicates a central role of 15LOX in ferroptosis. Using computational approaches, we examine here, the mechanism of 15LOX activation, using its natural substrate, PUFAs, and also inhibitors. The molecular docking and molecular dynamics simulations data revealed the membrane binding mechanism for 15LOX, including the domain responsible for recognizing the hydrophobic core of the bilayer. Application of such computational approaches is expected to make significant contributions to our understanding of LOX-driven PL peroxidation signaling in ferroptosis.

4.3 INTRODUCTION

4.3.1 Ferroptosis

Multicellular eukaryotes have perfected the programmed cell death pathways to optimize tissue homeostasis, immune and stress responses, as well as embryogenesis [77]. These programs have also been shown for prokaryotes through quorum sensing, thus making cell death pathways paradoxically essential across all life forms. One of the most recently identified redox programs of cell death is ferroptosis [76]. It is genetically, biochemically and morphologically distinctive from apoptosis, necrosis, and autophagy (Figure 4-1) [78]. It has been documented that oncogenic RAS-selective lethal small molecules (RSLs) such as erastin activate this iron-dependent cell death pathway (Figure 4-2). On a global scale, redox ferro-ferric cycling of iron by microorganisms controls the planetary fate of this element in the environment [79]. In eukaryotic cells, the same electron donor-acceptor propensities of iron that define its vital role in normal physiology and metabolism facilitate the ferroptotic cell demise programs [76].

Ferroptotic death program is activated by a disruption in the coordinated cross-talk between two major redox systems: thiols and lipid peroxidation. It has been postulated that a combination of GPX4/GSH deficiency and activation of one or more putative iron-containing enzymes generate oxygenated lipids that act as the proximal signals for ferroptotic cell death [80].

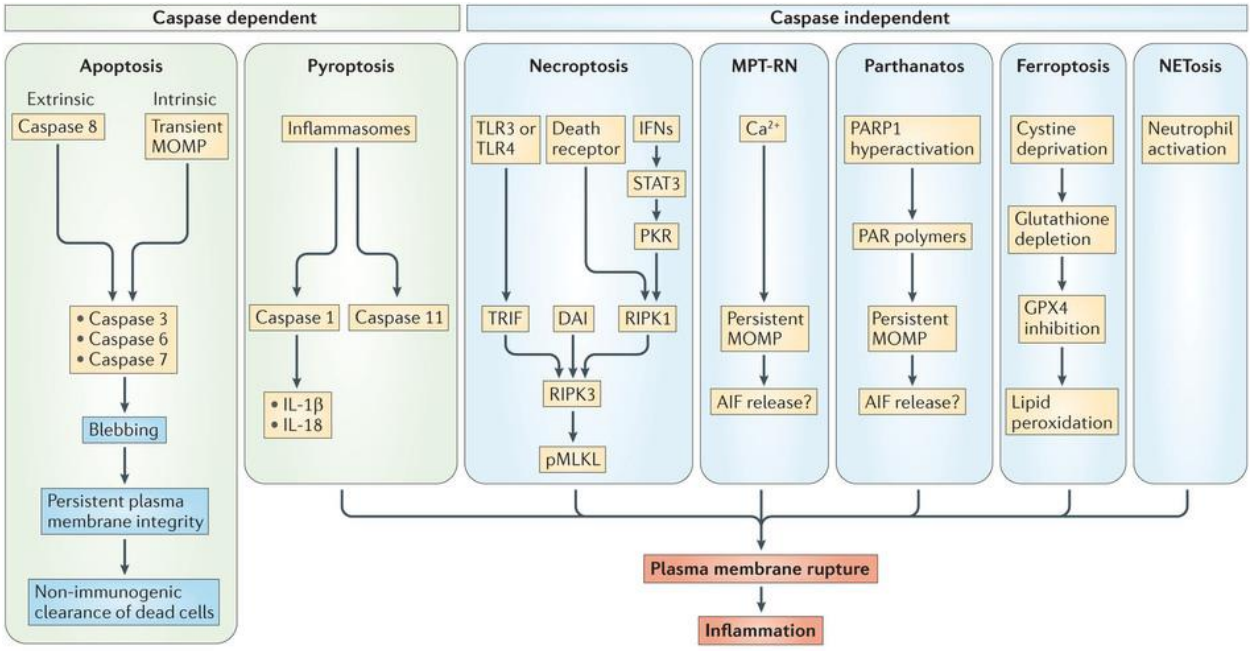

Figure 4-1 Ferroptosis is distinct from apoptosis, necrosis, and autophagy.

Regulated cell death (RCD) pathways can be classified by whether or not they are caspase dependent. Ferroptosis is a caspase-independent form of RCD and are highly immunogenic (adapted from [78]).

Among the specific features of ferroptosis, there are: i) deficiency/inactivation of phospholipid hydroperoxides metabolizing enzyme, GPX4 [81, 82]; ii) sensitvity to iron chelators [76]; iii) rescue by long-chain polyunsaturated fatty (arachidonic) acid specific acyl-CoA synthase (Acsl4) [83] and lysophospholipid acyl transferase [83], and iv) suppression by vitamin E [76, 81]. Thus, the process of lipid peroxidation is central and specific to the execution of ferroptosis [76, 80, 82].

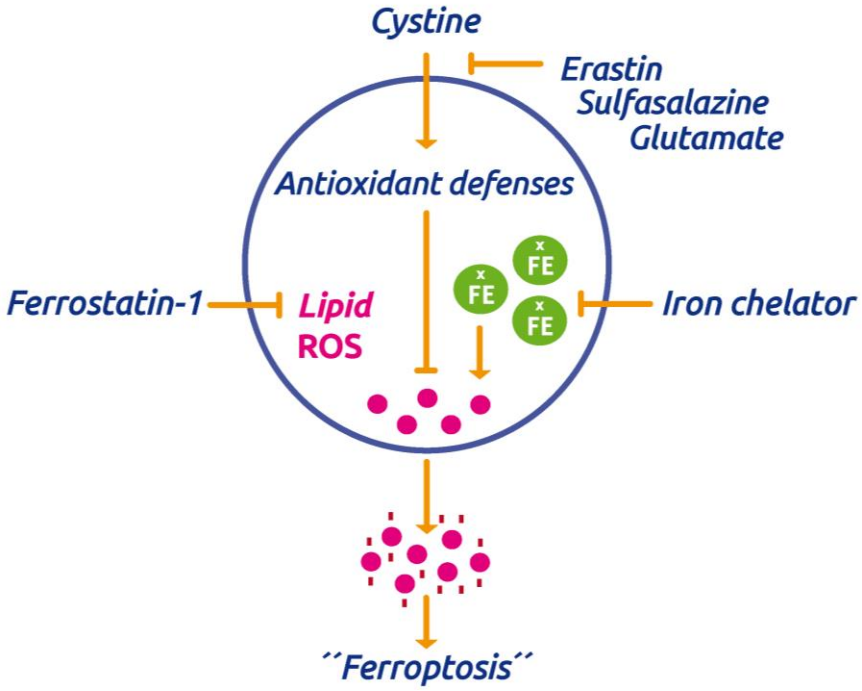

Figure 4-2 Ferroptosis is similar to glutamate-induced excitotoxicity.

It is triggered by inhibition of cystine uptake. Iron chelators are the primary inhibitors of this newly identified cell death pathways (from http://being-bioreactive.com/).

In spite of the numerous indications pointing to the lipid involvement in ferroptosis neither has *direct* evidence for lipid peroxidation, nor has the nature of oxygenated lipid species triggering cell demise been identified. Recent data suggest that oxygenated species of arachidonoyl- and adrenoyl-diacyl-phosphatidylethanolamines (AADiPEox and AdADiPEox) are strong predictive biomarkers of ferroptotic cell death in vitro and in vivo (unpublished data). It has further been documented that the lipoxygenases are key players in the ferroptosis cell death pathway.

4.3.2 Lipoxygenases

LOXs are a family of non-heme, iron-containing enzymes that catalyze the dioxygenation of polyunsaturated fatty acids in lipids containing a cis,cis-1,4-pentadiene structure. The phylogenetic tree of LOX family enzymes is shown in Figure 4-3 [84]. The number assigned for each LOX is based on the specificity of the enzyme acting on its substrate. For instance, 12-LOX oxygenated arachidonic acid (AA) at carbon-12. "R" or "S" is used to specify the stereochemistry for these enzymes (12R-LOX or 12S-LOX).

The plant and animal LOXs have many common features, including an amino terminal β-barrel, now known as a PLAT (Polycystin-1, LOX, Alpha-Toxin) domain and a much larger α-helical domain that houses the catalytic iron (Figure 4-4A). The animal enzymes are significantly smaller than the plant enzymes (~650 vs ~900 amino acids, respectively). The iron atom located at middle of the "J-shaped" active site (Figure 4-4B), is ligated with 5-6 amino acids, including 3-4 histidine (Figure 4-5) [85]. LOXs use their iron to catalyze the following reaction [86]:

$$\text{Fatty acid} + O_2 \rightarrow \text{fatty acid hydroperoxide}$$

Although free AA is the main substrate of AA, there are a few studies on oxygenation of esterified AA using LOXs, particularly 15-LOX.

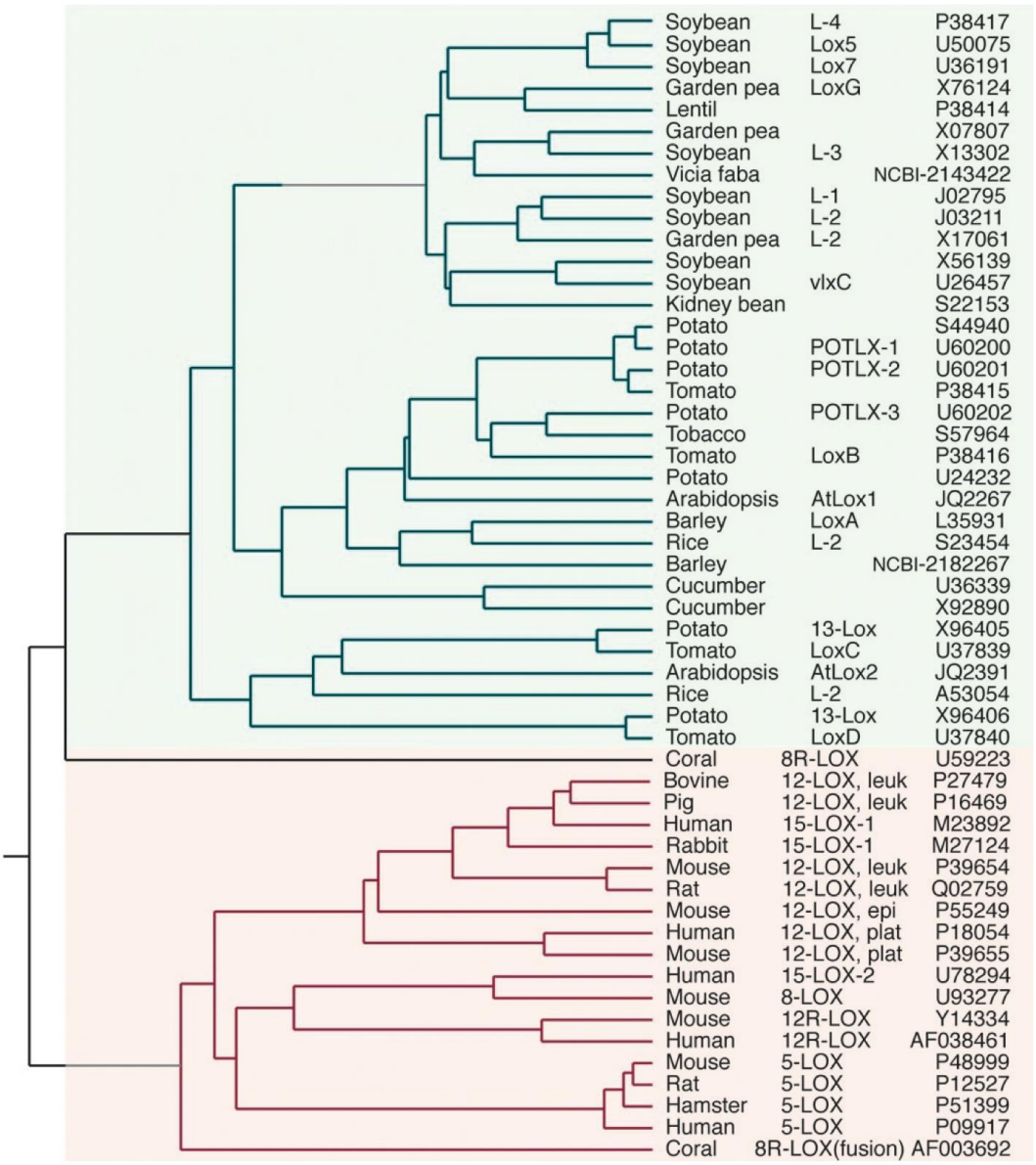

Figure 4-3 Lipoxygenase phylogenetic tree.

Representative plant and animal lipoxygenases were compiled into the phylogenetic tree using MegAlign (DNASTAR, Inc.) (adapted from [84]).

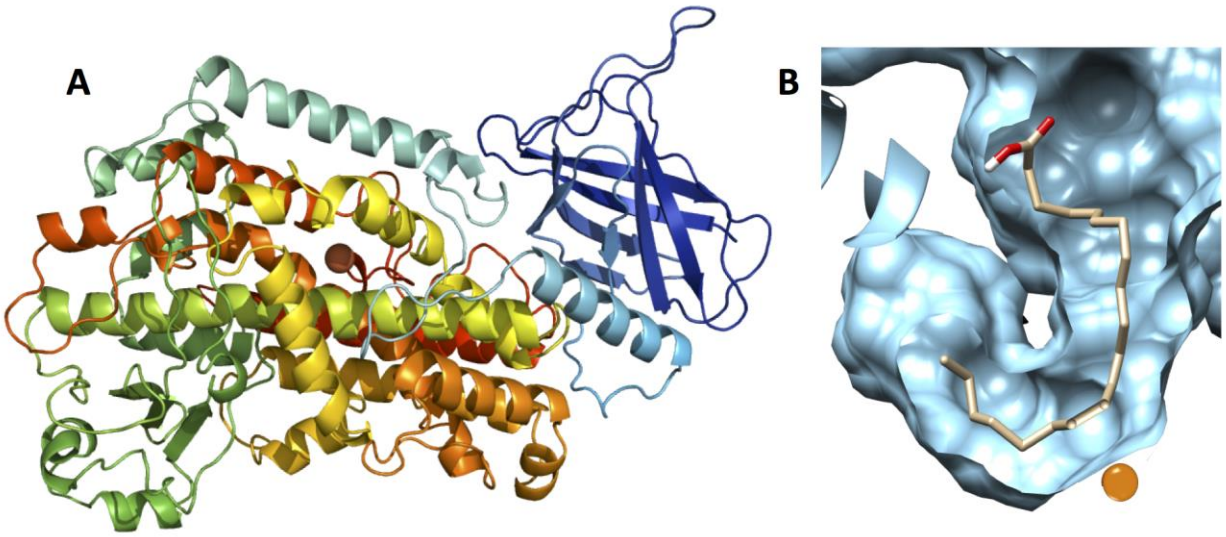

Figure 4-4 Structure of human 15-LOX-2.

A. Structure, and **B.** active site containing AA, based on PDB ID: 4NRE [29].

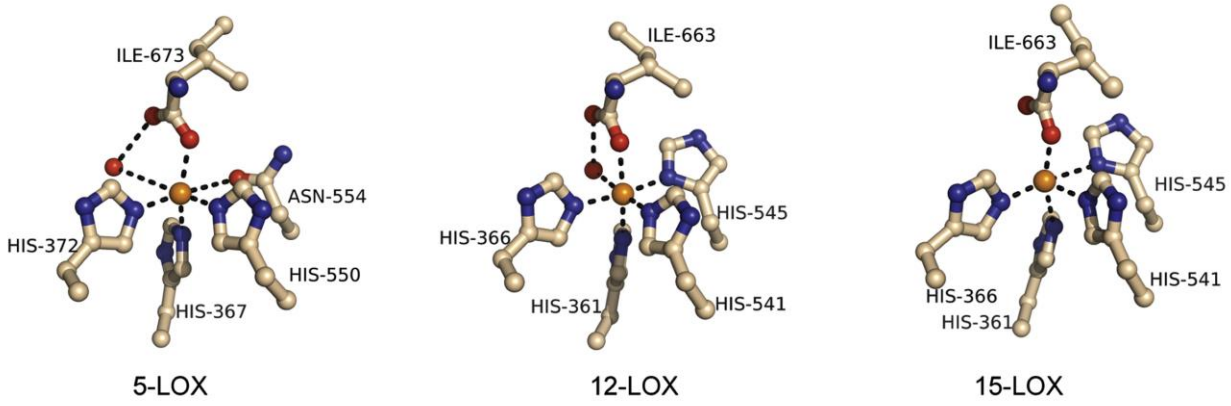

Figure 4-5 A comparison of the iron coordination environments for the mammalian LOXs.

The iron environment in 12-LOX is much closer to a six coordinate octahedral geometry than in 5- or 15-lipoxygenase. The central spheres represent the iron atoms [85].

The overall peroxidation process is assumed to initiate from hydrogen abstraction from the $–CH_2–$ group lying between the two –HC=CH– groups of AA by the Fe(III)–OH moiety (Figure 4-6) [87]. The whole process occurs throughout four steps. First, an electron goes to the

iron center, and a proton goes to the –OH, through a process known as proton-coupled electron transfer (PCET) (structure I). Second, molecular oxygen (O_2) attacks the substrate (structure II). Third, structure II lowers the energy by transferring to structure III. Lastly, structure III is reduced via transfer of a H from the Fe(II)–OH_2 moiety to give the final anticipated hydroperoxy product (structure IV) [87]:

Figure 4-6 The general substrate peroxidation mechanism by LOXs [87].

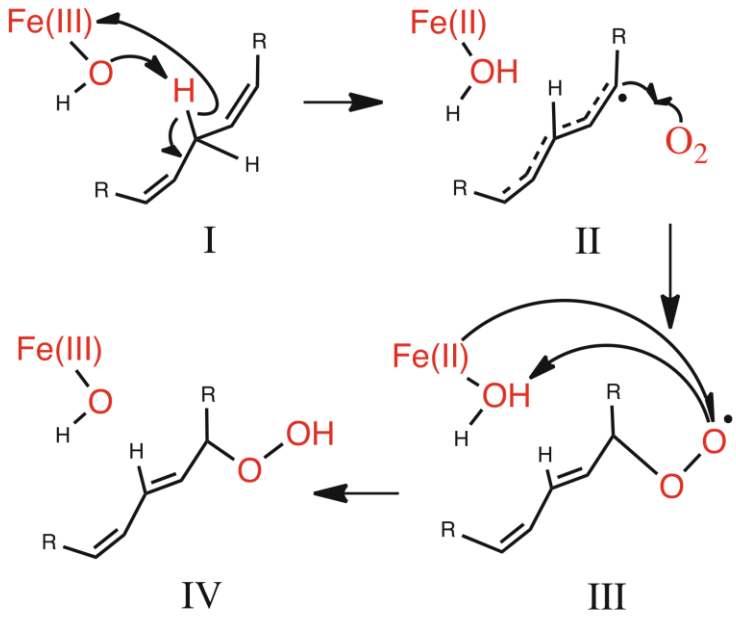

LOXs are multi-functional enzymes to produce diversified produces. The main substrate of LOXs, AA, can be oxygenated not only at a major site (C-12 for 12-LOX and C-15 for 15-LOX) but also at alternate sites (C-15 for 12-LOX and C-12 for 15-LOX). Hence, more than one product can be formed using a single enzyme. Moreover, LOXs can oxygenate an AA at multiple sites. Furthermore, the primary hydroperoxides can be converted to epoxy [86].

4.4 APPROACH

Determining LOX charge: Protein Calculator v3.4 —an online server (http://protcalc.sourceforge.net) to calculate protein properties based on a sequence— was used to predict the total charge of 15LOX-2 at various pH's, and to estimate its isoelectric point (IP). The results are provided in Table 4-1.

Table 4-1 15LOX-2 molecular weight, isoelectric point and charge.

Isotopically averaged molecular weight	Estimated isoelectric point (PI)	Charge at pH					
		6.0	6.5	7.0	7.5	8.0	8.5
78019.97	6.47	7.5	-0.6	-8.0	-12.9	-16.7	-21.3

Sequence and structure alignment: The full-length structure of human 15LOX-2 and human 5LOX are available in PDB database (PDB ID's: 4NRE and 3O8Y, respectively). However, the porcine leukocyte 12LOX coordinate file (PDB ID: 3RDE) contained only the C-terminal active site domain of the protein, but not the N-terminal membrane binding domain. Therefore, we used BLAST sequence alignment server [88] to compare 12LOX and 15LOX sequences. The results described 36% identity and 50% similarity, which convey a high level of resemblance. Subsequently, 3D structures of the active site of these two enzymes were compared using PDBeFOLD online server -protein structure comparison service PDBeFold at European Bioinformatics Institute [89]. Interestingly, RMSD value of 1.30 and Q-score of 0.61 represent that the 3D structures of porcine 12LOX and human 15LOX-2 are also closely similar. However, about 40% mismatch in 3D structure may represent significant variations in their functions, as 15LOX mainly oxygenates AA at C-15, but 12LOX peroxidases its substrate predominantly at C-12.

Molecular docking: A molecular docking modeling was employed to study interactions of free/esterified fatty acids and known/proposed inhibitors with 5, 12 and 15LOX structures. Due the large size of LOXs, we applied a large grid boxes for our docking. Due different number of residues and enzyme's size we used grid boxes with dimensions of 80 × 70 × 102 Å, 84 × 76 × 78 Å and 112 × 102 × 72 Å for 5LOX, 12LOX and 15LOX respectively. Three docking modeling were run using three different random number generator seeds, with exhaustiveness set at 14 to obtain a higher accuracy to find the binding site and reduce the discrepancies among the obtained binding affinities. The best models were designated based on the lowest binding energies for lipids selective bound at the LOX active site

CGMD simulations: CGMD simulations were applied to study the interactions of LOX with the membrane composed of six classes of PL. CGMD simulations provided insights regarding protein binding to the membranes, which explained the differences in activity of LOX towards the different PLs. Furthermore, the key residues during the recognition and stabilization stage of the interactions were identified. Analysis of the final configuration of the CGMD runs revealed the preferred PL substrate of 15LOX-2.

4.5 RESULTS AND DISCUSSIONS

In this study, using molecular modeling we examined the mechanism of LOX-dependent lipid signaling in ferroptosis. To this end, the binding of free and esterified fatty acids to three different LOXs were carefully examined to find out what are the favored substrates in this family of enzymes.

4.5.1 LOX Catalytic Mechanism and Preferred Substrates

LOX's are believed to play a central role as peroxidases in ferroptosis mediated cell death, that is driven by massive oxidation of PLs. Yet, the mechanism of PL binding to the catalytic site of LOX's has never been studied. Here, for the first time, we applied molecular modeling, to study the mechanism of PL binding to the LOX active site, and consequently predict the preferred PL substrate of LOX, in an effort to identify the PL species critical for ferroptosis. Our studies were primarily focused on the 15LOX-2 isozyme, which is the most prevalent in ferroptosis, and its substrate, arachidonic acid (AA).

4.5.1.1 Role of R429 on oxygenated products

We initially examined the interactions of AA —an established substrate of the LOX enzyme family, with 15LOX-2, using rigid and flexible molecular docking. In rigid docking all the residues of the receptor are considered immobilized. The binding pose analysis of the rigid docking represented "tail-in" orientation of AA in J-shape active site of LOX (Figure 4-7A). The binding affinity of the top-ranked model was -7.4 kcal/mol. Henceforth, this model will be used as a positive control. The tail-in orientation results in preferential oxygenation of AA at C-15, with a lower favorability for the C-12 double bond. This binding is stabilized with many hydrophobic residues in the active site and charged groups located at the opening of the active site. For rabbit reticulocyte 15S-LOX (PDB ID: 2P0M) —a homologue of human 15LOX-2— it has been proposed that R403 is responsible to stabilize the carboxylic group of AA [90, 91]. R429 is the only positively charged residues placed in close vicinity of the active site opening in human 15LOX-2. Using docking, we predicted the side chain of R429 plays a similar role as R403 in rabbit 15LOX to form a salt bridge with COOH group of AA.

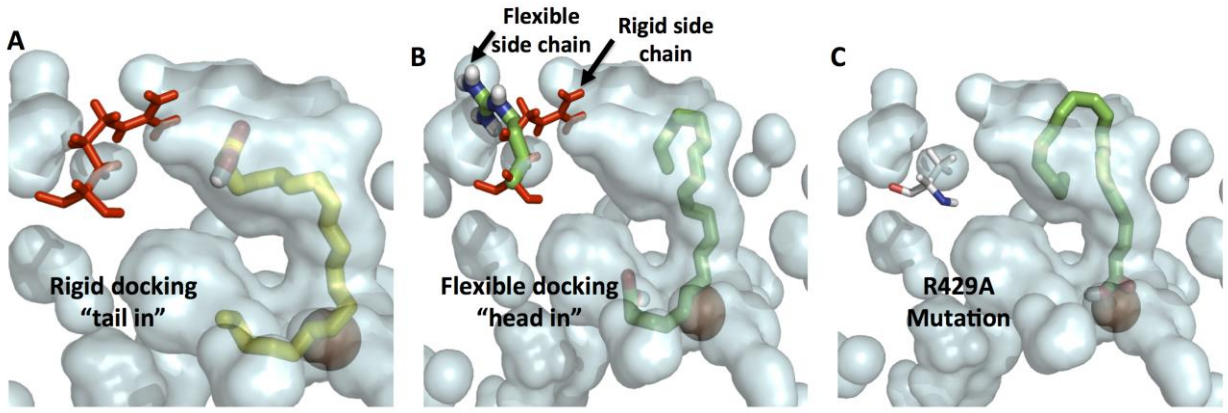

Figure 4-7 Molecular docking data shows R429 is stabilized the tail in orientation of the substrate in the active site of 15LOX-2.

A. The tail in orientation of AA using rigid docking. **B.** The head in orientation of AA in flexible docking while the site chain of R429 moves away. **C.** The head in orientation of AA in R429A point mutation experiment.

In flexible docking the dynamics properties are assigned to one or more selected residues. The data from flexible docking demonstrated that the dominant orientation of AA is "head in", while the side chain of R429 mostly moved away from its crystalized location. The top-ranked model showed binding affinity of -7.3 kcal/mol. The "head in" orientation facilitates the oxygenation at C-7 or C-9. We deduced that the flexibility R429 side chain, which supposed to occur *in vivo*, may vary the oxygenated products.

We further evaluated the role of R429 by mutating it to an uncharged amino acid, such as Alanine. Among the nine generated models, the head in orientation was dominant in the mutant. Interestingly, R429A mutation reduced the binding affinity dramatically to -6.0 kcal/mol highlighting the necessity of R429 to stabilize the substrate in the catalytic site.

4.5.1.2 Interactions of 5, 12 and 15LOX with free fatty acids

Comparing the interactions of four free polyunsaturated fatty acids (PUFAs) with 5, 12 and 15LOX (Figure 4-8) revealed that each LOX interacts with all four free PUFAs with almost similar binding affinities. A typical binding pose of free PUFAs in catalytic site of 15LOX-2 illustrated in Figure 4-9. AA, lineolic acid (LA), eicosapentaenoic acid (EPA) and docosahexaenoic acid (DHA) bind to 15LOX-2 catalytic site with binding energies of -7.0 ± 0.7, -6.5 ± 0.1, -6.3 ± 0.3 and -7.0 ± 1.6, respectively.

Figure 4-8 The binding affinities of four polyunsaturated fatty acids (PUFAs) with 5, 12 and 15LOX.

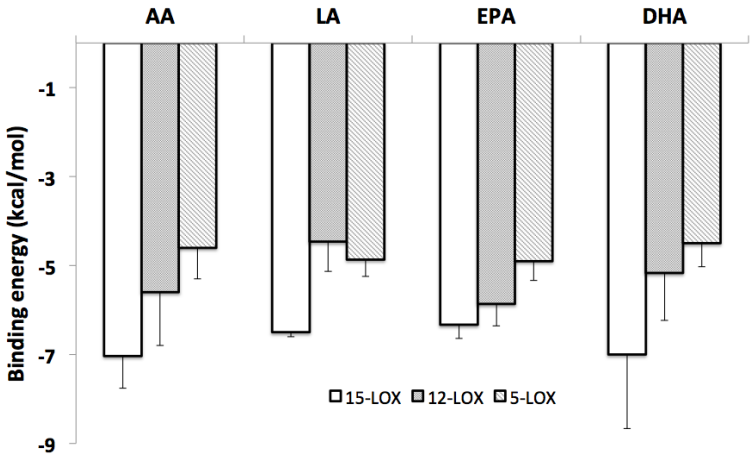

Among the three LOX isozymes, the binding affinities for the FA decrease in the order 15LOX > 12LOX > 5LOX (Fig. 1-8). While the reason for the difference in affinities among isozymes having similar 3D structures is unclear, these data highlight a likely prominent role for 15LOX in ferroptotic cell death, over other LOX isozymes.

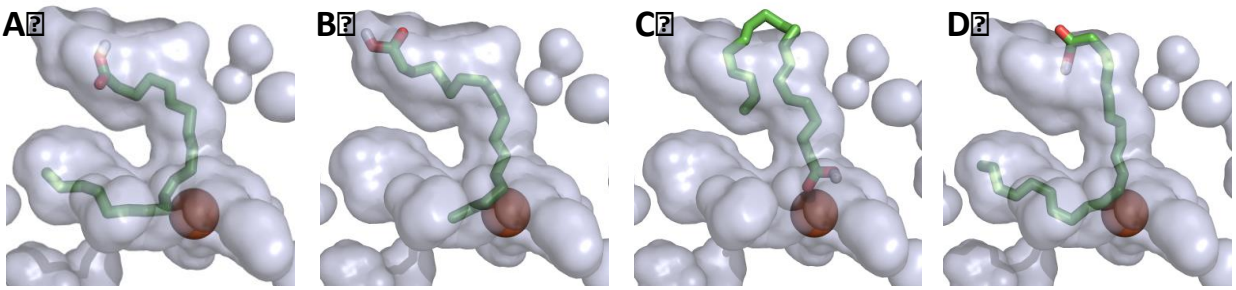

Figure 4-9 A typical binding pose of (A) AA, (B) LA, (C) EPA and (D) DHA to 15LOX-2.

In addition to AA, which has a physiologically important substrate in ferroptosis, other FAs, including the longer chain "adrenic acid (AdrA)" have also been identified. The close binding affinities and high degrees of similarity of the binding poses of AA and AdrA suggested that they have equal susceptible of oxygenation via LOXs (Figure 4-10).

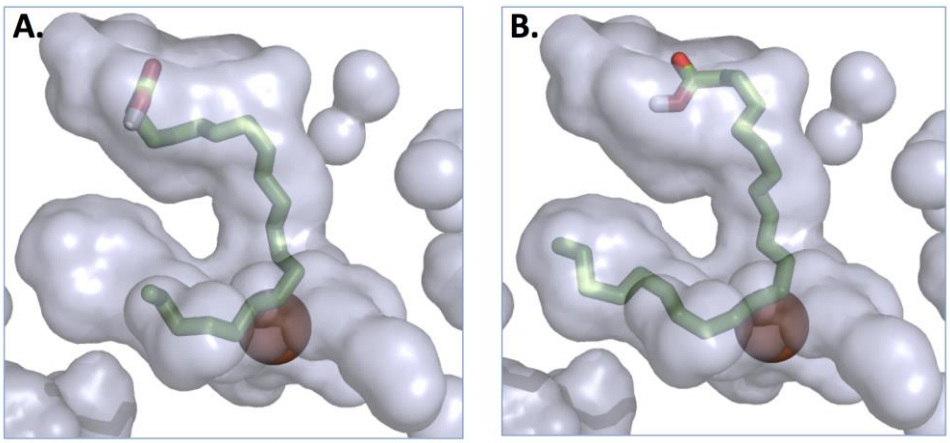

Figure 4-10 AA and AdrA are equally susceptible to be peroxidized via 15LOX-2.

Molecular docking shows the structural arrangement of 15LOX-2 active site perfectly fit to accommodate both AA (A) and AdrA (B) (with the binding energies of -7.0 ± 0.7 and -6.9 ± 0.4, respectively (n=3)), denoting almost equal susceptibility of the oxidation of these free fatty acids.

4.5.1.3 Interactions of 5, 12 and 15LOX with phospholipids

According to the recent experimental data (unpublished), PUFA-containing phospholipids (PLs) are susceptible to be substrates of LOXs. Accordingly, we explored PUFA-containing PLs, specially those containing AA, to identify the preferred PL substrate of LOXs.

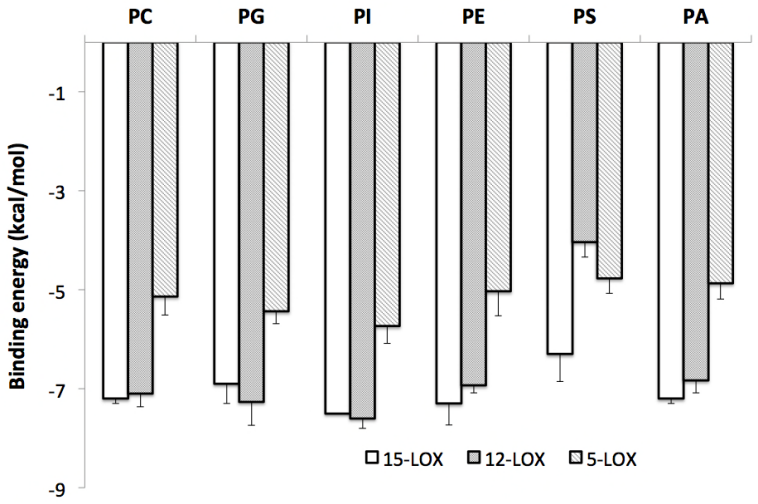

Figure 4-11 The PLs mainly bind to 12 and 15LOX with relative high affinities. PLs contain stearic acid (18:0) and arachidonic acids (20:4) chains bind to the active site of LOXs with almost similar binding energies. PS demonstrates low affinities to all three LOXs.

Among all six SA-based PLs, 1-stearoyl-2-arachidonoyl-sn-glycero-3-phospho-L-serine (SAPS) demonstrated the lowest binding affinities toward all three LOXs (Figure 4-11). Although SAPI exhibited the highest binding affinities, the binding energies of SAPC, SAPG, SAPI, SAPE and SAPA are comparable. In case of 15LOX-2, the binding energy of SAPS is significantly lower than other PLs. Therefore, we conclude that SA-based PL's are potential substrates of 15LOX-2 except SAPS, which binds with a substantially lower binding energy comparing other PLs. Using molecular docking we were unable to identify the best PL substrate of 15LOX-2. The *in vitro* and *in vivo* data, however, demonstrated different effects for various PLs. For instance, *in vitro* experiments using liposome, 15LOX-2 and low amount of peroxidase as an activator showed that the preference for PL decreased in the order PA > PG > PE at 31.6%, 14.7% and 9.6% respectively. Consistent with modeling data, PS showed the lowest level of oxidation comparing

other PLs (2%) On the other hand, *in vivo* data revealed that PI and PE were (per)oxidized dramatically higher than other PLs –data from the global analysis of the ox-lipids in GPX4 deficient cells.

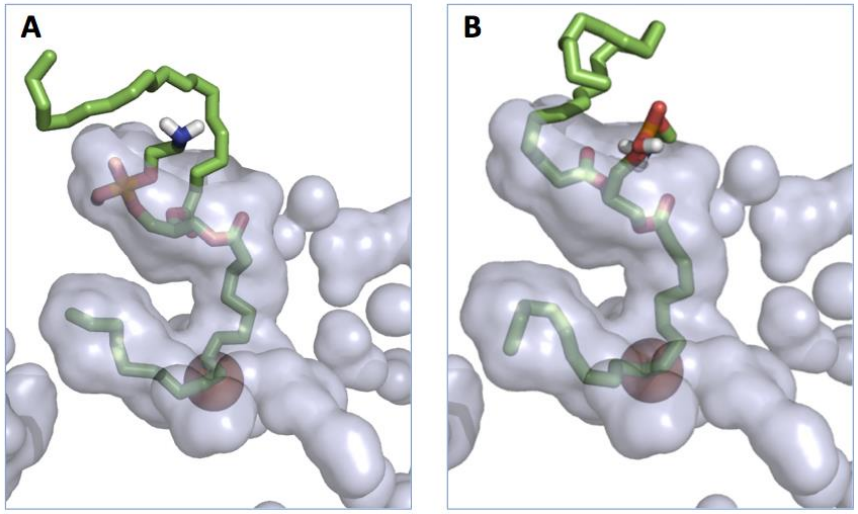

Figure 4-12 SA-PE and SAdr-PE are equally susceptible to be peroxidized via 15LOX-2.

The molecular docking results explained that two typical PE species containing PUFA, including PE(18:0/20:4) (A) and PE(18:0/22:4) (B) bind to 15-LOX-2 active site with binding energies of -7.2 ± 0.4 and -6.8 ± 0.2 respectively (n=3) demonstrating high degrees of structural and binding affinities resemblance.

The correlation of cell death and lipid oxidation explained that PUFA-containing PEs are potential signals and biomarkers of ferroptosis. Consequently, we have examined the structural arrangement of two key players of PE-having polyunsaturated acyl chains (18:0/20:4, and 18:0/22:4), in the active site of 15LOX-2 using docking method. It can be seen that both species of PE binds analogously in the catalytic site with highly similar binding affinities (Figure 4-12).

4.5.2 Interactions of 15-LOX-2 and a ER-membrane Mimic

Next, we utilized CGMD simulations (two trails for 2 μs) to carefully examine the interactions of 15LOX-2 with membrane. Based on the fluorescence microscopy data, ER is actively involved in ferroptotic cell death. Accordingly, we used a lipid composition approximately mimicking the ER-membrane (Table 4-2) [92].

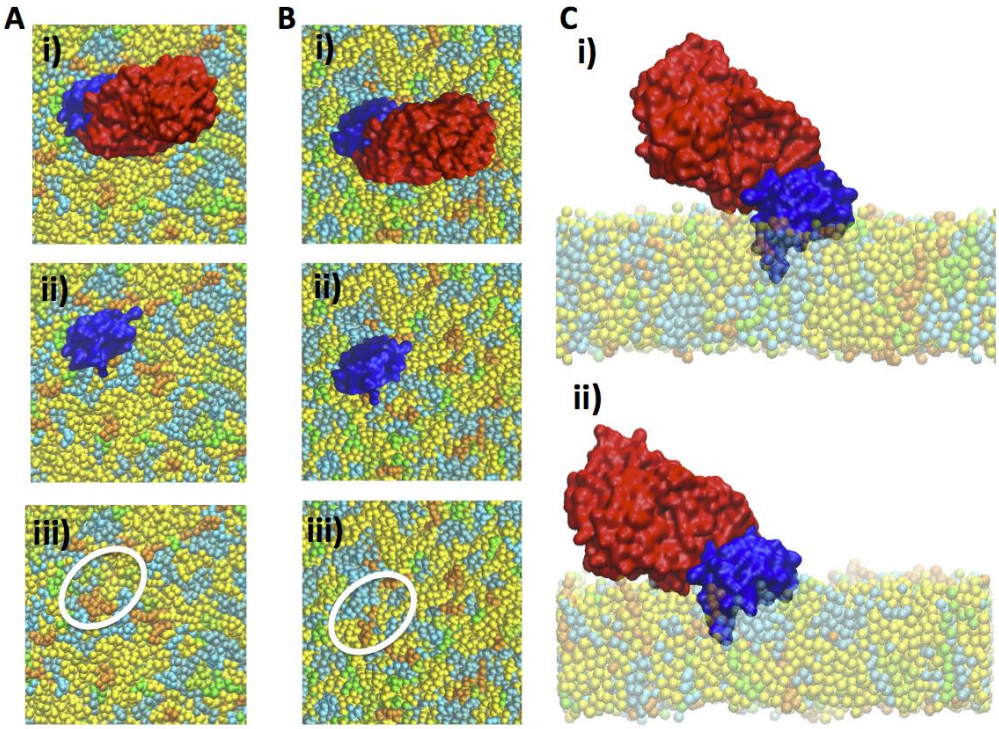

Figure 4-13 CGMD simulations of the interactions of 15LOX-2 with a ER-membrane mimic.

A and **B.** CGMD1 and CGMD2; i. 15LOX-2 interacting with the membrane with its amino-terminal β-barrel domain called PLAT (polycystin-1-lipoxygenase α-toxin) domain (blue); ii. the helical active site was removed (for clarity) to compare the orientation of the PLAT domain on the membrane; iii. whole protein was removed to illustrate the interacting lipids with PLAT domain. Representation guide: yellow: three species of PC (DPPC, pOLPC and SAPC); orange: SAPI; cyan: two species of PE (SAPE and pSAPE); green: two species (SOPS and SAPS); blue: PLAT domain; red: α-helical catalytic domain.

CGMD data confirmed that the amino-terminal β-barrel domain called PLAT (polycystin-1-lipoxygenase α-toxin) domain of 15LOX-2 is responsible for membrane binding (Figure 4-13A & B). Although in both runs the PLAT domain was oriented analogously in the membrane, the alignment of the helical active site was slightly varied.

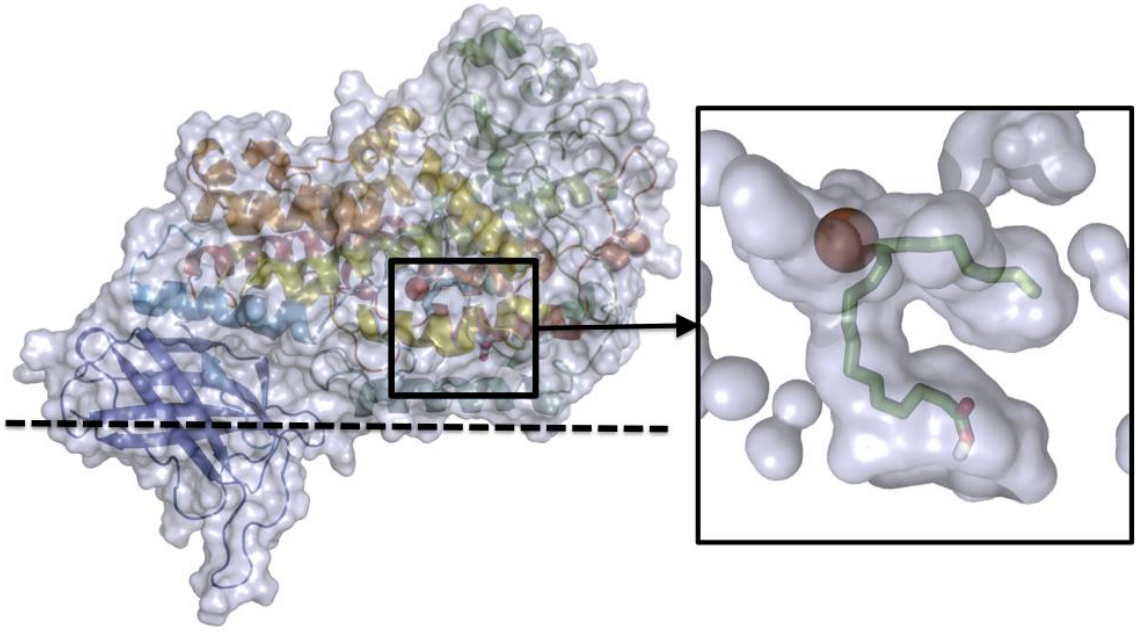

Figure 4-14 The reconstructed predicted orientation of 15LOX-2 in the membrane —based upon CGMD simulations— to identify the location of the catalytic site opening versus surface of the membrane.

Cartoon representation colored in spectra from blue to red denoting N- to C-terminal. Red and green spheres representing iron and calcium. The zoomed in panel shows that the active site opening is located on top of the membrane surface.

It should be noted that 15LOX-2 deeply penetrates in the membrane. The analysis of the interacting lipid represented that the PLAT domain even interacts with lipids on the opposite leaflet. The PLAT interacts with five and three lipids in CGMD1 and CGMD, respectively. In CGMD1 the PLAT domain interacts with two PC (16:0/16:0), one pPC (18:1/18:2), one PI

(18:0/20:4) and one PE (18:0/20:4). In CGMD2, however, only two PC (16:0/16:0) and one PE (18:0/20:4) were involved in the interactions with the PLAT domain.

To establish the positioning of the catalytic site opening and its orientation versus the membrane surface, we reconstructed the enzyme orientation in the membrane based on CGMD data. The surface and cartoon representations of 15LOX-2 were merged and oriented similar to CGMD2 binding configuration. The magnified J-shaped catalytic site (using the cavity representation of PyMol software) exhibited the approximate arrangement of the opening against the membrane surface (Figure 4-14).

A loop at the interface of the PLAT domain and helical active site in the crystal structure of 15LOX-2 (residues 120 to 132, EGTAKVSWADHH) acts as a hinge providing some degrees of flexibilities for helical domain while the PLAT domain is firmly bound in the membrane. Therefore, the position of the catalytic site opening varies due to the movement of whole helical domain. This motional feature can be connected to the activation mechanism of LOX's, which needs further investigations.

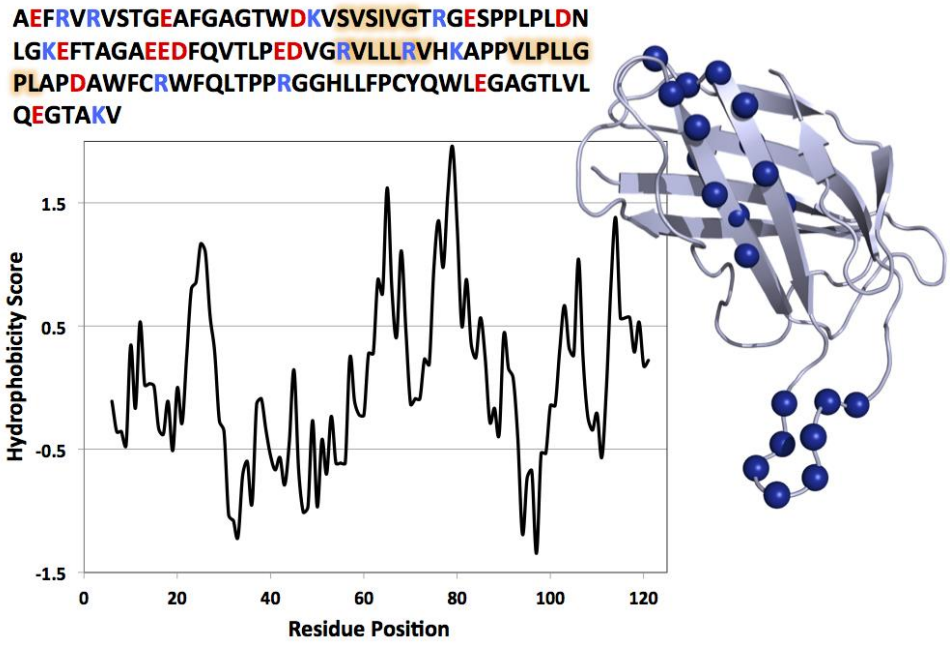

Figure 4-15 The hydrophobic analysis of the PLAT domain of 15LOX-2.

The residues around 80 present the longest coil in 15LOX-2, which should be responsible in initiating hydrophobic interactions with membrane hydrophobic core.

Table 4-2 The analysis of interacting lipids with NMBD of 15LOX-2.

Lipids present in the bilayer	Total number of lipids in each leaflet	Percentage of lipids in each leaflet	Number of lipids interacting with LOX (CGMD1)	Percentage of the interacting lipids (CGMD1)	Number of lipids interacting with LOX (CGMD2)	Percentage of the interacting lipids (CGMD2)
PC (16:0/16:0)	160	40.0	1	0.6	6	3.8
pPC (18:1/18:2)	40	10.0	0	0.0	0	0.0
PC (18:0/20:4)	20	5.0	2	10.0	0	0.0
PI (18:0/20:4)	28	7.0	2	7.1	2	7.1
PE (18:0/20:4)	80	20.0	0	0.0	3	3.8
pPE (18:0/20:4)	40	10.0	2	5.0	4	10.0
PS (18:0/18:1)	28	7.0	0	0.0	0	0.0
PS (18:0/20:4)	4	1.0	0	0.0	0	0.0

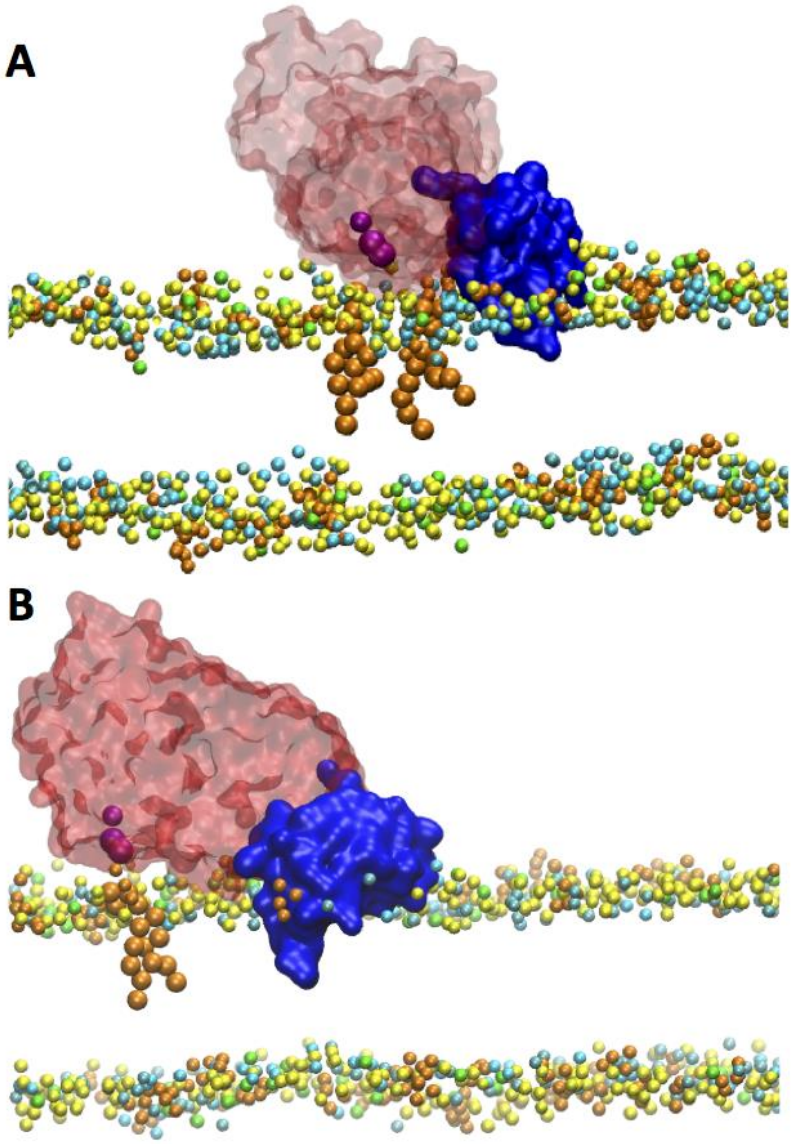

Figure 4-16 SAPI is the only PUFA-containing phospholipid in 15Å distance of the catalytic site of 15LOX-2. The side view of the final configurations of CGMD1 and CGMD2 representing the only PL is in 15Å distance of the opening of the catalytic site of 15LOX-2. The distance was measured from the location of R429 residue, which is located at the entrance of the J-shape active site. Representation guide: yellow: three species of PC (DPPC, pOLPC and SAPC); orange: SAPI; cyan: two species of PE (SAPE and pSAPE); green: two species (SOPS and SAPS); blue: PLAT domain; transparent red: α-helical catalytic domain; purple: R429.

To discover the binding domain recognizing the hydrophobic core of the membrane, we calculated the hydrophobic indices of PLAT domain residues (Figure 4-15). The data suggested that β-hairpin structure consisting highly hydrophobic amino acids around residue 80 are the membrane recognition domain, in line with a study was done by Kobe et al [29].

Next, we analyzed the interacting lipids involved in binding. In CGMD1, the lipids interacting in order of PC > PI > PE, and in CGMD in order of PE > PI > PC. To considering the concentration of the lipids in the membrane, the percentage was calculated based on the original number of lipids in the membrane. The discrepancy in the data suggested that lack of specificity of lipids to interact with PLAT domain (Table 4-2).

We further searched for the lipids around the active site, while no direct interactions with the membrane were observed. In both CGMD runs, only SAPI is located close the active site opening, which suggest feasibility of PI lipids to be oxidized via lipoxygenases (Figure 4-16). The measurements were performed based on the position of R429 residue located at the close proximity of the active site opening.

4.5.3 Can Inhibitors of Ferroptosis Potentially Inhibit LOXs?

The LOX inhibitors can be categorized into 5 groups; (i) redox inhibitors interfering with the valency change of iron during the catalytic cycle, (ii) iron chelators making complex with iron ion at the active site, (iii) compounds binds to active site competing with substrate AA binding, (iv) suicide substrates leading to inactivate the enzyme and (v) allosteric inhibitors. Here, we evaluated several known and proposed inhibitors of LOX family enzymes, particularly 15LOX (or 12/15LOX) inhibitors. We mainly tested the inhibitors that have been reported to block ferroptotic cell death [25] to test our hypothesis that “the LOXs inhibition impede ferroptosis

cell death". Baicalein, a known inhibitor of 15LOX —not tested for ferroptosis— was used as a positive control. We next explored the inhibition mechanism of LOXs using vitamin Es. Firstly, the chemical properties and structures of inhibitors will be introduced. Secondly, their structural arrangements in the catalytic site of 15LOX-2 and their binding affinities will be reported.

4.5.3.1 Structures of ferroptosis/LOXs inhibitors

Zileuton (trade name ZYFLO) (Figure 4-17A) is an active inhibitor of 5LOX enzyme, and thus inhibits leukotrienes (LTB4, LTC4, LTD4, and LTE4) formation. Zileuton is used for treatment of asthma [93]. It is a tested inhibitor of ferroptosis showing a strong effect to hinder ferroptotic cell death.

PD 146176 (Figure 4-17B) is a potent inhibitor of reticulocyte 15-LOX-1. It an anti-oxidant agent for stress-induced apoptosis in endothelial cells. In addition, it lacks significant non-specific antioxidant properties [94]. It is a tested inhibitor of ferroptosis demonstrating a strong effect to hamper ferroptosis with low doses; however, cell viability decreased significantly using higher doses.

Baicalein (5,6,7-trihydroxyflavone) (Figure 4-17C) is a flavone, originally extracted from the roots of Scutellaria baicalensis and Scutellaria lateriflora. In addition of inhibition of 12/15LOX [95], it has been shown baicalein acts as an anti-inflammatory agent as well [96]. It is known for its antioxidant properties. Baicalein also has never been examined to inhibit ferroptosis. We have employed this compound as a known inhibitor of 15LOX to compare binding energies of other inhibitors.

MK-866 (Figure 4-17D) is an inhibitor 5LOX involved in leukotriene biosynthesis (IC_{50} = 3 nM in human polymorphonuclear leukocytes). MK866 inhibits 5-LOX-activating protein (FLAP). It blocks and reverses the membrane association of 5-LOX [97]. Conversely, MK 866 induces

apoptosis through the mitochondria-dependent pathway [98]. MK-866 also is an examined ferroptosis inhibitor, which does not revealed a strong inhibition even in high doses.

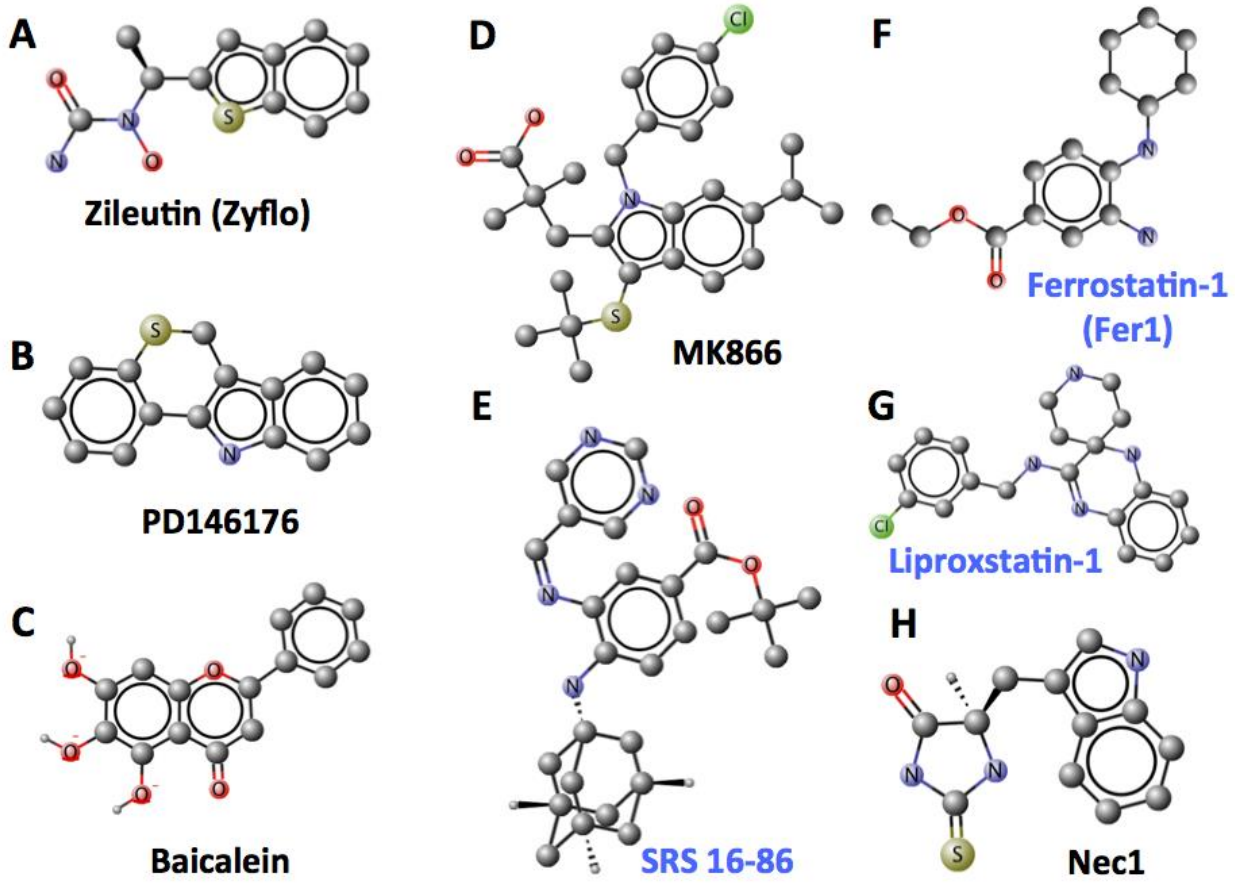

Figure 4-17 The structures of ferroptosis/LOXs inhibitors.

Ferrostatin-1, Liproxstatin-1 and SRS 16-86 are the specific inhibitors of ferroptosis.

Necrostatin-1 (Nec1) (Figure 4-17H) is an inhibitor of RIP1 kinase that blocks the death of TNF-α-treated FADD-deficient cells with an EC_{50} value of 490 nM. It is exclusively known as an inhibitor of necroptosis. Nec1 also plays a role to rescue Gpx4 deficient cells.

Ferrostatin-1 (Fer1) (Figure 4-17F) has been introduced as a ferroptosis inhibitor in 2014, simultaneously when this cell death pathway was discovered [76]. Later, **Lirpoxtatin-1**

(Figure 4-17G) [25] and **SRS 16-86** (Figure 4-17E) [99] were introduced to block the cell death induced by Gpx4 loss. SRS 16-86 is also called third-generation ferrostatin. It is more stable, to metabolism and plasma, and more potent, compared with Fer-1.

4.5.3.2 The binding affinities of ferroptosis/LOXs inhibitors to 15LOX-2

Figure 4-18 demonstrates the binding energies of the tested ferroptosis inhibitors comparing to baicalein —the known inhibitor of 12/15LOX. All the compounds bound at the opening of the catalytic channel. The visual inspection of the biding poses all the tested inhibitors suggested "corking" inhibition mechanism to block the J-shape catalytic site. However, other inhibition mechanism, such as iron chelation may be involved, which cannot be addressed using the rigid and simplified molecular docking.

Interestingly, the last two proposed inhibitors of ferroptosis bound 20 15LOX-2 active site with high affinities —significantly higher than AA. The modeling data and available experimental data again highlighted the potential role of 15LOX-2 in ferroptosis cell death pathway. Since Friedmann et al [25] clearly stated that no individual lipoxygenase can be solely responsible for the cell death processes downstream of GPX4 inactivation, we examined the binding of these compounds to 5 and 12LOX as well (data not shown). All compounds bound to 5 and 12LOX with significantly higher binding energies (lower affinities) compared to 15LOX. Overall, all the substrates and inhibitors binds stronger with 15LOX, possibly indicating the critical role of 15LOX in ferroptosis pathway —in agreement with the available experimental data.

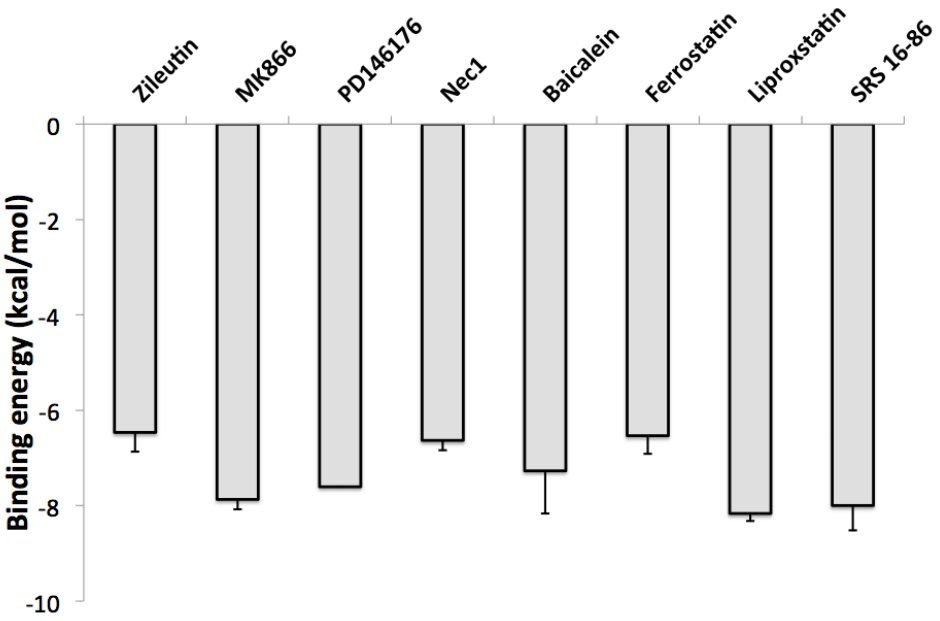

Figure 4-18 The binding affinities of ferroptosis/LOXs inhibitors to human 15LOX-2.

4.5.4 Tocotrienols Are More Effective Inhibitors of Ferroptosis Comparing Tocopherols

Friedmann et al [25] and recent findings in our group confirmed that vitamin E family, tocopherols (Tp's) and tocotrienols (Tt's) are the equipotent inhibitors of the cell death induced by GPX4 inactivation. Khanna et al [100] studied the role of α-Tp on the 12LOX activity and proposed α-Tp may hamper the access of AA to the catalytic site of 12LOX by binding to the opening of the solvent cavity adjacent to the active site. In addition, several studies explained that vitamin Es can inhibit 15LOX (12/15LOX) and 5LOX [101, 102]. Yet, the mechanism of action of this molecule on LOXs remained to be elucidated. Here, we explored the different members of vitamin E family —eight isoforms in total— to study their potential mechanism of action using molecular modeling.

All the vitamin E isoforms have a chromanol ring and a 16-carbon phytyl-like side chain, in which Tp's are saturated and Tt's have three double bonds (Figure 4-19). Different isoforms of Tp's and Tt's vary at the 5- or 7-position of the chromanol ring with either an H or a CH_3 group.

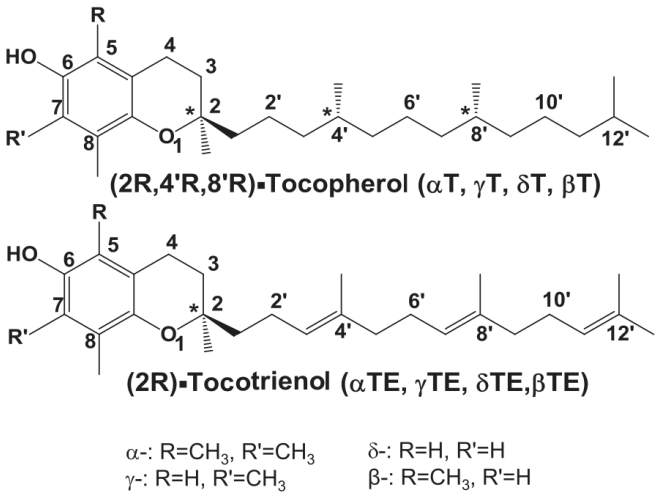

Figure 4-19 Structures of tocopherols (Tp's) and tocotrienols (Tt's).

Molecular docking represented that the binding energies of all Tt's isoforms of vitamin E are lower —defining the higher affinity— comparing to corresponding isoforms of Tp's (Figure 4-20). Yet, the biding energies of α-, β-, γ- and δ-tocopherols are comparable. This trend was observed for Tt's isoforms as well.

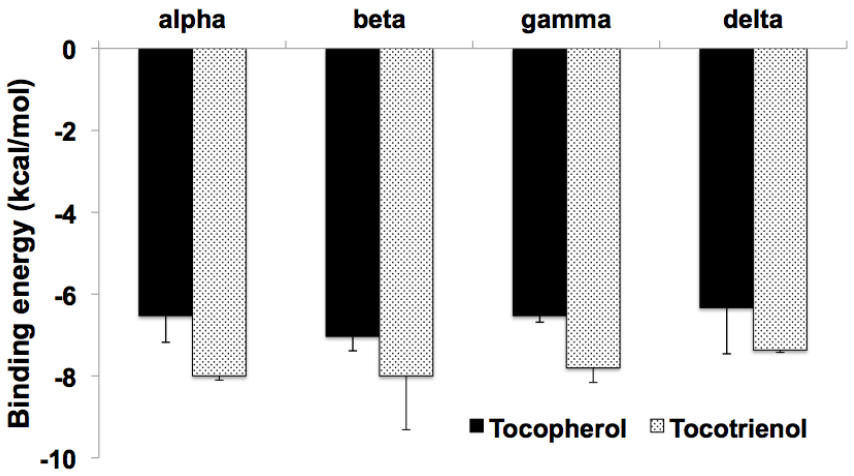

Figure 4-20 Molecular docking represent that the binding energies of all tocotrienol isoforms of vitamin E are lower —defining the higher affinity— comparing to corresponding isoforms of tocopherol (n=3).

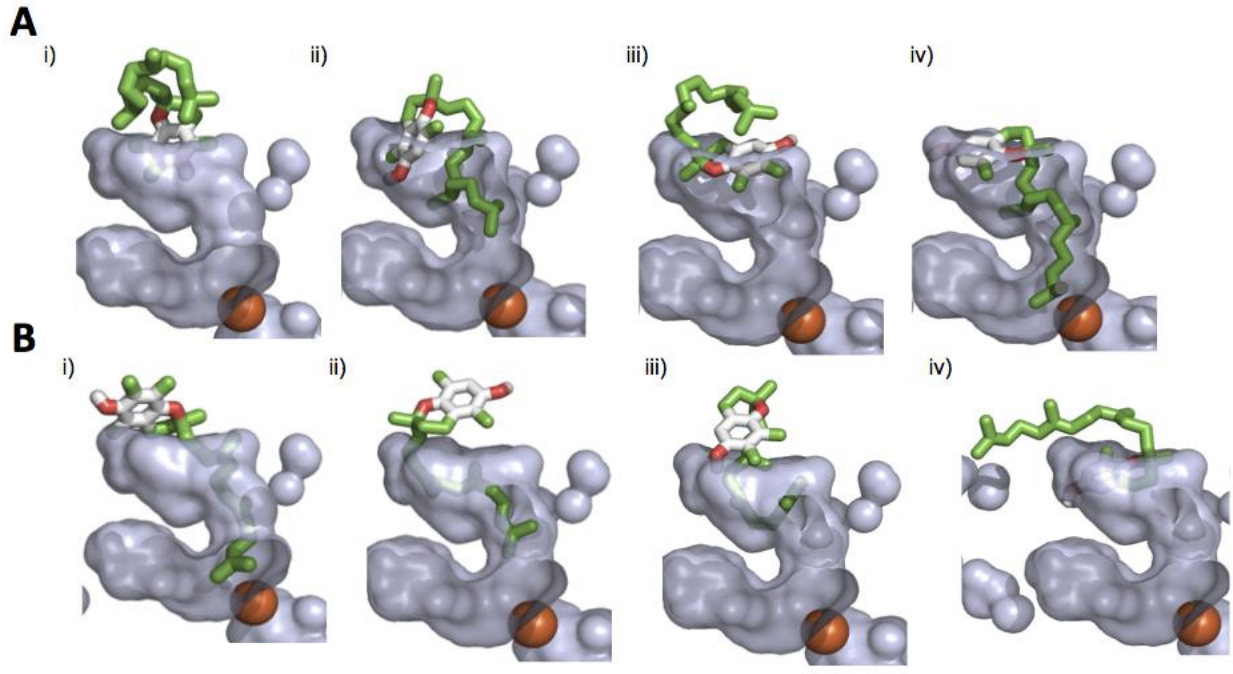

Figure 4-21 Tocopherols and tocotrienols are equipotent inhibitors of 15LOX-2.

(A) Typical binding poses of tocopherol (i) alpha, (ii) beta, (iii) gamma and (iv) delta. (B) Typical binding poses of tocotrienol (i) alpha, (ii) beta, (iii) gamma and (iv) delta.

Moreover, the comparison of Tp's and Tt's binding at the catalytic site clearly represent these molecules —in different ways— blocks the substrate binding site Figure 4-21. Although vitamin E's are known for their radical scavenging properties, the modeling data suggested a corking mechanism. The corking molecule competes with the LOX's substrate to prevent the oxygenation process.

4.5.5 Comparison with Experimental Results

Through modeling it is possible to predict the binding affinities of different FFAs and PLs with the three LOX's under study, including 15LOX, 12LOX and 5LOX. The modeling data showed that FFA and PL have the highest affinity to bind to 15LOX. This finding is in line with published experimental data highlighting the role of 15LOX compared to other LOX's in ferroptosis pathway by knocking down LOX's one by one [81].

Furthermore, my study of the interactions of eight isoforms of vitamin E, including tocopherols and tocotrienols, with LOX's revealed that tocotrienols have higher affinities to interact with LOX's. These data are in concert with the experimental data based on cell viability of GPX4 deficient cells treated with vitamin Es that showed high potency of tocotrienol to inhibit ferroptosis (manuscript is under preparation). It should be noted that LOX's play a key role in lipid peroxidation in this cell death pathway.

Finally, the membrane binding behavior of the 15LOX confirmed the involvement of the N-terminal domain (called PLAT) in the membrane binding, in line with previous studies [29].

4.5.6 Discussion and Conclusion

Ferroptosis is a newly coined term for one of the programmed death pathways that emphasizes the mechanism of cell demise associated with the dysregulation of thiol and lipid oxidative metabolism controlled by GPX4 [81, 82]. Execution of apoptosis includes oxidation of CLs as a required step in apoptosis. In contrast, CL oxidation was not involved in ferroptotic signaling (unpublished results). On the other hand, the redox signaling in ferroptosis is dependent on specific engagement of PE (unpublished experimental data). This also includes different acyl molecular speciation whereby LA(18:2)-containing oxygenated CLs are utilized in apoptosis and oxygenated AA- and AdrA-PE species —in ferroptosis. Moreover, the oxygenating enzymatic mechanisms of apoptosis and ferroptosis are also different viz., cytochrome c [103] and 15LOX, respectively.

It has been shown that the accumulation of PE-OOH is confined to the extra-mitochondrial ER-associated compartments where several iron proteins —COX, LOX and CYP450— can generate PUFA hydroperoxy-intermediates as the primary molecular products of their reactions (according to the available live cell imaging data). Of those, only LOX', utilize di-acyl lipids as their substrates, thus making these non-heme-iron enzymes the prime candidate-catalysts and sources of ferroptotic oxygenated PE-species.

Our goals here, were to understand the mechanism of LOX-driven lipid signaling. Molecular modeling showed the substrate arrangement in the catalytic site of 15LOX can be tail in or head in (with lower probability), which suggests more than one oxygenated products for a particular LOX. It should be noted AA, AdaA and DHA demonstrated similar binding poses and binding energies to 15LOX-2 (~ -7.0 kcal/mol). Yet, the bio-availability and accessibility of the

substrate can also affect the kinetics, an aspect that cannot be addressed using molecular modeling.

We also explored the probability of the oxygenation of PLs via 5, 12 and 15LOX, using computational methods. Our data proposed —five out of six— classes of SA-based PLs can effectively interact with the active site of LOXs. Only SA-PS demonstrated significantly low affinities toward all three LOX's, comparing others. Following the experimental data, we tested two main lipid biomarkers of ferroptosis, SA-PE and SAdrA-PE. Selectivity of LOX towards PE species was not confirmed using modeling data. Indeed, the traditional mechanism of LOX catalyzed oxygenation of free PUFA is based on the selectivity of the respective PLA2 in releasing the substrates of LOX reaction. In case of esterified substrates, the question —how would LOX identify PUFA-PE species, among many other phospholipids with AA- and AdrA-residues for the selective peroxidation? The mechanism based on the formation of specific PE-LOX complexes is not compatible with our computer modeling data indicating that diversified (phospho)lipid classes can effectively interact with LOX. One possible mechanism is a non-bilayer organization of PE in membranes that facilitates availability of these substrates for the enzymatic attack.

To decipher the membrane binding mechanism of 15LOX-2, we ran long CGMD simulations and proved it bound with the similar orientation for the PLAT domain, but quite different for helical active site. These results can be ascribed to the presence of a coil-like structure functioning as hinge and provide flexibility for the active site. This flexibility can change the accessibility of the active site opening to the substrate. This can affect the activation mechanism of LOXs, which needs further evaluations. Additionally, we found that a long loop in the PLAT domain with the highest degree of hydrophobicity is responsible for membrane

binding —in line with previous studies. The discrepancy in the interacting lipids with the PLAT domain suggested lack of lipid specificity for these interactions. The active site, however, in both simulations, was located to SAPI lipids representing a higher probability of using as a substrate by lipoxygenase enzymes.

The inhibition mechanisms of LOXs, particularly 15LOX, were examined using the known inhibitor, bacalein (as a positive control), and tested/specific inhibitors of ferroptosis cell death. In addition of the aforementioned group of the small molecules, vitamin Es —eight isoforms— also were inspected to possibly explain their mechanism of action on LOX —and indirectly on ferroptosis. Interestingly, all the tested compounds in this study bound to the active site of LOXs. The specific ferroptosis inhibitors, including Fer1, liproxstatin and SRS16-86 bound with high affinities to the active site. Among them, SRS16-86 demonstrated the highest affinity, more than one unit higher than baclein and AA —the known inhibitor and substrate of 15LOX.

Moreover, we established that different forms of vitamin Es are universally bound to the LOX catalytic site. Thus one of the physiologically significant mechanisms of vitamin Es action may be stereospecific liganding of the LOX catalytic site outcompeting the oxygenation of free or esterified PUFA hence regulating ferroptosis. Because different vitamin E homologues are effective in inhibiting essentially all LOX isoforms —this suggest, for the first time, the rationale for the previously reported equivocal results on the failure of the approaches based on KO individual LOXs to suppress ferroptosis [81].

Overall, our data revealed the dominant mechanism of peroxidation of esterified fatty acid via LOX's and provided a possible mechanism of inhibition of LOX, particularly by vitamin E's. Moreover, the membrane binding properties of LOXs were also studied.

5.0 CHAPTER 5: COMPUTATIONAL STUDIES OF CARDIOLIPIN SIGNALING IN APOPTOSIS AND MITOPHAGY

5.1 SUMMARY

Due to CL migration during apoptosis the inherent asymmetric distribution of CL is disturbed. It presumably leads to increased CL concentration on the outer leaflet of the inner mitochondrial membrane (IMM) and both leaflets of outer mitochondrial membrane (OMM). CL translocation introduces many challenging biophysical questions regarding to interactions of CL-containing membrane with diversified proteins/enzymes. Here, we sought the mechanism of cardiolipin (CL)-signaling in apoptosis and mitophagy pathways. To this end, we initially appreciated the physical properties and functional roles of cardiolipin in membranes utilizing molecular dynamics simulations. The modeling results were validated using available low-angle X-ray scattering (LAXS) and differential scanning calorimetry (DSC) data.

Coarse-grained molecular dynamics (CGMD) simulations demonstrated that CL thickens the membrane and increases the average lipid area per head group. No significant CL clustering and membrane curvature were observed in symmetrically concentrated-CL-containing membrane. Then, we investigated the molecular details of CL interactions with cytochrome c (cyt-c) and LC3 to decipher the mechanism of CL signaling in apoptosis and autophagy,

respectively. A combination of several molecular modeling methods was employed to identify the CL-binding sites of LC3 and cyt-c. Moreover, the effect of protein interactions on the membrane properties —e.g. lipid clustering and curvature formation— was studied. In apoptosis, we were anxious to explain how CL/cyt-c complex formation leads to lipid peroxidation. The presence of two binding sites on distal and proximal sides of heme paved the path toward the understanding of the heme crevice opening for the substrate.

5.2 SIGNIFICANCE

Among the various types of lipids that form mitochondrial membranes, CL is a mitochondria-specific phospholipid (PL) with two phosphatidyl groups linked to a glycerol backbone and four fatty acyl chains. The synthesis of CL is on the matrix side of IMM [104], which introduces a CL asymmetry. The CL asymmetry allows to membrane potential for the "healthy" mitochondrion to be maintained [27]. CL asymmetry is disrupted through a process called "CL externalization" [21]. Upon mitochondrial injury and depolarization, a significant portion of CL becomes exposed on the mitochondrial surface, where it serves as either the pro-apoptotic or pro-mitophagic signal, depending on the extent of mitochondrial injury [105]. The presence of a myriad of proteins associated with either the IMM or the OMM allows critical biophysical questions regarding the interactions of CL-containing membrane and proteins to be addressed. While many studies of molecular interactions of CL with proteins have been done, the common features of the CL-binding sites are enigmatic. Therefore, using computational approaches we examined (i) the structural role of CL in the membrane, (ii) the mechanism of interactions of the externalized

CL with cyt-c and LC3, and (iii) the consequence of protein interactions for the membrane properties.

5.3 INTRODUCTION

CL (1,3-bis(sn-3′-phosphatidyl)-sn-glycerol) is essential for the structural organization and function of mitochondrial membranes by supporting membrane dynamics and stabilizing the lateral organization of protein-rich membranes [106]. CL is an unusual anionic phospholipid with two negatively charged phosphate groups in its polar head and a bulky hydrophobic "body" containing 4-acyl chains [107, 108]. The specific features of CL result in a small head group, which in turn promotes negative curvature, cohesive effects between hydrocarbon chains, and electrostatic interactions [14]. Figure 5-1 represent three different CL species from the diversified class of CLs. TLCL is an oxidizable CL species due to presence of two unsaturated bonds in each acyl chain.

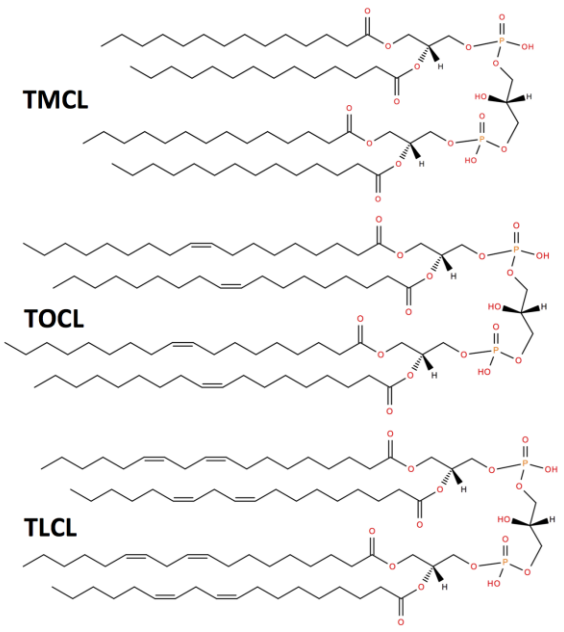

Figure 5-1 Cardiolipin is a diversified class of lipids. Tetramyristoyl-CL (TMCL), tetraoleyl-CL (TOCL) and tetralinoyl-CL (TLCL) are the CL species have been sued in this study. The latter is an oxidizable CL species.

Cardiolipin (CL) displays extraordinary specificity in its cellular distribution. It is found almost exclusively in the IMM of eukaryotes, where it constitutes about 20 % of total phospholipids (PLs). A stronger enrichment is found in the matrix-facing leaflet of IMM, which contains 70-80 % CL. This has been determined using CL-specific antibodies on mitoplasts [109, 110]. The appearance of CL in the OMM is to be interpreted as an "eat me" signal to induce mitophagy — the selective degradation of mitochondria by autophagy. CL externalization serves as a signal recognized by LC3, —an autophagosome-associated enzyme responsible for cargo recognition— and leads to the engagement of the autophagy machinery [28]. How the obstacles of transmigration from the inner leaflet of the IMM to the outer leaflet of the OMM are overcome has been the focus of many recent studies and several candidate enzymes have been suggested to be involved [26]. While mitophagy was achieved through presence of CL in its native structure on mitochondrial surface, modified CL species may play even more diverse roles in terms of cell signaling. Owing to its high unsaturation level and versatile molecular structure, lipid peroxidation initiated by reactive oxygen species (ROS) generates a wide range of oxygenated species. A physiological catalyst found responsible for CL peroxidation is cyt-c, which is linked to the intrinsic apoptosis cell death pathway [111]. In mitochondrial apoptosis, interactions of CL with cyt-c result in formation of peroxidase complexes, leading to the accumulation of oxidized CL (oxCL) products. This leads to the release of pro-apoptotic factors, including cyt-c, from mitochondria into the cytosol (Figure 5-2).

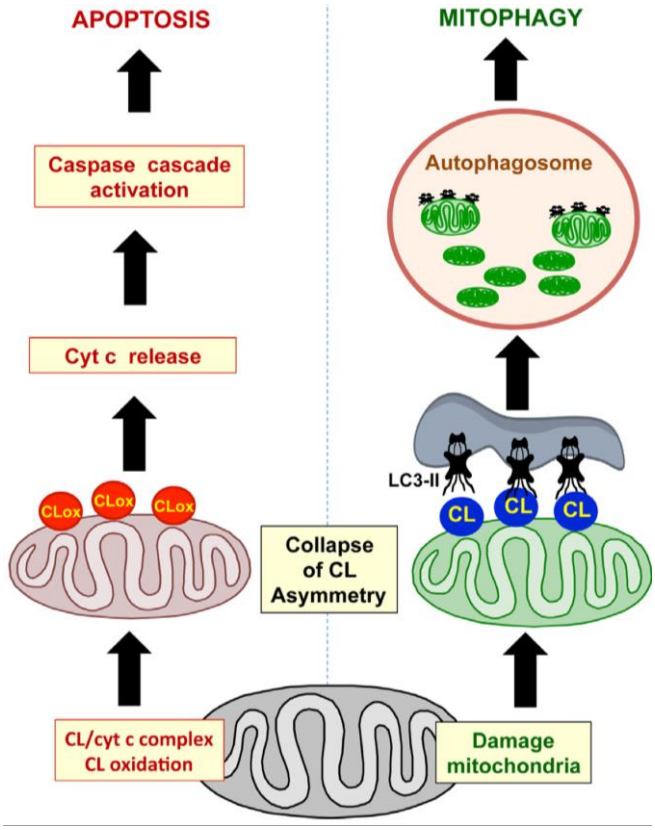

Figure 5-2: The illustration of CL-driven intracellular signaling pathways in mitophagy and apoptosis.

Either in mitophagy or apoptosis the molecular details of the interactions of CL and target proteins are not fully understood. On the other hand the effect of these interactions on the membrane also needs to be elucidated. In this chapter we utilize a combination of several computational approaches to study the interactions of CL and cyt-c and LC3, involved in apoptosis and mitophagy, respectively.

5.4 APPROACH

5.4.1 Effects of CL on the Structure and Properties of Lipid Membranes

To shed light on the molecular details of lipid signaling through maintaining/disrupting CL asymmetry, one should initially appreciate the effects of CL on the structure and properties of lipid membranes.

The CGMD simulations of lipid bilayer systems were carried out with the MARTINI force field. Two CL species were used, including tertramyristoyl-cardiolipin (TMCL) and tertraoleoyl-cardiolipin (TOCL). Six different lipid bilayer systems, including pure DMPC, pure DOPC, DMPC containing 20% TMCL, DOPC containing 5, 7.5, 10 and 20% TOCL were studied. Na^+ ion was added to each simulation box to neutralize the total charges. Initially, each system was minimized, and a 20 ns NVT (constant number of particles, volume and temperature) ensemble equilibration was followed by a 20 ns NPT (constant number of particles, pressure and temperature) ensemble equilibration. Each MD run was carried out to cover 500ns. A 40fs time step was used to integrate the equations of motion. For all simulations, analyses were performed using the last frame in the 500 ns trajectory for the snapshots. Number densities were determined using the undulation correction method with filter cutoff $q_0 = 1.0\ nm^{-1}$ [112, 113]. Areas were calculated by dividing the size of the simulation box (XY) by half the number of lipids. Finally, the membrane properties calculated via simulations compared with available experimental data obtained from differential scanning calorimetry and S_{Xray}.

5.4.2 Study Interactions of CL and Cyt-c

Molecular Docking: The structure of the TOCL was docked to the crystal structure of native cyt-c (pdbid: 1HRC) [114]. Three docking modeling sessions were run using three different random number generator seeds. A cubic box was positioned at x, y, and z values of 46.839, 23.029, and 5.505, respectively. The center was built around the protein with 52 × 52 × 52 points and a spacing of 0.375 Å between the grid points. The top 9 resulting orientations were clustered together based upon the RMSD value with respect to model 1. The best ligand bound receptor structure in each case was chosen based on lowest energy, visual inspection (to recognize similarities of the models), as well as the total number of conformations in a cluster.

Orientations of Proteins in Membranes (OPM): Protein orientation on the membrane was predicted using OPM server applying default settings [115]. OPM offers spatial arrangements of proteins with respect to the hydrophobic core of the lipid bilayer. The rotational and translational positions of peripheral and trans-membrane proteins in membranes can be calculated using this online server. OPM only requires the 3D structure of the interested protein (PDB coordinate file) as input.

The CGMD simulations: 400 lipids, including 1,2-dioleoyl-sn-glycero-3-phosphocholine (DOPC) and TOCL, were used to construct the membrane. Five membranes with varying TOCL amount of 0 (control), 5, 7.5, 10, and 20 mol% TOCL were chosen and subjected to simulation. The composition of the lipids in each membrane listed in Table 5-1.

The CG model of DOPC and TOCL molecules is illustrated in Figure 5-3. Each system equilibrated with three different random seeds to produce different initial velocities and thus different trajectories. In total, 15 simulations were run, 1 microseconds each. Initially, each system was minimized for 20 ps, before 1 ns NVT and 1 ns NPT ensemble equilibration. The

position of protein was restricted during equilibration runs. A 15 fs time step was used to integrate the equations of motion.

Table 5-1 The composition of the membrane used for CGMD simulations of CL/cyt-c interactions.

CL concentration in the membrane (mol%)	Number of DOPC	Number of TOCL
0 (Control system)	400	0
5	380	20
7.5	370	30
10	360	40
20	320	80

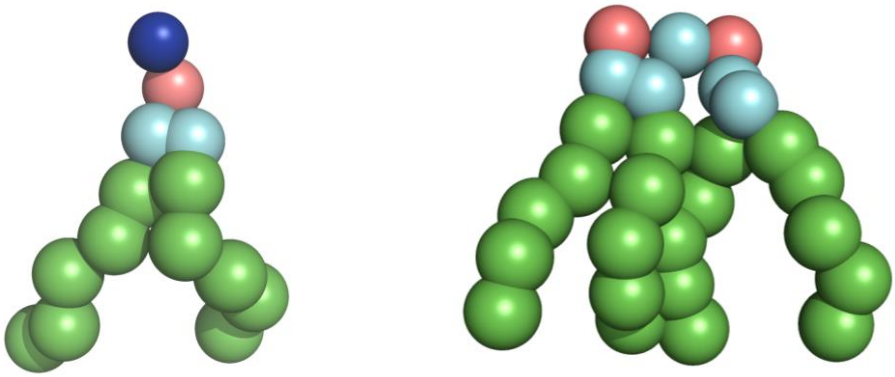

Figure 5-3 CG model of DOPC (left) and TOCL (right) molecules based on the MARTINI force field.

5.5 RESULTS AND DISCUSSIONS

5.5.1 Physical properties and functional roles of cardiolipin in membranes

CL-containing membranes, in general, are vulnerable to forming negative curvature and thickening, and depending on the CL species, it may rigidify or liquefy the membrane. CGMD simulations based on MARTINI force field, in line with differential scanning calorimetry (DSC) and S_{Xray}, suggest that TMCL does not form domains within the DMPC bilayers (Figure 5-4 A) [116].

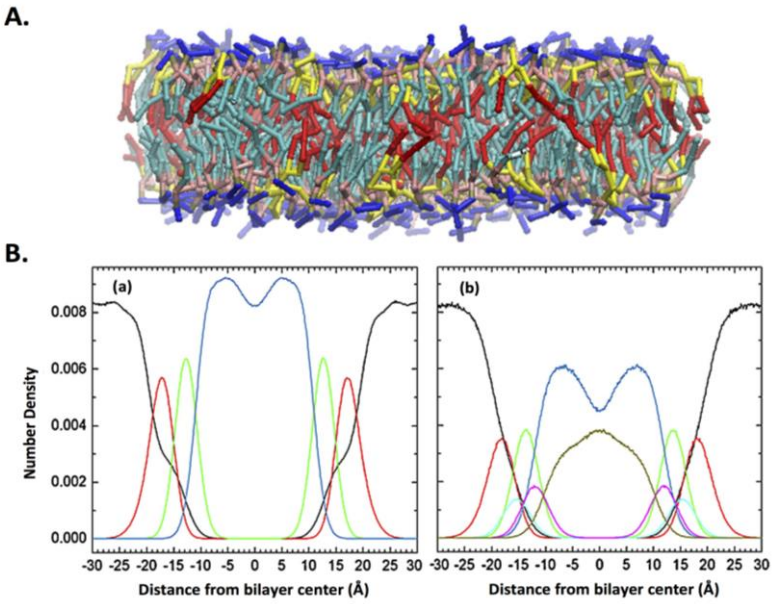

Figure 5-4 TMCL induces thickening and increasing the area per lipid head group in mixture with DMPC.

A. interactions of TMCLs and DMPCs in bilayer thicken and stiffen the membrane, B. Number densities calculated from the CGMD Martini simulation of (a) DMPC and (b) DMPC/20mol% TMCL. Color code: water (black), DMPC phosphocholine (red), DMPC glycerol-carbonyl (green), TMCL phosphoglycerol (cyan), TMCL glycerol-carbonyl (magenta), DMPC chains (blue) and TMCL chains (dark yellow).

The number densities calculated from CGMD simulation, in concert with experimental results, demonstrated that the presence of 20 mol% tetramyristoyl-CL (TMCL) induces a thickening of 2 Å and an increase in the area per lipid head group of 8 $Å^2$ in a mixture with 1,2-dimyristoyl-sn-glycero-3-phosphocholine (DMPC) (Figure 5-4 B). Interestingly, the data revealed that the TMCL headgroups localize near the glycerol-carbonyl region of DMPC; i.e., they are sequestered below the DMPC phosphocholine headgroup (Figure 5-4 B).

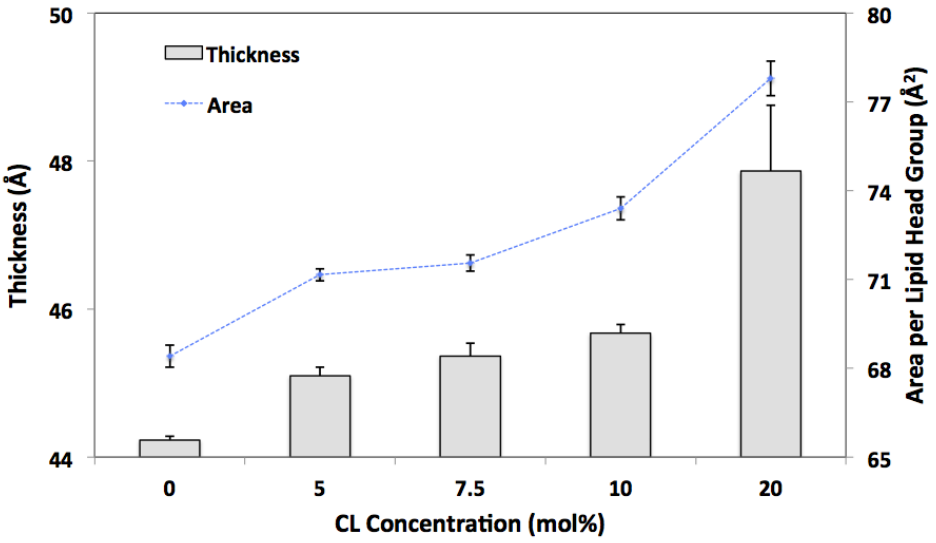

Figure 5-5 TOCL thickens the membrane and increases the average lipid area per head group in presence of DOPC as a matrix lipid in the bilayer.

We have re-evaluated our finding using another species of CL, 1,1′,2,2′-tetraoleoyl-cardiolipin (TOCL), in the membrane with a different concentration of TOCL. In sum, regardless of lipid species, the presence of CL in the bilayer thickens the membrane and increases the average lipid area per head group in the presence of DOPC as a matrix lipid in the bilayer (Figure 5-5). Additionally, no significant CL clustering (domain formation) or membrane curvature was observed.

5.5.2 Computational Studies of CL-signaling in apoptosis

Cyt-c is an inter-membrane space (IMS) mitochondrial protein, which carries electrons from the inner mitochondrial membrane (IMM) proteins respiratory complex III (cytochrome c reductase) to complex IV (cytochrome c oxidase) [111, 117, 118]. Cyt-c is a highly conserved, alpha helical globular protein, composed of 104 amino acids [119]. The prosthetic heme group of cyt-c is covalently linked to the peptide chain at positions Cys14 and Cys17 [120] (Figure 5-6 A). The heme iron is in hexa-coordinated form, with four covalent bonds from the porphyrin's nitrogen atoms and two axial ligands, His18 and Met80 [114, 121]. Upon binding to Complex III, Met80 moves away from the covalently bonded iron to facilitate reduction [117, 122]. Cyt-c is a positively charged enzyme with a net positive charge of +9.2-9.6 (Figure 5-6 B), and has an affinity toward anionic lipids.

In addition to the well-established bio-energetic function, cyt-c has been identified as an essential pro-apoptotic factor acting as a switch in mitochondria-mediated cell death pathways upon its release into the cytosol [107, 111, 117, 122-125]. Recent studies revealed that the liberation of cyt-c is mediated by its binding to a mitochondria-specific phospholipid, CL. The presence of CL is important for the proper structural arrangements and functioning of a number of proteins [126, 127]. Among those are the cyt-c-related respiratory complexes III, IV, and V which require two, two, and four CL molecules, correspondingly, as binding partners to maintain their functions [128-130].

Under physiological conditions, only a minor fraction of CL interacts with cyt-c resulting in the attachment of ~10-15% of cyt-c to the IMM [125, 131, 132]. However, during apoptosis, trans-membrane migration of CL from the IMM to the OMM facilitates the formation of cyt-c/CL complexes, which initiated a new peroxidase enzymatic activity [121, 126, 133]. While

soluble cyt-c displays only very weak peroxidase activity, it increases over 50-fold in the complex, as measured in the presence of H_2O_2 [125].

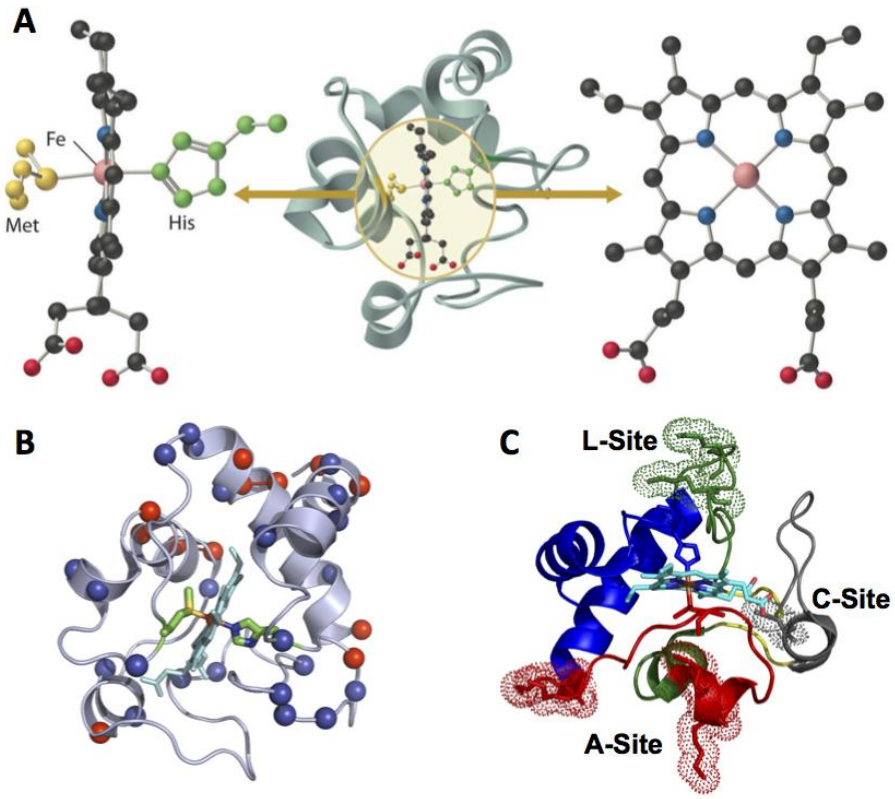

Figure 5-6 Cyt-c structure is a Heme containing protein localized in IMS.

A. Heme contains Fe^{2+} in the center, and ligated with four bonds in porphyrin ring and His18 (on proximal side) and Met80 (on distal side) (from http://chemwiki.ucdavis.edu). **B.** Cyt-c is a positively charged protein with a net charge ~+10 in physiological condition. Blue and red spheres represent α-carbons of the positive and negative residues, respectively. **C.** Previously introduced CL binding sites of cyt-c.

The gain of enzymatic activity is even up to 1,000-fold with fatty acid hydroperoxides as sources of oxidizing equivalents [125, 126]. The newly emerged peroxidase activity is highly selective towards polyunsaturated species of bound CL yielding a variety of oxygenated CL species (oxCL) [103]. Accumulation of oxCL leads to a permeabilization of the OMM – through yet to

be established mechanisms – thus facilitating the release of cyt-c into the cytosol [103, 121]. These mitochondrial events designate the point of no return in apoptosis [103, 134] initiated by the binding of cyt-c to the WD-40 portion of apaf-1 in apoptosomes [103].

The gain of peroxidase activity requires a non-native conformation of cyt-c. Circular dichroism [135, 136] and electron paramagentic resonance [118, 131] spectroscopic studies suggest that binding of CL induces a conformational changes in the tertiary structure and partial unfolding of cyt-c, resulting in the reduction of its α-helical content [137-139]. Furthermore, changes in heme iron coordination state and redox potential have been documented [140-142]. The location of the binding sites for CL on cyt-c is controversial and three binding sites, referred to as A, C and L (Figure 5-6 C) have been proposed. An unusual number of positively charged residues are found in these sites and are believed to be involved in electrostatic attraction of CL phosphates. In particular, Lys72 and Lys73 [131, 132, 143] and Lys86 and Lys87 [144] in site A have been implicated in initiating complex formation, while high affinity binding may require additional interactions with Site C, especially Asn52 [132, 136]. At a lower pH, Lys22, Lys25, and Lys27 in site L have been proposed to become available for interaction [145]. Because sites A and L are not contiguous on the surface of cyt-c, it was proposed that binding of liposomes to these sites may mediate membrane fusion [132].

Other models suggest that electrostatic interaction of cyt-c with anionic phospholipid membranes results in partial insertion of cyt-c into the bilayer membrane [146-148]. Finally, there are also extended lipid anchorage models, in which one or two of the CL's acyl chains protrudes out of the membrane and inserts into a hydrophobic cavity of the protein [136, 143, 149]. The models differ in location and nature of the hydrophobic pocket [136, 143, 149]. All models involve the Met80 loop, but either also involves residues 67-71 [149, 150], or 81-85, or

Asn52 [143]. A recent model proposes two - rather than one – of the CL acyl chains to be inserted into cyt-c [136].

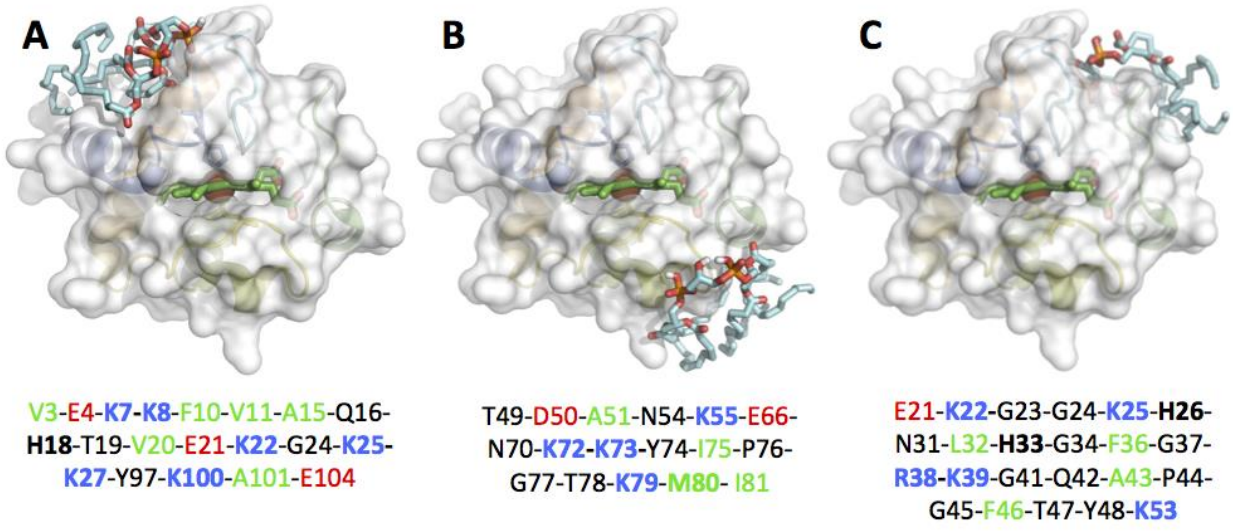

Figure 5-7 Molecular docking predicts three CL-binding sites, which can be generalized in two main sites called "distal" and proximal" sites.

Molecular docking predicted three CL-binding sites: **A.** site one is located in vicinity of proximal His18, **B.** site two is placed in neighboring of distal Met80, and **C.** Site three represents some overlaps with site one and remaining of this site is extended toward the opposite side of HEME crevice opening.

The diversity and often mutually exclusive character of existing models highlights the incompleteness of our knowledge and the complexity of the interactions between cyt-c and CL. Furthermore, experimental observations such as the need for a threshold concentration of CL required to induce peroxidase activity cannot be explained by any of these models. Therefore, we employed a combination of several computational approaches —validated by solution NMR data generated in our laboratory— to elucidate the molecular details of CL/cyt-c interactions. Molecular modeling methods, including Gaussian network modeling (GNM), molecular docking,

prediction of orientation of cyt-c with respect to the membrane and coarse-grained molecular dynamics (CG-MD) simulations were used to complement the NMR studies.

5.5.2.1 Predicting CL Binding Sites on cyt-c by docking

Autodock Vina was used to predict putative binding sites by molecular docking studies using the structure of native horse heart cyt-c (PDB ID: 1HRC) and TOCL. We grouped the nine top-ranked CL binding poses into three possible CL binding sites based on binding affinities, probability of occurrence and visual inspection of the models (to classify the models based on their similarities).

Table 5-2 Residues interacting with CLs in each model, predicted by molecular docking.

Probability of Binding Pocket	Residues interacting with CL (in 5Å distance to CL)	Binding Energy (kcal/mol)
4/9	Model1: V3-E4-**K7**-**K8**-F10-V11-A15-Q16-**H18**-T19-V20-E21-**K22**-G24-**K25**-**K27**-Y97-**K100**-A101-E104	-3.3
	Model2: V3-E4-**K5**-**K7**-**K8**-F10-V11-V20-E21-**K22**-**H33**-Y97-**K100**-A101-E104	-3.2
	Model7: E4-**K7**-**K8**-F10-V11-Q12-A15-Q16-**H18**-T19-V20-E21-**K25**-**K27**-Y97-**K100**-A101-E104	-3.0
	Model8: V3-E4-**K7**-**K8**-F10-V11-Q12-**K13**-A15-Q16-C17-**H18**-T19-V20-E21-**K27**-T28-Y97-**K100**	-3.0
2/9	Model3: T49-D50-A51-N54-**K55**-E66-N70-**K72**-**K73**-Y74-I75-P76-G77-T78-**K79**-**M80**- I81	-3.1
	Model6: T49-D50-A51-N54-**K55**-I57-N70-**K72**-**K73**-Y74-I75-P76-G77-T78-**K79**-**M80**-I81	-3.1
3/9	Model4: N31-**H33**-G34-L35-F36-G37-**R38**-**K39**-Q42-A43-P44-T58-W59-**K60**-**K99**-T102-N103-E104	-3.1
	Model5: E21-**K22**-G23-G24-**K25**-H26-N31-L32-**H33**-G34-F36-G37-**R38**-**K39**-G41-Q42-A43-P44-G45-F46-T47-Y48-**K53**	-3.1
	Model9: E21-**K22**-G23-G24-**H26**-N31-**H33**-G34-L35-F36-G37-**R38**-P44-G45-T58-W59-**K60**-E61-E62-**K99**-T102-N103-E104	-3.0

Representatives of each binding site are shown in Figure 5-7 A-C and the residues within 5Å of TOCL are listed under each model shown and for all nine models in Table 5-2.

The first binding site (Figure 5-7 A), which we will refer to henceforth as the "proximal site" includes site L and several other residues in vicinity of proximal heme ligand His18. It consists of 6 positively charged Lys, 6 hydrophobic amino acids, 3 negatively charged Glu. His18 is also positively charged [151]. The acyl chains of TOCL are aligned toward the N- and C-terminal helices H1 and H5, respectively. The Glu residues may facilitate interactions of cyt-c with positively charged groups of zwitterionic lipids, such as the choline group of phosphatidylcholine, an abundant lipid in any biological membrane. Thus, the nature of the amino acids and secondary structures present in the proximal site supports involvement of electrostatic (specifically with CL, but potentially also other lipids in which CL is embedded) and hydrophobic forces in the cyt-c/CL interactions. A close proximity of Lys25 and Lys27 nitrogen atoms to oxygens in the CL phosphate groups may result in stabilization of the interaction through hydrogen bond formation. A recent survey of amino acids present in known CL binding pockets [152] identified the motif G as characteristic of CL binding. This motif is also present in the CL proximal site.

The second CL binding site (Figure 5-7 B), henceforth referred to as the "distal site" includes site A and several residues in close proximity of the distal heme ligand, Met80. The composition of this site is overall similar to that of the proximal site and also comprises four positively charged Lys, 4 hydrophobic and 2 negatively charged amino acids (Asp50 and Glu66). In this site, the CL acyl chains are extended around helices H2 and H4.

The third predicted binding site (Figure 5-7 C) is only composed of random coil. This site consists of 5 positively charged (R38 and 4 Lys), 1 negatively charged, and 4 hydrophobic

residues. This site is also located on the proximal side of the heme but does not include the critical heme-coordinating residue His18. The third binding site does not show overlap with previously identified binding sites, but is in proximity to the previously proposed site C (Asn52). As for the proximal site, the motif G (K,L) is present. Furthermore, its high abundance of Gly and positively charged residues and low abundance of Leu, Val, Ile are all characteristic of CL binding [152]. Finally, this binding site contains Y48, which was recently identified as a CL binding residue [153].

5.5.2.2 Predicted contacts of cyt-c with membrane surfaces

Clearly, the interaction of cyt-c with a single CL molecule as used in docking studies is an oversimplification as CL is embedded in a membrane *in vivo*. We therefore investigated the predicted orientation of cyt-c with respect to membranes using the OPM server [154, 155].

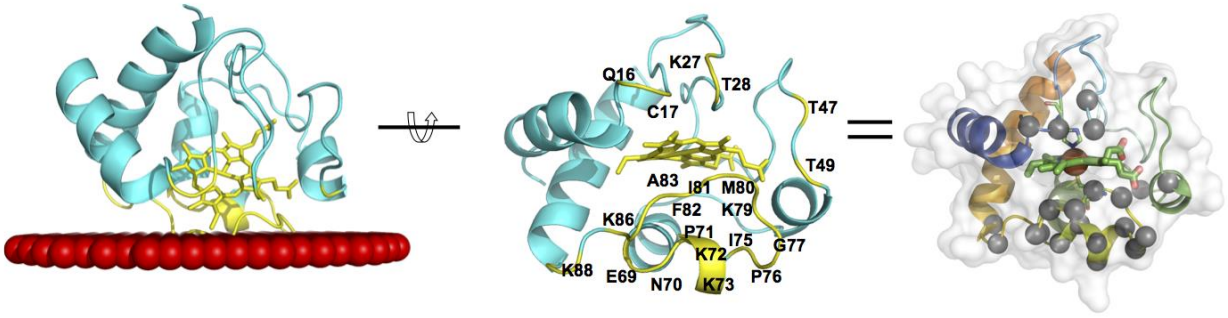

Figure 5-8 The orientation of cyt-c with respect to the membrane predicted using OPM server.

This orientation is highly in concert with the proposed proximal and distal binding sites.

The orientation of cyt-c with respect to the membrane according to OPM is shown in Figure 5-8. This orientation highly correlates with the proposed proximal and distal binding sites. The residues Lys22, Lys25, Lys27, His33, Arg38, Lys72 and Lys73 are all calculated to be part of

the OPM membrane-binding interface on cyt-c. Moreover, several hydrophobic residues around and including M80 are predicted to be part of the interface. This suggests the proximal and distal sites may be viewed as a joint albeit not contiguous binding site.

5.5.2.3 Coarse-grained molecular dynamics simulation of cyt-c interaction with membranes

Ideally, we would like to study the interaction of cyt-c with CL further in the context of the lipid environment provided by the membrane. However, considering the large system size and long simulation time required to study the interactions of proteins with membranes, we chose CGMD simulations, rather than full atomistic MD simulations. CG-MD simulations offer advantages due to the greater length and time scales possible to capture possible interactions and to study the consequences of the interactions on both protein and lipid bilayer.

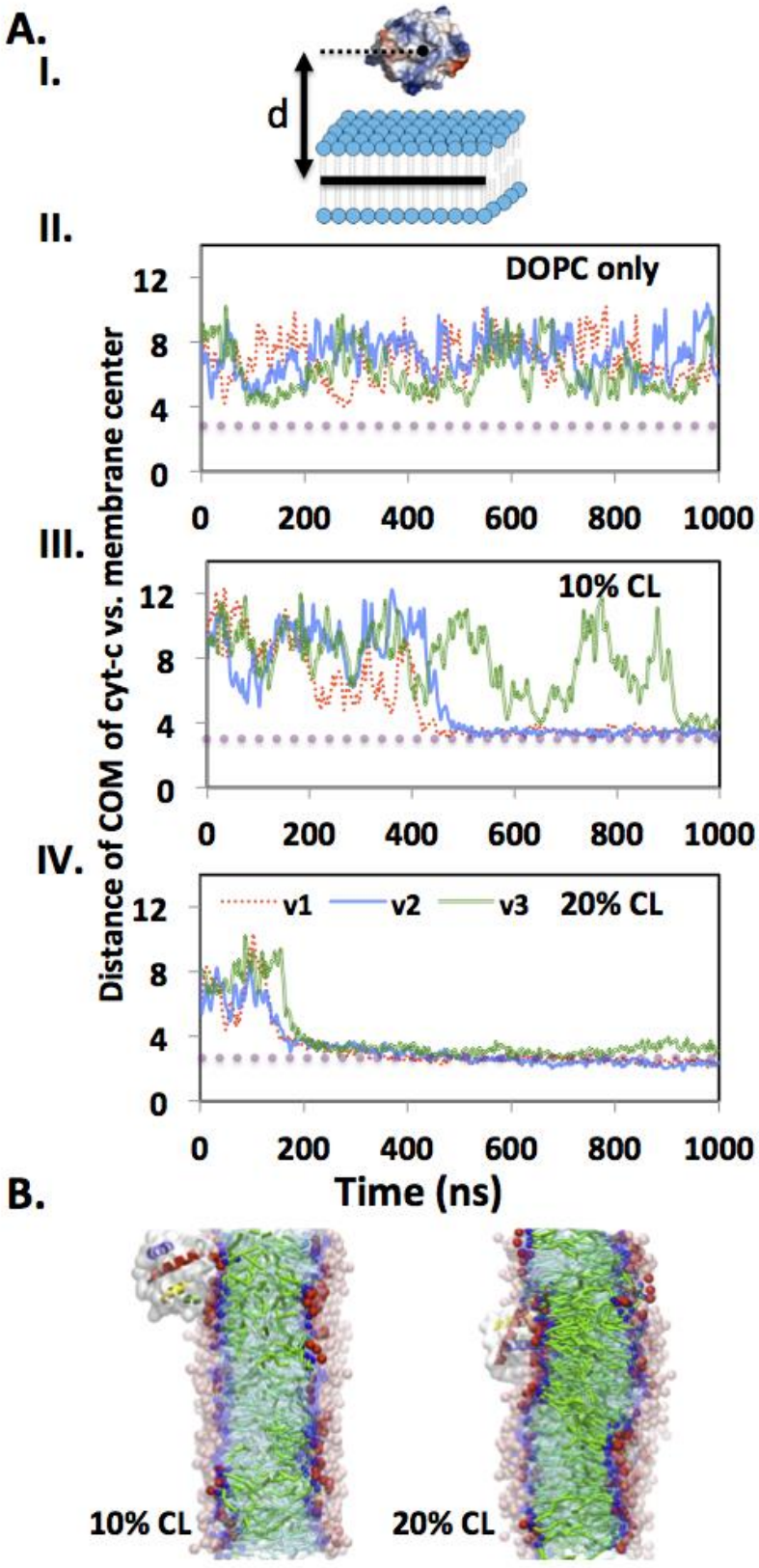

Figure 5-9 Cyt-c interacts with higher affinity to the membrane containing a larger amount of CL.

A. I. Schematic representation of the distance between COM of cyt-c and center-line of the membrane; II-IV. The distance of cyt-c to the membranes containing pure DOPC, DOPC-10 mol% CL and DOPC-20 mol% CL over 1 μs of three independent CG-MD simulations, respectively. Dotted line represents the membrane surface. **B.** The comparison of the typical final configuration of the interactions of cyt-c with the membranes containing 10 and 20 mol% CL. Representation guide: transparent cyan: DOPC acyl chains; green: CL acyl chains; transparent pink: choline and phosphate groups of DOPC; red: head groups of CL (two phosphate groups and one connected glycerol backbone); transparent blue: glycecrol backbone of DOPC; blue: glycerol backbone of CL; Helices: Blue: residues 3-13, Green: resides 50-54, Yellow: resides 61-67, Orange: resides 71-74 and Red: residues 88-103.

Three independent CG-MD simulations of the interactions of cyt-c with membranes of different compositions varying in the amount of CL (0, 5, 7.5, 10 and 20 mol% embedded in DOPC) were run for 2μs each. The schematic representation in Figure 5-9 A.I. illustrated how distances of the center of mass (COM) of cyt-c with respect to the center of the membrane were calculated. In the absence of CL, cyt-c did not interact with the membrane (Figure 5-9 A.II.), while addition of 10% CL resulted in 2 out of 3 simulations in a bound state (Figure 5-9 A.III and IV). The membrane containing DOPC-20 mol% TOCL always resulted in a bound state (Figure 5-9 A.VI. and B.II.).

The analysis of cyt-c residues located in 5Å distance of any CL molecules at the final configuration of each simulation, confirmed the simultaneous presence of the distal (residues 72-88) and proximal (residues 5-18 and 22-27) CL binding sites on cyt-c in two of the simulations and the third binding site (without the other two) in one of the simulations (Table 5-3).

In one of the three CGMD simulations, the third binding site from docking was observed. When relaxing the elastic network constraints on the protein and thus allowing greater flexibility in the protein structure, a 300 ns further simulation resulted in a reorientation of cyt-c into the orientation found in the other two simulations, where proximal and distal binding sites are occupied together.

Table 5-3 Residues interacting with CLs at t=1 μs for each individual CG-MD simulation.

Simulation ID		Cyt c Residues Interacting with CLs at t=1 μs
CL Concentration (mol%)	CGMD-ID	
5	1	--
	2	--
	3	**K55**-N70-P71-**K72**-**K79**-M80-**K86**-**K87**-**K88**-**R91**
7.5	1	A51-N54-**K55**-**K73**-Y74-P76
	2	**K22**-G24-**K25**-**H26**-**K27**-**H33**-L35-Q42-P44-G45-F46-T47-**K53**
	3	--
10	1	**K22**-**K25**-**H33**-G34-**R38**-**K39**-P44-**K53**-N54
	2	G23-**H26**-**H33**-L35-**R38**-**K39**-Q42-P44-G45-**K53**-**K100**-N103
	3	**K55**-N70-**K72**-**K73**-Y74-I75-G77
20	1	**K5**-**K8**-I9-Q12-**K13**-C14-Q16-C17-T19-**K24**-**K25**-**K27**-T28-G29-F46-Y48-A51-**K55**-E69-**K72**-**K73**-Y74-I75-P76-**K79**-G84-**K86**-**K87**
	2	**K5**-**K8**-I9-Q12-**K13**-Q16-C17-**K25**-**H26**-**K27**-F46-Y48-T49-**K72**- P76-G77-**K79**-**M80**-A83-**K86**-**K87**-**K88**-T89
	3	**K25**-**H26**-**H33**-**R38**-**K39**-G41-Q42-A43-P44-G45-F46-T47-**K53**-N54

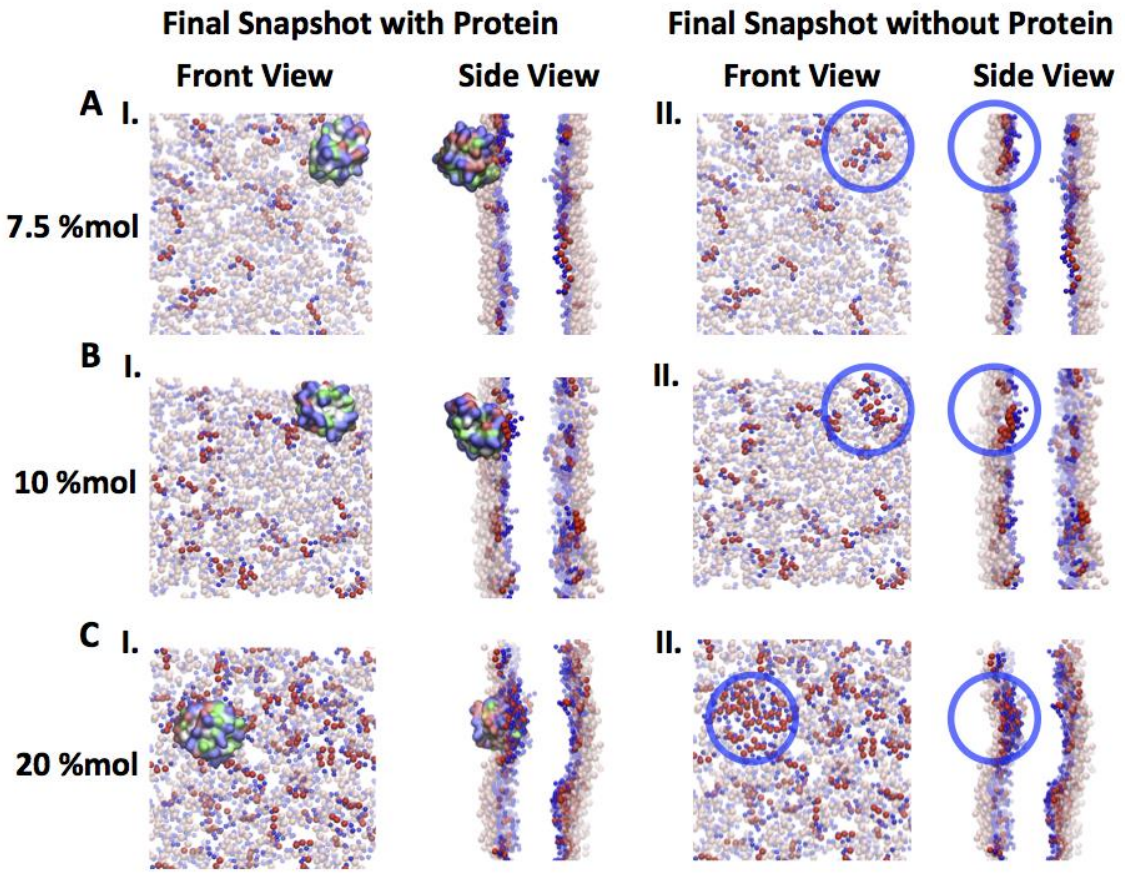

Figure 5-10 Interactions of Cyt-c induce CL clustering on the membrane, which leads in a negative curvature on the membrane surface.

Final configurations of the head groups of the lipids in the membrane containing **A.** 7.5, **B.** 10 mol% and **C.** 20 mol% CL interacting with cyt-c, I. top and side views with cyt-c presentation, II. top and side views without cyt-c presentation – to represent CL-clustering underneath of the protein. Representation guide: transparent pink: choline and phosphate groups of DOPC; red: head groups of CL (two phosphate groups and one connected glycerol backbone); transparent blue: glycecrol backbone of DOPC; blue: glycerol backbone of CL; colorful particle: Cyt c.

Effect of cyt-c interactions on CL-containing membranes –The CG-MD simulations not only shed light on the details of the amino acids on cyt-c involved in the interaction with the membrane, but also show how cyt-c affects the membrane. In particular, we observed very

clearly that the strong interactions of cyt-c with CL-containing membranes lead to CL clustering (Figure 5-9 B, and Figure 5-10), in line with previous studies [156, 157]. This clustering in turn induces a negative curvature on the membrane surface, especially visible at the highest concentration of CL used (Figure 5-10 C.II.).

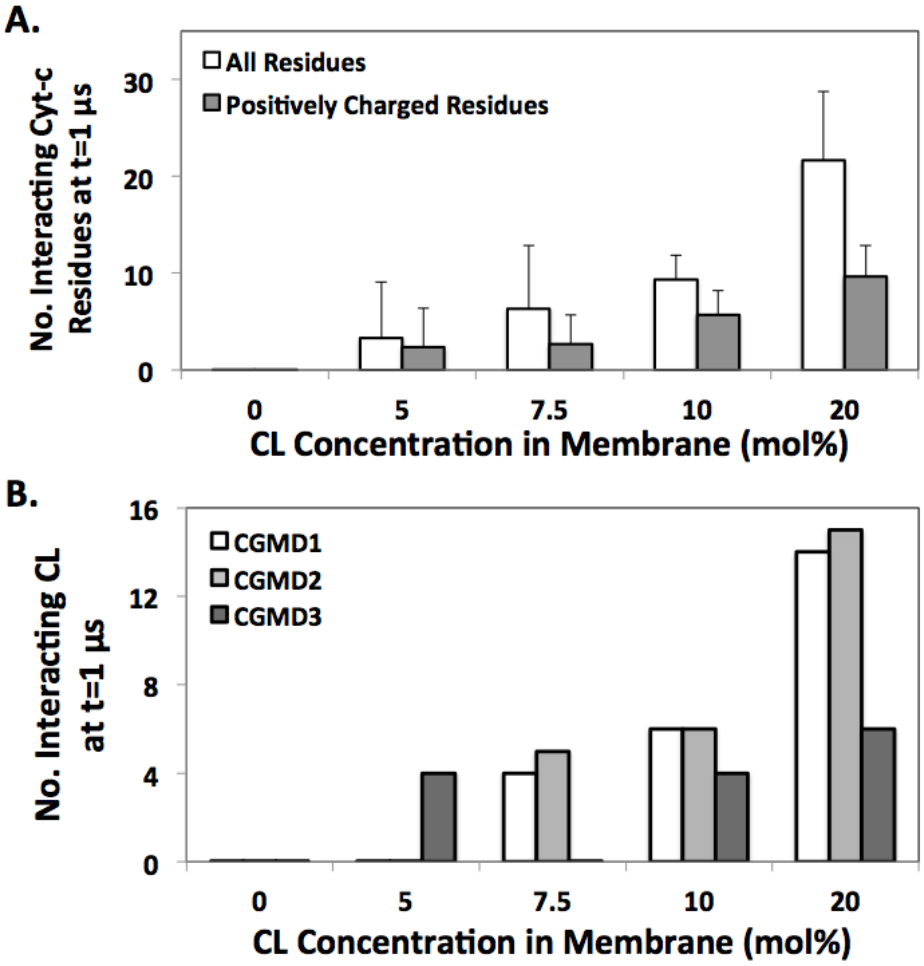

Figure 5-11 Number of cyt-c residue interacting with membrane and number of CL interacting with cyt-c enhance by increasing CL concentration in the membrane, indicating higher affinity of cyt-c to interact with CL-rich membranes.

A. Average number of cyt-c resides, including all and positively charged residues, interacting with CL-containing membranes at t = 1 µs (n=3). **B.** Average number of CL interacting with cyt-c at t = 1 µs (n=3).

It is well known experimentally that not only in the eukaryotic mitochondrial membrane, but also in bacterial membranes, CL localization can induce a negative curvature on the membrane [158]. Further analysis of the final configurations of the CG-MD trajectories revealed that the number of residues interacting with membrane proportionally increases with increasing CL concentration (Figure 5-11 A). Furthermore, the number of CL molecules interacting with cyt-c also increases with increasing CL concentration (Figure 5-11 B). The effect is even more pronounced when considering the two CGMD simulations that overlap with distal and proximal binding sites and the CGMD simulation the overlaps with the third binding site separately (Figure 5-11 B). In the latter, the number of CL molecules interacting with cyt-c is significantly smaller (6 versus 14 and 15) and the membrane is not curved. This finding strongly suggests that the engagement of cyt-c's third binding site with the membrane is an unproductive one.

5.5.2.4 Comparison with Experimental Results

The modeling data were compared with the solution NMR data of CL binding to cyt-c. The experiments were performed either by maintaining the same molar ratio between TOCL and DOPC in phosphate buffer at pH 6 or the same total lipid concentration in Hepes buffer at pH 7.4. The gradual decrease in signal intensity as a result of TOCL binding at pH 6 predominantly affects the distal and proximal sides of the heme, but then also extends to the left and right sides. The Hepes pH 7.4 conditions result in an earlier disappearance of all peaks (complete disappearance of all peaks at ratio 1:5 in Hepes pH 7.4 as opposed to 1:6 in phosphate pH 6), which means that cyt-c is fully attached to the large liposomes which do not tumble sufficiently fast on the NMR time scale to allow peak detection.

Additionally, the initial rate of substrate oxidation measured by fluorescence spectroscopy in Hepes buffer at pH 7.4 and phosphate buffer at pH 6 (in correspondence with the NMR studies). The activity measurement in line with NMR and modeling studies confirmed that higher ratios of CL/cyt-c lead to strong interactions and consequently higher peroxidase activity.

5.5.2.5 Discussion and conclusion of interactions of CL and cyt-c

The initiation and formation of the cyt-c/CL complex, which leads to cyt-c conformational changes and peroxidase activity of cyt-c is pivotal for its role in the early stages of apoptosis. The nature of binding of CL to cyt-c, including affinity, stoichiometry and location of binding sites remains unclear despite numerous studies [125, 131, 132, 140, 143, 159-161]. Emphasis has been on the electrostatic interactions between negatively charged phosphate groups on CL and positively charged residues on cyt-c and it was proposed that these electrostatic interactions initiate the formation of the complex. It was proposed that only subsequent to electrostatic attraction, hydrophobic and hydrogen bonding interactions between cyt-c and the acyl chains develop and ensure the tight binding of cyt-c to anionic phospholipids [118, 125, 131, 132, 160]. It has also been argued that this second stage tight binding is the major cause of partially unfolding the protein [162, 163]. A number of experiments exhibit bi-phasic characteristics. It was therefore tempting to speculate that a 2-step process comprising electrostatic interaction in step 1 followed by hydrophobic interaction in step 2 is responsible [121, 136, 159, 164]. The two-step models, however, are not able to explain the observation of multiple binding sites and the details of the interactions are controversial.

To better understand the interplay of different binding sites and multiple modes of binding proposed previously, we used molecular modeling —in complement to available NMR data— to study the cyt-c/CL interaction and conformational heterogeneity of cyt-c structure.

Molecular docking identified three possible locations for the interaction of CL with cyt-c, and available NMR spectroscopy data provides evidence that all of these sites are actually engaged. How can this be possible given the locations on opposite ends of the protein? The answer lies in the fact that the interaction of cyt-c with CL has to be seen in the context of the membrane. Our CGMD and OPM say that the two binding sites identified by docking are actually one when considering the extended size of the membrane and availability of multiple CL molecules within and that cyt-c embeds partially into the membrane.

The simulation further supports the notion that both, electrostatics and hydrophobic forces combined lead to form a tight CL/cyt-c complex and we no longer need to assume a two-step process as in prior models. The ability to bind cyt-c simultaneously at two opposing ends of the heme provides a natural path to formation of the peroxidase by opening the heme crevice through "pulling" by the membrane. We thus consider the simultaneous occupation of the distal and proximal sites as "productive" binding. We cannot distinguish if membrane curvature enhances binding of CL to cyt-c in this manner, or if the strain imposed on the membrane by binding is the driving factor for curvature formation. Either way, our results support a model in which cyt-c is partially and stably embedded in a locally curved and CL-rich membrane patch.

We propose that one bound state is the productive binding at proximal and distal sites and that the other bound state is the unproductive binding at the third site. The available solution NMR results indicate that all binding sites are engaged. Due to the nature of the measurements it is not possible to quantify the relative ratio of the two modes of binding at this time.

The CGMD results are also in good agreement with the NMR and fluorescence results respect to the ratio of CL needed to create a peroxidase. Increasing the CL concentration enhances the affinity of cyt-c for the membrane. Remarkably, cyt-c recruits CL to form a cluster

in the membrane, which demonstrates that multiple CL molecules (not one alone) stabilize the cyt-c/CL complex.

Taking together the conformational studies of cyt-c and interaction studies with CL, we propose that gain of peroxidase activity by the cyt-c/CL complex is not a small molecule induced effect, but rather is mediated by the interaction with the extensive surface area involved in binding the CL containing membrane bilayer. This has important biological implications for modulating cyt-c peroxidase activity. The extensive surface area formed between CL and cyt-c is reminiscent of protein-protein interaction interfaces and the inherent conformational flexibility of cyt-c identified by the NMR relaxation measurements is crucial for enabling this interaction.

5.5.3 Computational Studies if CL-signaling in mitophagy

Two types of macroautophagy have been identified so far, nonselective and cargo-specific autophagy. Nonselective autophagy occurs on nutrient deficiency to supply cells with essential metabolic building blocks to the point that nutrients can be gained again from the extracellular environment. Cargo-specific autophagy occurs during nutrient-rich conditions to mediate the removal of redundant or injured organelles and protein aggregates, which could be toxic [165].

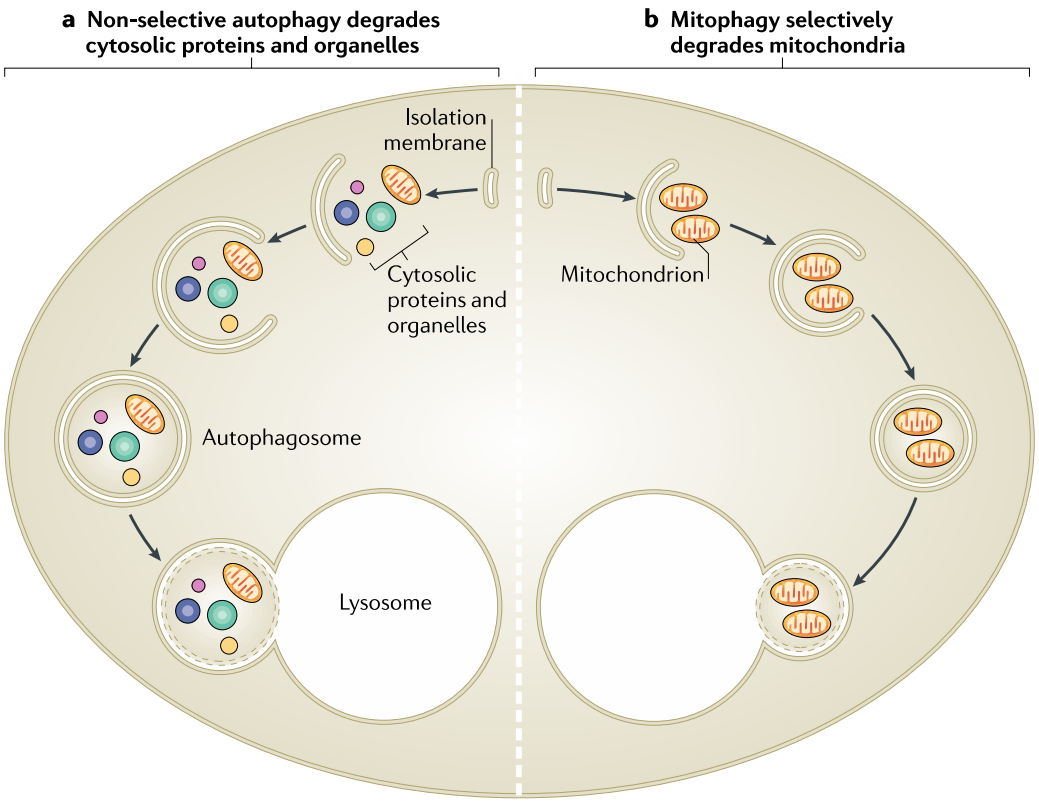

Figure 5-12 Two different autophagy pathways

a. non-selective autophagy occurs when cells are deprived of nutrients, and **b.** cargo-specific autophagy that includes mitophagy occurs to eliminate mitochondria, either to regulate their number or to specifically remove damaged mitochondria (adapted from [165]).

Mitophagy is a well-studied type of cargo-specific autophagy to remove mitochondria selectively (Figure 5-12) [165]. Mitophagy was coined by Lemasters and colleagues [166] to describe the engulfment of mitochondria into vesicles that are coated with the autophagosome marker MAPI light chain 3 (LC3; a homologue of yeast Atg8). This process can occur within ~5 minutes [165]. LC3 (mammalian homologue of yeast Atg8) is an ubiquitin-like protein that is covalently attached to phosphatidylethanolamine (PE) during autophagosome biogenesis. LC3 integrates into autophagosome, helps the growing isolation membrane and participates in cargo recruitment [167]. However, the details of how mitochondrial damage can induce mitophagy remains to be

elucidated. Mitophagy is a quality control stage for the damaged mitochondrial material for selective removal. Moreover, mitophagy is required for steady-state turnover of mitochondria to adjust mitochondrion numbers, according to cell demands [168].

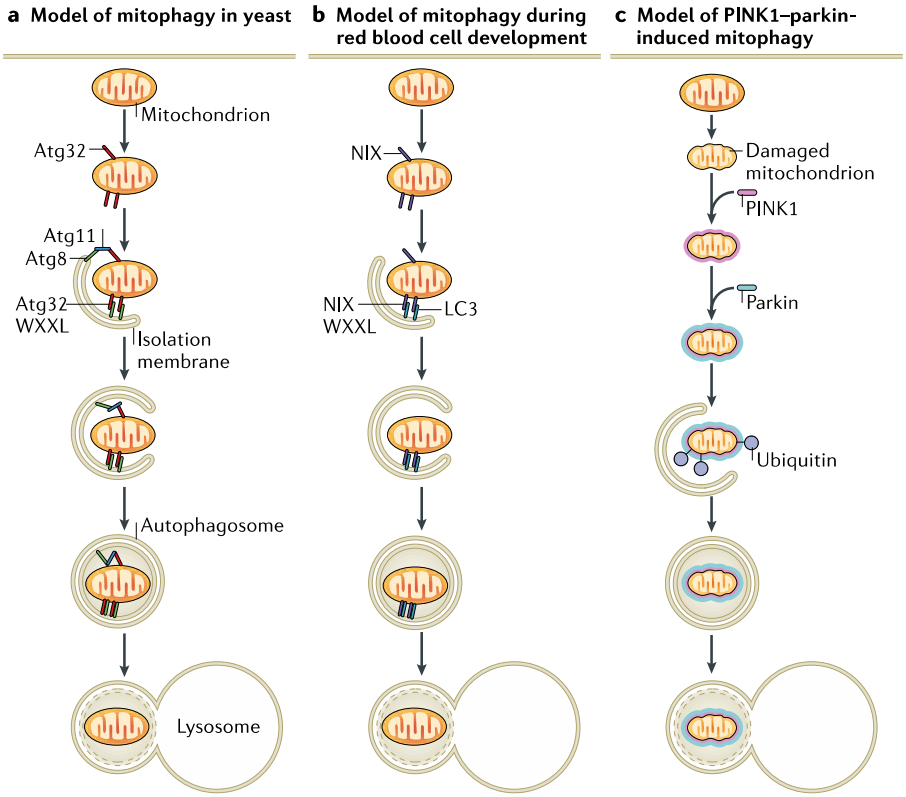

Figure 5-13 The mechanisms of mitophagy.

a. In yeast this occurs through OMM protein autophagy-related 32 (Atg32). **b.** Red blood cells, during differentiation, lose their mitochondria through mitophagy. NIX has a WXXL-like motif, which binds to LC3 and sequestration of mitochondria into autophagosomes. **c.** For the damaged mitochondrion, the kinase PTEN-induced putative kinase protein 1 (PINK1) accumulates, and recruits the E3 ubiquitin ligase parkin from the cytosol. Parkin ubiquitylates mitochondrial proteins to induce mitophagy. This may mediate mitochondrial quality control (adapted from [165]).

Three mechanisms had been proposed for mitophagy (Figure 5-13) until Chu and co-workers describe a novel mechanism for autophagy [165]. They suggested that the binding of the externalized CLs —on the surface of a damaged mitochondrion— with LC3 act as an ‘‘eat-me’’ signal for mitophagy. With regard to specificity of CL involvement in the signaling process, two points should be noted: (i) enrichment of the OMM with CLs is associated with the random trans-membrane translocation of different CL species, and (ii) externalized CLs do not contain increased amounts of oxidized CL species [28].

Here, we employed computational methods to explore the mechanism of interactions of LC3/CL. The modeling data were leveraged to study CL-binding sites of LC3 to propose the key residues/domain involve in CL interactions. Moreover, the effect of LC3 interactions on CL-containing membrane was identified. Our modeling data have been validated using experimental data and full atomistic simulations.

5.5.3.1 LC3 structure and its conserved residues

Although mechanisms of selective autophagy are just beginning to emerge [169, 170], LC3 serves as a receptor for cargo adapters that bind protein aggregates [171], and its homolog Atg8 functions in an analogous role in yeast [172]. Examination of the crystal structure of LC3 reveals basic patches at its surface that are not present in the related proteins GABARAP and GATE16 (Figure 5-14) [173].

A total of 10 sequences corresponding to the LC3 family corresponding to isoforms (A, B and C) were downloaded from SwissProt using the criteria “((gene:MAP1LC3A OR gene:MAP1LC3B OR gene:MAP1LC3C))”.

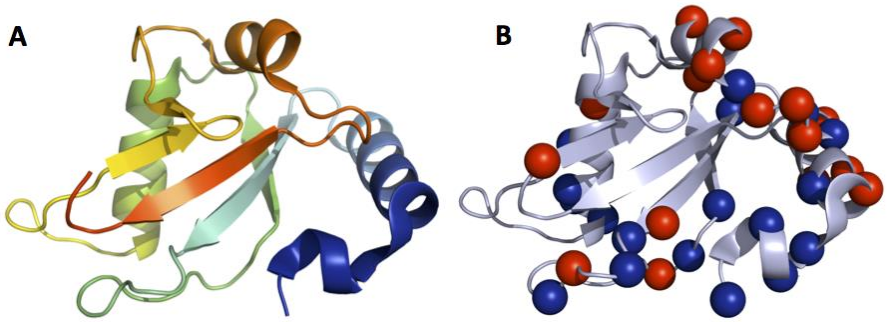

Figure 5-14 LC3 structure.

A. Rat LC3-B structure based on PDB ID: 1UGM. B. Positively (blue) and negatively (red) charged residues of LC3 —spheres represent the Cα atom of each amino acid.

The sequence alignment and phylogram of those 10 sequences using ClustalW illustrated in Figure 5-15.

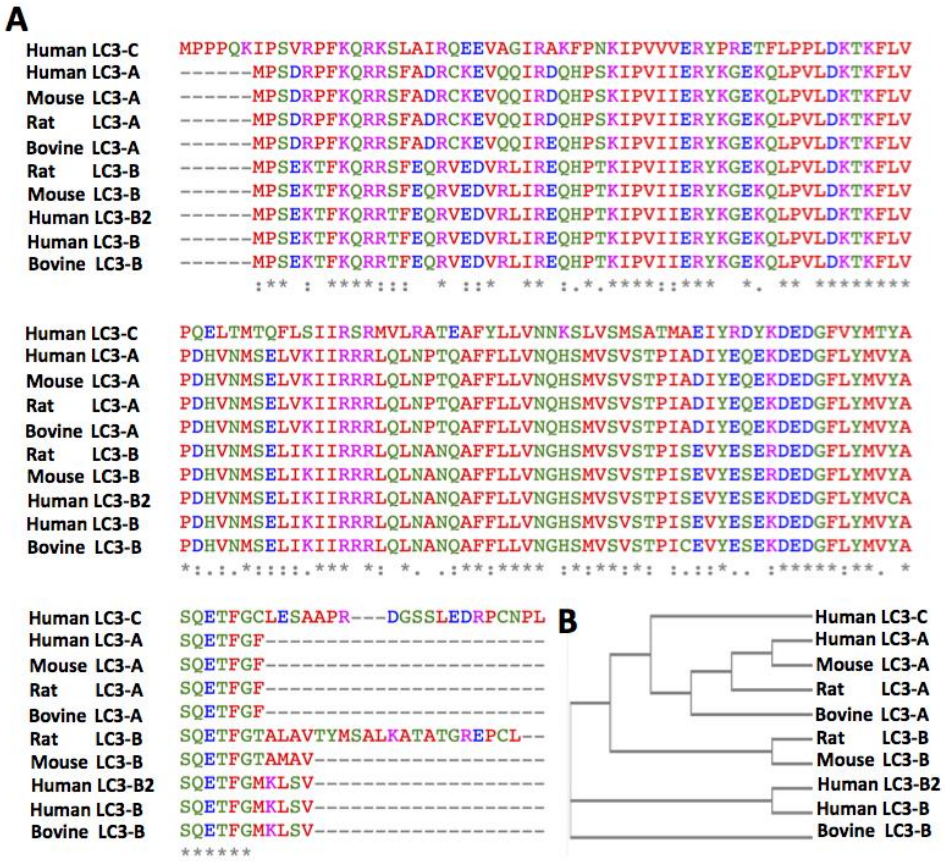

Figure 5-15 A. The sequence alignment and B. phylogram of 10 LC3 homologues using ClustalW.

5.5.3.2 Predicting CL-binding site on LC3 using molecular modeling

Molecular docking analysis predicts two CL-binding pockets at the rat LC3-B surface (Figure 5-16 A).

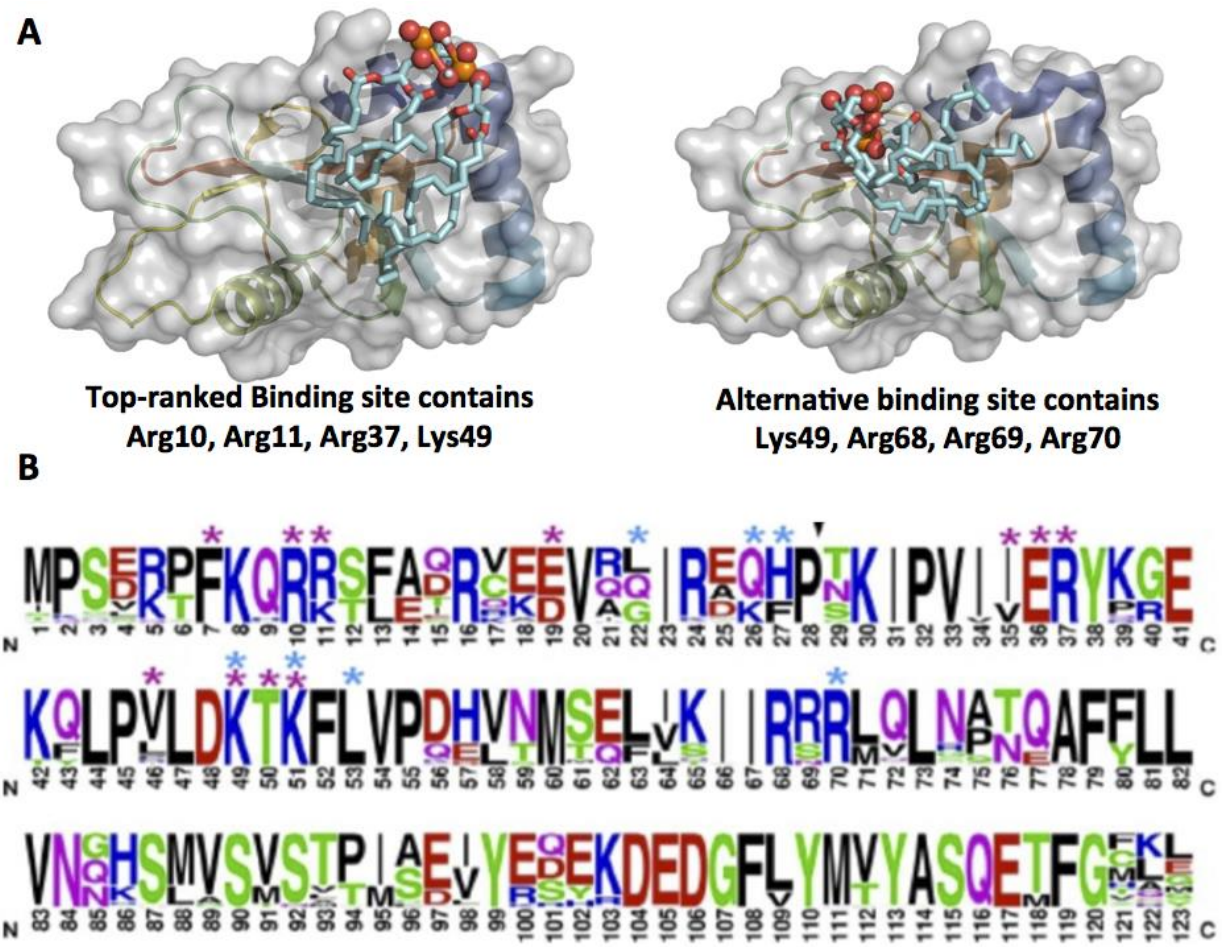

Figure 5-16 CL-binding site of LC3.

A. Molecular model of interaction sites for CL binding to LC3 by docking analysis, left is the top-ranked and right is the alternative binding site. Representation guide: CL acyl chains are colored cyan, and phosphate groups in orange. Surface and cartoon representation of LC3 are merged. **B.** Thirty-nine LC3 family sequences including isoforms A-C were aligned with ClustalW and displayed using WebLogo, with symbol heights corresponding to relative amino acid frequency. Asterisks denote residues that contact CL in the favored (magenta) and alternate conformations (cyan).

On both binding sites, there are positively charged residues interacting with the sterically-constrained head group of CL to stabilized electrostatic interactions. The predicted coordinating amino acids, which displayed using WebLogo (Figure 5-16 B), include N-terminal alpha-helical residues of LC3, which are highly conserved (Figure 5-15). According to molecular docking data we hypothesized that, the electrostatic interactions of CLs phosphate groups with a cluster of critical arginine residues of LC3 define the recognition process [21], which has been tested using experimental data. Two types of experiments validated that N-terminal residues of LC3 is highly involved in CL interactions, i. deleting N-terminus of LC3 and ii. double mutating LC3 at R10 and R11 prevented the injury-induced increase in co-localization with mitochondria.

5.5.3.3 Interactions of LC3 with CL-containing membrane

To supplement the molecular docking predictions of CL-binding pockets at the LC3 surface, facilitating identification of key residues for mutagenesis, we used molecular dynamics to simulate the binding of human LC3B to PC bilayer membranes containing CL or PA. Three independent CGMD simulations of 1 μs each were performed, using different initial velocities during equilibration to generate different LC3 orientation versus membrane. In all three runs, LC3, originally placed ~20 Å away from the bilayer surface, reoriented and translocated towards the bilayer surface to rapidly interact with CL —four snapshots of CGMD1 demonstrated in Figure 5-17 as a typical interactions trajectory. The significant displacement of LC3 was driven by strong electrostatic interactions between the negatively charged CL head groups and positively charged residues on LC3. The overall comparison of the interactions of LC3 with the lipid bilayer in the presence or absence of CL suggests that the presence of CL facilitates more rapid diffusion towards bilayers followed by stronger interactions.

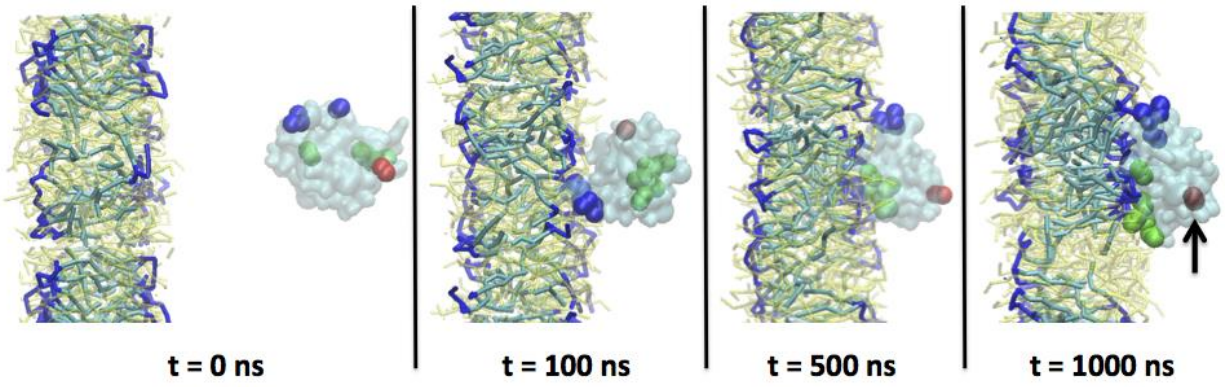

Figure 5-17 Interactions of CL-containing membrane and LC3. CGMD simulations suggest that LC3 triggers lateral diffusion of CL and its clustering in the membrane.

The curvature formation caused by protein binding emphasizes the strong interactions. Initial configuration (t = 0 ns) LC3 was placed ~2 nm away from the membrane; Final configuration (t = 1000 ns) LC3 is interacting with CL-containing membrane. Color guide: head groups of CL, dark blue sticks; acyl chain of CL, light blue sticks; LC3, cyan (transparent); N-terminus of LC3 (K5, R10-R11), blue spheres; K49, R68-R69-R70, green spheres; Glu117, red sphere. Black arrow shows Glu117 —representing C-terminus of LC3, which stays exposed to the water to play the cross-linker role.

The three CGMD simulations indicated the involvement of residues K5, R10 and R11 in the initial interactions with the CL-containing bilayer, with recruitment of residues R68-R70 and K49 (Table 5-4).

Although the simulations are likely to provide insights into early recognition events rather than thermodynamically stable binding conformations, CGMD simulations implicated residues in two regions - K5, R10-R11 and R68-R70 – in early interactions of LC3 with CL containing membranes. Notably, the C-terminal region of LC3, which becomes cross-linked to autophagosome membranes, remained exposed throughout the simulation (Figure 5-17 the right panel), compatible with its proposed bridging role.

Table 5-4 Residues of LC3 in contact with CL during CGMD simulation.

The first contact involves N-terminal residues F7-K8-Q9-R10-R11 [Note overlap with the favored docked conformation of F7-R10-R11]. These residues stay in contact throughout the rest of the simulation. While additional electrostatic interactions form subsequently, a hydrophobic contribution develops through involvement of V33-I34-V46-F52-L53-I67 at 100ns, which is further expanded with the addition of V17-V20- L22-I31-I35-Y38-L47-V54-I64-I66-L71-F79-F80-L82-L83-I95-F108-Y110 at 150ns. A distance of < 5Å was used to identify interacting molecules Bold: residues that contact the bilayer after 50ns. Underlined: residues in contact after 100ns.

Time (ns)	Residues	Number of Residues
40	--	0
50	**F7-K8-Q9-R10-R11**	5
100	K5-**F7-Q9-R10-R11**-E14-H27-T29-K30-P32-V33-I34-R37-P45-V46-K49-T50-F52-L53-I67-R68	21
150	**F7-Q9-R10-R11**-V17-V20-R21-L22-H27-T29-K30-I31-V33-I34-I35-Y38-K42-L47-K49-T50-F52-L53-V54-N59-I64-I66-R68-L71-F79-F80-L82-L83-I95-F108-Y110	35

Effect of LC3 interactions on CL-containing membrane: The strength of the interactions between LC3 and CL in a bilayer membrane is emphasized by the observed CL clustering and membrane deformation due to the binding (Figure 5-17 at time equal to 500 and 1000 ns).

CL and lysoCL vs. PA: CGMD simulations of CL- and PA-containing membranes (data are not shown) suggest that LC3 fluctuates near PA-containing bilayer surfaces, without significant movement toward the membrane. In contrast, the interaction of LC3 with the CL-containing bilayer appeared to be stabilized by recruitment of additional interaction sites, particularly for CL bearing four acyl chains. LC3 interacts with lower affinity with the membrane containing lyso-CL (CL with three acyl chains).

Experimental proof: The data were generated using a gel retardation assay demonstrated that recombinant LC3 can directly bind CL liposomes, but not PC liposomes. We also found that

LC3 interacts more favorably with CL containing four acyl chains, than with lysoCLs. Experimental data also indicates that LC3 shows a stronger affinity for CL than for phosphatidic acid (PA) and phosphatidylglycerol (PG).

Interactions of CL and Beclin 1: CL has been reported to bind several proteins, including the C-terminal domain of the autophagy protein Beclin 1 [174] and the voltage dependent anion channel, which is implicated in the FCCP-PINK1-Parkin pathway of mitophagy [175, 176]. Consistent with observations that full length Beclin 1 does not interact with membranes [174], simulations of the interaction of Beclin 1 with a lipid bilayer containing CL provided little evidence for binding (not shown). Thus, it is unlikely that this interaction contributes significantly to mitochondrial targeting to the autophagosome in these contexts.

5.5.3.4 Comparison with Experimental Results

The modeling data were compared with the double point mutation of LC3, in which either Arg 10 and Arg 11 or Gln 26 and His 27 were mutated. The Arg 10 and Arg 11 mutation fully recapitulated the effects of deleting the α-helices, preventing the injury-induced increase in co-localization with mitochondria (in line with docking and CGMD simulations) [28]. Additionally, full atomistic MD simulations revealed that the positively charged residues in N-terminal domain of LC3 are actively involved in the interactions with the CL-containing membrane [28].

5.5.3.5 Discussion and conclusions of interactions of CL and LC3

1A/1B-light chain 3 protein mediates both autophagosome formation and cargo recognition during mitophagy. However, the mechanism of recognition of injured/damaged mitochondria is not known. Since it has been known that CLs are externalized in damaged mitochondria we have

hypothesized that LC3 may recognize these CLs. To test our hypothesis we employed computational approaches (in complement with the available experimental data generated in our group) to predict CL binding site of LC3. Molecular docking analysis predicts CL-binding pockets at the LC3 surface, where Arg and Lys interact with the negative head groups of CL with two possible conformations. The predicted coordinating amino acids include N-terminal residues of LC3 such as Arg 10 and Arg 11 for the top-ranked conformation or Gln 26 and His 27 for the alternative conformation. CGMD simulations of 1,000 ns implicate Arg 10 and Arg 11 in the initial interactions of LC3 with CL-containing membranes. Then, it was experimentally validated that the truncation of the predicted CL binding domain or even mutation of the predicted key CL-binding residues impaired mitophagy process.

Molecular modeling and simulations also predicted that clustering of CL around LC3 may serve to stabilize initial electrostatic interactions, with embedding of parts of the protein into the bilayer through hydrophobic interactions. If this is correct, such a clustering mechanism could help ensure that normal transient fluctuations due to lipid transport dynamics do not trigger mitophagy until a critical threshold of LC3–CL interaction density is achieved. It is possible that in some systems, the threshold may be modulated by concurrent engagement of other cargo-targeting mechanisms.

6.0 CHAPTER 6: FUTURE DIRECTIONS

6.1 LIPID SIGNALING DUE TO OXYGENATION OF LIPIDS

6.1.1 Role of Oxygenated-Lipid-Containing Lipid Droplets in Cancer

6.1.1.1 Structural role of ox-lipids in LD

Due to limitation of computational resources and simulations time, we used a relatively small LD size compared to the actual LD dimensions in our studies. Thus, our model depicts a higher curvature and a higher surface pressure at the interface. To mitigate the size issue, a tri-layer model composed of two layers of phospholipids and a central layer of TAGs/oxTAGs can be employed in future studies. This model mimics a very large lipid droplet by ignoring the curvature. A comparison of both models, small LD and tri-layer system, will provide more accurate insight regarding the dynamics behavior of TAGs and oxTAGs. We documented the small fraction of TAGs molecules also can be redistributed into the PL monolayer, however, they are not stable there. On the other hand, oxTAG reside in PL monolayer, comparing the core, for a longer simulations time. We hypothesized that this behavior can be limited in oxTAG in tri-layer system due to elimination of the curvature effect and the surface pressure at the interface.

6.1.1.2 Role of Oxygenated-Lipid-Containing Lipid Droplets in Antigen-Cross Presentation

Our computer modeling data represented that a beta-hairpin motif in the N-terminal ATPase domain of HSP70 is actively involved in the interactions with oxygenated lipid species. In future studies, the computational and experimental approaches can be utilized to study the effect of point mutation(s) of the residues present in this motif, particularly Lys294. Mutation study can be performed using both molecular docking and CGMD.

To gain further insight regarding to chemical bond formation between HSP70 and ox-lipids, the free energy calculations based on potential mean forces (PMF) can be applied. PMF can be calculated for two systems, i. HSP70 anchored on the surface of LD without covalent bond formation (current model), ii. HSP70 anchored on the LD surface while initially a chemical bond is considered between Lys294 and an aldehyde group of a truncated TAG. Using pulling method and umbrella sampling PMF can be calculated and compared for both cases. We hypothesize that the covalent binding of Lys249 and one ox-TAG possibly introduces large barrier energy to pull HSP70 away from the surface of the LD indicating irreversibility of the interactions.

6.1.2 Mechanism of Phospholipids Peroxidation in Ferroptosis

The *in vivo* and *in vitro* experiments clearly indicated that arachidonoyl- and adrenoyl-PE are dominant biomarkers of ferroptosis cell death. However, our molecular docking data represented insignificant differences in the binding affinities for five classes of PL (from six). On the other hand CGMD simulations suggested two lipids species, including SAPE and SAPI lipids, are potentially can interact with the active site of 15LOX. In future studies, we can employ a

membrane model to investigate the specificity of 15LOX enzyme to these two lipid species. The model membrane should contain PC as a substrate and equal concentration of PE and PI lipids. Therefore, the role of these two lipids in the membrane binding behavior can be investigated. As we showed, 15LOX deeply penetrates in the membrane, which probably make the catalytic site of the enzyme accessible for the lipids embedded in the membrane (in a long enough run). Hence, we may be able to observe the interactions of either of these two types of lipids with the catalytic site.

6.2 CL- SIGNALING DUE TO COLLAPSE OF ASYMMETRY

6.2.1 Interactions of CL and Proteins

Recently, we describe the collection of the first systematic and, to the best of our knowledge, the comprehensive gold standard data set of all known CL-binding proteins. In future works, the availability of a gold standard data set can be used in combination with suitable features to develop a general classification model that can be applied at the system-wide level to predict if a given protein may interact with CL or not.

Although we have observed clear trends in binding patch properties in CL-binding proteins, in future, we can investigate the “specificity”. For example, other anionic phospholipids or even other doubly negatively charged small molecules such as GDP or ADP may show similar general structural and dynamics features in their respective binding pockets. Moreover, we can explore specificity among many CL species —using molecular modeling to predict the binding

affinities and binding sites. We hypothesize that TLCL shows higher affinity compared to CL with higher degrees of saturations or shorter chains (<18 carbons).

BIBLIOGRAPHY

1. Fahy, E., et al., *Update of the LIPID MAPS comprehensive classification system for lipids.* J Lipid Res, 2009. **50 Suppl**: p. S9-14.

2. Shevchenko, A. and K. Simons, *Lipidomics: coming to grips with lipid diversity.* Nat Rev Mol Cell Biol, 2010. **11**(8): p. 593-8.

3. Quehenberger, O., et al., *Lipidomics reveals a remarkable diversity of lipids in human plasma.* J Lipid Res, 2010. **51**(11): p. 3299-305.

4. Oresic, M., V.A. Hanninen, and A. Vidal-Puig, *Lipidomics: a new window to biomedical frontiers.* Trends Biotechnol, 2008. **26**(12): p. 647-52.

5. Bandorowicz-Pikula, J., M. Wos, and S. Pikula, *Do annexins participate in lipid messenger mediated intracellular signaling? A question revisited.* Molecular Membrane Biology, 2012. **29**(7): p. 229-242.

6. Kagan, V.E., et al., *Cardiolipin Signaling Mechanisms: Collapse of Asymmetry and Oxidation.* Antioxid Redox Signal, 2015.

7. Rothman, J.E. and J. Lenard, *Membrane asymmetry.* Science, 1977. **195**(4280): p. 743-53.

8. Fadeel, B. and D. Xue, *PS externalization: from corpse clearance to drug delivery.* Cell Death Differ, 2006. **13**(3): p. 360-2.

9. Lewis, R.N. and R.N. McElhaney, *The physicochemical properties of cardiolipin bilayers and cardiolipin-containing lipid membranes.* Biochim Biophys Acta, 2009. **1788**(10): p. 2069-79.

10. Tyurina, Y.Y., et al., *A mitochondrial pathway for biosynthesis of lipid mediators.* Nature Chemistry, 2014. **6**(6): p. 542-552.

11. Haines, T.H., *A new look at Cardiolipin.* Biochim Biophys Acta, 2009. **1788**(10): p. 1997-2002.

12. Oliver, P.M., et al., *Localization of anionic phospholipids in Escherichia coli cells.* J Bacteriol, 2014.

13. Maloney, E., et al., *Localization of acidic phospholipid cardiolipin and DnaA in mycobacteria.* Tuberculosis (Edinb), 2011. **91 Suppl 1**: p. S150-5.

14. Kagan, V.E., et al., *Cardiolipin signaling mechanisms: collapse of asymmetry and oxidation.* Antioxid Redox Signal, 2015. **22**(18): p. 1667-80.

15. Horvath, S.E. and G. Daum, *Lipids of mitochondria.* Prog Lipid Res, 2013. **52**(4): p. 590-614.

16. Kozjak-Pavlovic, V., K. Ross, and T. Rudel, *Import of bacterial pathogenicity factors into mitochondria.* Curr Opin Microbiol, 2008. **11**(1): p. 9-14.

17. Curtis, M.M. and V. Sperandio, *A complex relationship: the interaction among symbiotic microbes, invading pathogens, and their mammalian host.* Mucosal Immunol, 2011. **4**(2): p. 133-8.

18. Gold, V.A., et al., *The action of cardiolipin on the bacterial translocon.* Proc Natl Acad Sci U S A, 2010. **107**(22): p. 10044-9.

19. Arechaga, I., *Membrane invaginations in bacteria and mitochondria: common features and evolutionary scenarios.* J Mol Microbiol Biotechnol, 2013. **23**(1-2): p. 13-23.

20. Dalebroux, Z.D., et al., *PhoPQ regulates acidic glycerophospholipid content of the Salmonella Typhimurium outer membrane.* Proc Natl Acad Sci U S A, 2014. **111**(5): p. 1963-8.

21. Kagan, V.E., et al., *Cardiolipin asymmetry, oxidation and signaling.* Chem Phys Lipids, 2014. **179**: p. 64-9.

22. Greenberg, M.E., et al., *The lipid whisker model of the structure of oxidized cell membranes.* J Biol Chem, 2008. **283**(4): p. 2385-96.

23. Herber, D.L., et al., *Lipid accumulation and dendritic cell dysfunction in cancer.* Nat Med, 2010. **16**(8): p. 880-6.

24. Ramakrishnan, R., et al., *Oxidized lipids block antigen cross-presentation by dendritic cells in cancer.* J Immunol, 2014. **192**(6): p. 2920-31.

25. Friedmann Angeli, J.P., et al., *Inactivation of the ferroptosis regulator Gpx4 triggers acute renal failure in a therapeutically relevant mechanism.* Nat Cell Biol, 2014. **in press**.

26. Schlattner, U., et al., *Dual function of mitochondrial Nm23-H4 protein in phosphotransfer and intermembrane lipid transfer: a cardiolipin-dependent switch.* J Biol Chem, 2013. **288**(1): p. 111-21.

27. Gottlieb, E., et al., *Mitochondrial membrane potential regulates matrix configuration and cytochrome c release during apoptosis.* Cell Death Differ, 2003. **10**(6): p. 709-17.

28. Chu, C.T., et al., *Cardiolipin externalization to the outer mitochondrial membrane acts as an elimination signal for mitophagy in neuronal cells.* Nat Cell Biol, 2013. **15**(10): p. 1197-205.

29. Kobe, M.J., et al., *The structure of human 15-lipoxygenase-2 with a substrate mimic.* J Biol Chem, 2014. **289**(12): p. 8562-9.

30. Trott, O. and A.J. Olson, *AutoDock Vina: improving the speed and accuracy of docking with a new scoring function, efficient optimization, and multithreading.* J Comput Chem, 2010. **31**(2): p. 455-61.

31. Morris, G.M., et al., *AutoDock4 and AutoDockTools4: Automated docking with selective receptor flexibility.* J Comput Chem, 2009. **30**(16): p. 2785-91.

32. *The PyMOL Molecular Graphics System, Version 1.5.0.4 Schrödinger, LLC.*

33. *Proteins in Solution and at interfaces*. 2013: John Wiley and Sons.

34. Ingolfsson, H.I., et al., *The power of coarse graining in biomolecular simulations.* Wiley Interdiscip Rev Comput Mol Sci, 2014. **4**(3): p. 225-248.

35. Essmann, U., et al., *A smooth particle mesh Ewald method.* The Journal of Chemical Physics, 1995. **103**(19): p. 8577.

36. Evans, D.J. and B.L. Holian, *The Nose–Hoover thermostat.* The Journal of Chemical Physics, 1985. **83**(8): p. 4069.

37. Berendsen, H.J.C., et al., *Molecular-Dynamics with Coupling to an External Bath.* Journal of Chemical Physics, 1984. **81**(8): p. 3684-3690.

38. Marrink, S.J., et al., *The MARTINI force field: coarse grained model for biomolecular simulations.* J Phys Chem B, 2007. **111**(27): p. 7812-24.

39. Lopez, C.A., et al., *Martini Force Field Parameters for Glycolipids.* J Chem Theory Comput, 2013. **9**(3): p. 1694-708.

40. Monticelli, L., et al., *The MARTINI Coarse-Grained Force Field: Extension to Proteins.* J Chem Theory Comput, 2008. **4**(5): p. 819-34.

41. Periole, X., et al., *Combining an Elastic Network With a Coarse-Grained Molecular Force Field: Structure, Dynamics, and Intermolecular Recognition.* J Chem Theory Comput, 2009. **5**(9): p. 2531-43.

42. Uusitalo, J.J., et al., *Martini Coarse-Grained Force Field: Extension to DNA.* J Chem Theory Comput, 2015. **11**(8): p. 3932-45.

43. Lai, K., et al., *Computer simulation study of nanoparticle interaction with a lipid membrane under mechanical stress.* Phys Chem Chem Phys, 2013. **15**(1): p. 270-8.

44. Martinez, L., et al., *PACKMOL: a package for building initial configurations for molecular dynamics simulations.* J Comput Chem, 2009. **30**(13): p. 2157-64.

45. Humphrey, W., A. Dalke, and K. Schulten, *VMD: Visual molecular dynamics.* Journal of Molecular Graphics & Modelling, 1996. **14**(1): p. 33-38.

46. Cao, W.R., R.; Tuyrin, V.A.; Veglia, F.; Condamine, T.; Amoscato, A.; Mohammadyani, D.; Johnson, J.J.; Zhang, L.M.; Klein-Seetharaman, J.; Celis, E.; Kagan, V.E.; Gabrilovich, D.I., *Oxidized lipids block antigen cross-presentation by dendritic cells in cancer.* The Journal of Immunology, 2014. **In Press**.

47. Walther, T.C., Farese Jr., R. V., *Lipid Droplets and Cellular Lipid Metabolism* Annual Review of Biochemistry, 2012. **81**: p. 687-714.

48. Cabodevilla, A.G., et al., *Cell survival during complete nutrient deprivation depends on lipid droplet-fueled beta-oxidation of fatty acids.* J Biol Chem, 2013. **288**(39): p. 27777-88.

49. Reue, K., *A thematic review series: lipid droplet storage and metabolism: from yeast to man.* J Lipid Res, 2011. **52**(11): p. 1865-8.

50. Shi, X., et al., *Regulation of lipid droplet size and phospholipid composition by stearoyl-CoA desaturase.* J Lipid Res, 2013. **54**(9): p. 2504-14.

51. Kuramoto, K., et al., *Perilipin 5, a lipid droplet-binding protein, protects heart from oxidative burden by sequestering fatty acid from excessive oxidation.* J Biol Chem, 2012. **287**(28): p. 23852-63.

52. Saka, H.A. and R. Valdivia, *Emerging roles for lipid droplets in immunity and host-pathogen interactions.* Annu Rev Cell Dev Biol, 2012. **28**: p. 411-37.

53. Murphy, S., S. Martin, and R.G. Parton, *Lipid droplet-organelle interactions; sharing the fats.* Biochim Biophys Acta, 2009. **1791**(6): p. 441-7.

54. Tobin, K.A., et al., *Long-chain polyunsaturated fatty acid transport across human placental choriocarcinoma (BeWo) cells.* Placenta, 2009. **30**(1): p. 41-7.

55. Girotti, A.W., *Lipid hydroperoxide generation, turnover, and effector action in biological systems.* J Lipid Res, 1998. **39**(8): p. 1529-42.

56. Biron-Shental, T., et al., *Hypoxia regulates the expression of fatty acid-binding proteins in primary term human trophoblasts.* Am J Obstet Gynecol, 2007. **197**(5): p. 516 e1-6.

57. Kato, Y., et al., *HSP70 and HSP90 Differentially Regulate Translocation of Extracellular Antigen to the Cytosol for Cross-Presentation.* Autoimmune Dis, 2012. **2012**: p. 745962.

58. Penno, A., Hackenbroich, G., Thiele, C., *Phospholipids and lipid droplets.* Biochimica et Biophysica Acta, 2013. **1831**: p. 589–594.

59. Bertelsen, E.B., et al., *Solution conformation of wild-type E. coli Hsp70 (DnaK) chaperone complexed with ADP and substrate.* Proc Natl Acad Sci U S A, 2009. **106**(21): p. 8471-6.

60. Boratyn, G.M., et al., *BLAST: a more efficient report with usability improvements.* Nucleic Acids Research, 2013. **41**(W1): p. W29-W33.

61. Periole, X., et al., *Combining an Elastic Network With a Coarse-Grained Molecular Force Field: Structure, Dynamics, and Intermolecular Recognition.* Journal of Chemical Theory and Computation, 2009. **5**(9): p. 2531-2543.

62. Vuorela, T., et al., *Role of lipids in spheroidal high density lipoproteins.* PLoS Comput Biol, 2010. **6**(10): p. e1000964.

63. Koivuniemi, A., et al., *Lipid exchange mechanism of the cholesteryl ester transfer protein clarified by atomistic and coarse-grained simulations.* PLoS Comput Biol, 2012. **8**(1): p. e1002299.

64. Catte, A., et al., *Structure of spheroidal HDL particles revealed by combined atomistic and coarse-grained simulations.* Biophys J, 2008. **94**(6): p. 2306-19.

65. Mohammadyani, D., et al., *Molecular speciation and dynamics of oxidized triacylglycerols in lipid droplets: Mass spectrometry and coarse-grained simulations.* Free Radic Biol Med, 2014. **76**: p. 53-60.

66. Butterfield, D.A., et al., *Mass spectrometry and redox proteomics: applications in disease.* Mass Spectrom Rev, 2014. **33**(4): p. 277-301.

67. Tyurin, V.A., et al., *Mass-spectrometric characterization of peroxidized and hydrolyzed lipids in plasma and dendritic cells of tumor-bearing animals.* Biochem Biophys Res Commun, 2011. **413**(1): p. 149-53.

68. Kimmel, A.R. and C. Sztalryd, *Perilipin 5, a lipid droplet protein adapted to mitochondrial energy utilization.* Curr Opin Lipidol, 2014.

69. Thiam, A.R., R.V. Farese, Jr., and T.C. Walther, *The biophysics and cell biology of lipid droplets.* Nat Rev Mol Cell Biol, 2013. **14**(12): p. 775-86.

70. Wong-Ekkabut, J., et al., *Effect of lipid peroxidation on the properties of lipid bilayers: a molecular dynamics study.* Biophys J, 2007. **93**(12): p. 4225-36.

71. Walther, T.C., Farese Jr., R. V. , *The life of lipid droplets.* Biochimica et Biophysica Acta 2009. **1791**: p. 459-466.

72. Walther, T.C. and R.V. Farese, Jr., *The life of lipid droplets.* Biochim Biophys Acta, 2009. **1791**(6): p. 459-66.

73. Schild, R.L., et al., *The activity of PPAR gamma in primary human trophoblasts is enhanced by oxidized lipids.* J Clin Endocrinol Metab, 2002. **87**(3): p. 1105-10.

74. Radner, F.P., et al., *Growth retardation, impaired triacylglycerol catabolism, hepatic steatosis, and lethal skin barrier defect in mice lacking comparative gene identification-58 (CGI-58).* J Biol Chem, 2010. **285**(10): p. 7300-11.

75. Ren, R., et al., *A lipid peroxidation product 9-oxononanoic acid induces phospholipase A2 activity and thromboxane A2 production in human blood.* J Clin Biochem Nutr, 2013. **52**(3): p. 228-33.

76. Dixon, S.J., et al., *Ferroptosis: an iron-dependent form of nonapoptotic cell death.* Cell, 2012. **149**(5): p. 1060-72.

77. Allocati, N., et al., *Die for the community: an overview of programmed cell death in bacteria.* Cell Death Dis, 2015. **6**: p. e1609.

78. Linkermann, A., et al., *Regulated cell death and inflammation: an auto-amplification loop causes organ failure.* Nat Rev Immunol, 2014. **14**(11): p. 759-67.

79. Byrne, J.M., et al., *Redox cycling of Fe(II) and Fe(III) in magnetite by Fe-metabolizing bacteria.* Science, 2015. **347**(6229): p. 1473-6.

80. Yang, W.S. and B.R. Stockwell, *Ferroptosis: Death by Lipid Peroxidation.* Trends Cell Biol, 2015.

81. Friedmann Angeli, J.P., et al., *Inactivation of the ferroptosis regulator Gpx4 triggers acute renal failure in mice.* Nat Cell Biol, 2014. **16**(12): p. 1180-91.

82. Yang, W.S., et al., *Regulation of ferroptotic cancer cell death by GPX4.* Cell, 2014. **156**(1-2): p. 317-31.

83. Dixon, S.J., et al., *Human Haploid Cell Genetics Reveals Roles for Lipid Metabolism Genes in Nonapoptotic Cell Death.* ACS Chem Biol, 2015. **10**(7): p. 1604-9.

84. Brash, A.R., *Lipoxygenases: occurrence, functions, catalysis, and acquisition of substrate.* J Biol Chem, 1999. **274**(34): p. 23679-82.

85. Xu, S., et al., *Crystal structure of 12-lipoxygenase catalytic-domain-inhibitor complex identifies a substrate-binding channel for catalysis.* Structure, 2012. **20**(9): p. 1490-7.

86. Yamamoto, S., *Mammalian lipoxygenases: molecular structures and functions.* Biochim Biophys Acta, 1992. **1128**(2-3): p. 117-31.

87. Bushnell, E.A., R. Jamil, and J.W. Gauld, *Gaining insight into the chemistry of lipoxygenases: a computational investigation into the catalytic mechanism of (8R)-lipoxygenase.* J Biol Inorg Chem, 2013. **18**(3): p. 343-55.

88. Madden, T.L., R.L. Tatusov, and J. Zhang, *Applications of network BLAST server.* Methods Enzymol, 1996. **266**: p. 131-41.

89. Krissinel, E. and K. Henrick, *Secondary-structure matching (SSM), a new tool for fast protein structure alignment in three dimensions.* Acta Crystallogr D Biol Crystallogr, 2004. **60**(Pt 12 Pt 1): p. 2256-68.

90. Kuhn, H. and V.B. O'Donnell, *Inflammation and immune regulation by 12/15-lipoxygenases.* Prog Lipid Res, 2006. **45**(4): p. 334-56.

91. Newcomer, M.E. and A.R. Brash, *The structural basis for specificity in lipoxygenase catalysis.* Protein Sci, 2015. **24**(3): p. 298-309.

92. van Meer, G., D.R. Voelker, and G.W. Feigenson, *Membrane lipids: where they are and how they behave.* Nat Rev Mol Cell Biol, 2008. **9**(2): p. 112-24.

93. Lu, P., et al., *Mechanism-based inhibition of human liver microsomal cytochrome P450 1A2 by zileuton, a 5-lipoxygenase inhibitor.* Drug Metab Dispos, 2003. **31**(11): p. 1352-60.

94. Bocan, T.M., et al., *A specific 15-lipoxygenase inhibitor limits the progression and monocyte-macrophage enrichment of hypercholesterolemia-induced atherosclerosis in the rabbit.* Atherosclerosis, 1998. **136**(2): p. 203-16.

95. Song, L., et al., *Inhibition of 12/15 lipoxygenase by baicalein reduces myocardial ischemia/reperfusion injury via modulation of multiple signaling pathways.* Apoptosis, 2014. **19**(4): p. 567-80.

96. Hsieh, C.J., et al., *Baicalein inhibits IL-1beta- and TNF-alpha-induced inflammatory cytokine production from human mast cells via regulation of the NF-kappaB pathway.* Clin Mol Allergy, 2007. **5**: p. 5.

97. Rouzer, C.A., et al., *MK886, a potent and specific leukotriene biosynthesis inhibitor blocks and reverses the membrane association of 5-lipoxygenase in ionophore-challenged leukocytes.* J Biol Chem, 1990. **265**(3): p. 1436-42.

98. Fan, X.M., et al., *Five-lipoxygenase-activating protein inhibitor MK-886 induces apoptosis in gastric cancer through upregulation of p27kip1 and bax.* J Gastroenterol Hepatol, 2004. **19**(1): p. 31-7.

99. Linkermann, A., et al., *Synchronized renal tubular cell death involves ferroptosis.* Proc Natl Acad Sci U S A, 2014. **111**(47): p. 16836-41.

100. Khanna, S., et al., *Molecular basis of vitamin E action: tocotrienol modulates 12-lipoxygenase, a key mediator of glutamate-induced neurodegeneration.* J Biol Chem, 2003. **278**(44): p. 43508-15.

101. Jiang, Q., *Natural forms of vitamin E: metabolism, antioxidant, and anti-inflammatory activities and their role in disease prevention and therapy.* Free Radic Biol Med, 2014. **72**: p. 76-90.

102. Lebold, K.M. and M.G. Traber, *Interactions between alpha-tocopherol, polyunsaturated fatty acids, and lipoxygenases during embryogenesis.* Free Radic Biol Med, 2014. **66**: p. 13-9.

103. Kagan, V.E., et al., *Cytochrome c acts as a cardiolipin oxygenase required for release of proapoptotic factors.* Nat Chem Biol, 2005. **1**(4): p. 223-32.

104. Schlame, M., *Cardiolipin remodeling and the function of tafazzin.* Biochim Biophys Acta, 2013. **1831**(3): p. 582-8.

105. Chu, C.T., et al., *Cardiolipin externalization to the outer mitochondrial membrane acts as an elimination signal for mitophagy in neuronal cells.* Nature Cell Biology, 2013. **15**(10): p. 1197-U168.

106. Schlame, M. and M. Ren, *The role of cardiolipin in the structural organization of mitochondrial membranes.* Biochim Biophys Acta, 2009. **1788**(10): p. 2080-3.

107. Daum, G., *Lipids of mitochondria.* Biochim Biophys Acta, 1985. **822**(1): p. 1-42.

108. Schlame, M., S. Brody, and K.Y. Hostetler, *Mitochondrial cardiolipin in diverse eukaryotes. Comparison of biosynthetic reactions and molecular acyl species.* Eur J Biochem, 1993. **212**(3): p. 727-35.

109. Daum, G. and J.E. Vance, *Import of lipids into mitochondria.* Prog Lipid Res, 1997. **36**(2-3): p. 103-30.

110. Krebs, J.J., H. Hauser, and E. Carafoli, *Asymmetric distribution of phospholipids in the inner membrane of beef heart mitochondria.* J Biol Chem, 1979. **254**(12): p. 5308-16.

111. Kagan, V.E., et al., *Cytochrome c/cardiolipin relations in mitochondria: a kiss of death.* Free Radic Biol Med, 2009. **46**(11): p. 1439-53.

112. Brandt, E.G., et al., *Interpretation of fluctuation spectra in lipid bilayer simulations.* Biophys J, 2011. **100**(9): p. 2104-11.

113. Braun, A.R., et al., *Determination of electron density profiles and area from simulations of undulating membranes.* Biophys J, 2011. **100**(9): p. 2112-20.

114. Bushnell, G.W., G.V. Louie, and G.D. Brayer, *High-resolution three-dimensional structure of horse heart cytochrome c.* J Mol Biol, 1990. **214**(2): p. 585-95.

115. Lomize, M.A., et al., *OPM database and PPM web server: resources for positioning of proteins in membranes.* Nucleic Acids Res, 2012. **40**(Database issue): p. D370-6.

116. Boscia, A.L., et al., *X-ray structure, thermodynamics, elastic properties and MD simulations of cardiolipin/dimyristoylphosphatidylcholine mixed membranes.* Chemistry and Physics of Lipids, 2014. **178**: p. 1-10.

117. Godoy, L.C., et al., *Disruption of the M80-Fe ligation stimulates the translocation of cytochrome c to the cytoplasm and nucleus in nonapoptotic cells.* Proc Natl Acad Sci U S A, 2009. **106**(8): p. 2653-8.

118. Kapralov, A.A., et al., *The hierarchy of structural transitions induced in cytochrome c by anionic phospholipids determines its peroxidase activation and selective peroxidation during apoptosis in cells.* Biochemistry, 2007. **46**(49): p. 14232-44.

119. Dickerson, R.E., *The structure of cytochromec and the rates of molecular evolution.* Journal of Molecular Evolution, 1971. **1**(1): p. 26-45.

120. Kapralov, A.A., et al., *Topography of tyrosine residues and their involvement in peroxidation of polyunsaturated cardiolipin in cytochrome c/cardiolipin peroxidase complexes.* Biochim Biophys Acta, 2011.

121. Vladimirov, Y.A., et al., *Mechanism of activation of cytochrome C peroxidase activity by cardiolipin.* Biochemistry (Mosc), 2006. **71**(9): p. 989-97.

122. Sinibaldi, F., et al., *Insights into cytochrome c-cardiolipin interaction. Role played by ionic strength.* Biochemistry, 2008. **47**(26): p. 6928-35.

123. Huttemann, M., et al., *The multiple functions of cytochrome c and their regulation in life and death decisions of the mammalian cell: From respiration to apoptosis.* Mitochondrion, 2011.

124. Kadenbach, B., et al., *The possible role of cytochrome c oxidase in stress-induced apoptosis and degenerative diseases.* Biochimica et Biophysica Acta (BBA)-Bioenergetics, 2004. **1655**: p. 400-408.

125. Belikova, N.A., et al., *Peroxidase activity and structural transitions of cytochrome c bound to cardiolipin-containing membranes.* Biochemistry, 2006. **45**(15): p. 4998-5009.

126. Belikova, N.A., et al., *Heterolytic reduction of fatty acid hydroperoxides by cytochrome c/cardiolipin complexes: antioxidant function in mitochondria.* J Am Chem Soc, 2009. **131**(32): p. 11288-9.

127. Xu, Y., et al., *Remodeling of Cardiolipin by Phospholipid Transacylation.* Journal of Biological Chemistry, 2003. **278**(51): p. 51380-51385.

128. Gomez Jr, B. and N.C. Robinson, *Phospholipase digestion of bound cardiolipin reversibly inactivates bovine cytochrome bc 1.* Biochemistry, 1999. **38**(28): p. 9031-9038.

129. Zhang, M., E. Mileykovskaya, and W. Dowhan, *Cardiolipin is essential for organization of complexes III and IV into a supercomplex in intact yeast mitochondria.* Journal of Biological Chemistry, 2005. **280**(33): p. 29403.

130. Lesnefsky, E.J., et al., *Myocardial ischemia selectively depletes cardiolipin in rabbit heart subsarcolemmal mitochondria.* American Journal of Physiology-Heart and Circulatory Physiology, 2001. **280**(6): p. H2770.

131. Rytomaa, M. and P.K. Kinnunen, *Reversibility of the binding of cytochrome c to liposomes. Implications for lipid-protein interactions.* J Biol Chem, 1995. **270**(7): p. 3197-202.

132. Rytomaa, M. and P.K. Kinnunen, *Evidence for two distinct acidic phospholipid-binding sites in cytochrome c.* J Biol Chem, 1994. **269**(3): p. 1770-4.

133. Kagan, V.E., et al., *Carbon nanotubes degraded by neutrophil myeloperoxidase induce less pulmonary inflammation.* Nature Nanotechnology, 2010. **5**(5): p. 354-359.

134. Zamzami, N., et al., *Mitochondrial control of nuclear apoptosis.* The Journal of Experimental Medicine, 1996. **183**(4): p. 1533-1544.

135. Basova, L.V., et al., *Cardiolipin switch in mitochondria: shutting off the reduction of cytochrome c and turning on the peroxidase activity.* Biochemistry, 2007. **46**(11): p. 3423-34.

136. Sinibaldi, F., et al., *Extended cardiolipin anchorage to cytochrome c: a model for protein-mitochondrial membrane binding.* J Biol Inorg Chem, 2010. **15**(5): p. 689-700.

137. Muga, A., H.H. Mantsch, and W.K. Surewicz, *Membrane binding induces destabilization of cytochrome c structure.* Biochemistry, 1991. **30**(29): p. 7219-24.

138. Pinheiro, T.J., et al., *Structural and kinetic description of cytochrome c unfolding induced by the interaction with lipid vesicles.* Biochemistry, 1997. **36**(42): p. 13122-32.

139. Spooner, P.J. and A. Watts, *Reversible unfolding of cytochrome c upon interaction with cardiolipin bilayers. 2. Evidence from phosphorus-31 NMR measurements.* Biochemistry, 1991. **30**(16): p. 3880-5.

140. Zucchi, M.R., et al., *Modulation of cytochrome c spin states by lipid acyl chains: a continuous-wave electron paramagnetic resonance (CW-EPR) study of haem iron.* Biochem J, 2003. **370**(Pt 2): p. 671-8.

141. Huang, Y.Y. and T. Kimura, *Thermodynamic parameters for the reduction reaction of membrane-bound cytochrome c in comparison with those of the membrane-free form: spectropotentiostatic determination with use of an optically transparent thin-layer electrode.* Biochemistry, 1984. **23**(10): p. 2231-6.

142. Salamon, Z. and G. Tollin, *Interaction of horse heart cytochrome c with lipid bilayer membranes: effects on redox potentials.* J Bioenerg Biomembr, 1997. **29**(3): p. 211-21.

143. Tuominen, E.K., C.J. Wallace, and P.K. Kinnunen, *Phospholipid-cytochrome c interaction: evidence for the extended lipid anchorage.* J Biol Chem, 2002. **277**(11): p. 8822-6.

144. Kostrzewa, A., et al., *Membrane location of spin-labeled cytochrome c determined by paramagnetic relaxation agents.* Biochemistry, 2000. **39**(20): p. 6066-74.

145. Kawai, C., et al., *pH-Dependent interaction of cytochrome c with mitochondrial mimetic membranes: the role of an array of positively charged amino acids.* J Biol Chem, 2005. **280**(41): p. 34709-17.

146. Choi, E.J. and E.K. Dimitriadis, *Cytochrome c adsorption to supported, anionic lipid bilayers studied via atomic force microscopy.* Biophys J, 2004. **87**(5): p. 3234-41.

147. Domanov, Y.A., J.G. Molotkovsky, and G.P. Gorbenko, *Coverage-dependent changes of cytochrome c transverse location in phospholipid membranes revealed by FRET.* Biochim Biophys Acta, 2005. **1716**(1): p. 49-58.

148. Oellerich, S., et al., *Peripheral and integral binding of cytochrome c to phospholipids vesicles.* Journal of Physical Chemistry B, 2004. **108**(12): p. 3871-3878.

149. Kalanxhi, E. and C.J. Wallace, *Cytochrome c impaled: investigation of the extended lipid anchorage of a soluble protein to mitochondrial membrane models.* Biochem J, 2007. **407**(2): p. 179-87.

150. Gorbenko, G.P., J.G. Molotkovsky, and P.K. Kinnunen, *Cytochrome C interaction with cardiolipin/phosphatidylcholine model membranes: effect of cardiolipin protonation.* Biophys J, 2006. **90**(11): p. 4093-103.

151. Grimsley, G.R., J.M. Scholtz, and C.N. Pace, *A summary of the measured pK values of the ionizable groups in folded proteins.* Protein Sci, 2009. **18**(1): p. 247-51.

152. Planas-Iglesias, J., et al., *Cardiolipin Interactions with Proteins.* Biophys J, 2015. **109**(6): p. 1282-94.

153. Pecina, P., et al., *Phosphomimetic substitution of cytochrome C tyrosine 48 decreases respiration and binding to cardiolipin and abolishes ability to trigger downstream caspase activation.* Biochemistry, 2010. **49**(31): p. 6705-14.

154. Lomize, A.L., et al., *Positioning of proteins in membranes: a computational approach.* Protein Sci, 2006. **15**(6): p. 1318-33.

155. Lomize, M.A., et al., *OPM: orientations of proteins in membranes database.* Bioinformatics, 2006. **22**(5): p. 623-5.

156. Brown, L.R. and K. Wuthrich, *NMR and ESR studies of the interactions of cytochrome c with mixed cardiolipin-phosphatidylcholine vesicles.* Biochim Biophys Acta, 1977. **468**(3): p. 389-410.

157. Spooner, P.J. and A. Watts, *Cytochrome c interactions with cardiolipin in bilayers: a multinuclear magic-angle spinning NMR study.* Biochemistry, 1992. **31**(41): p. 10129-38.

158. Renner, L.D. and D.B. Weibel, *Cardiolipin microdomains localize to negatively curved regions of Escherichia coli membranes.* Proc Natl Acad Sci U S A, 2011. **108**(15): p. 6264-9.

159. Salamon, Z. and G. Tollin, *Surface plasmon resonance studies of complex formation between cytochrome c and bovine cytochrome c oxidase incorporated into a supported planar lipid bilayer. II. Binding of cytochrome c to oxidase-containing cardiolipin/phosphatidylcholine membranes.* Biophys J, 1996. **71**(2): p. 858-67.

160. Rytomaa, M., P. Mustonen, and P.K. Kinnunen, *Reversible, nonionic, and pH-dependent association of cytochrome c with cardiolipin-phosphatidylcholine liposomes.* J Biol Chem, 1992. **267**(31): p. 22243-8.

161. Stepanov, G., et al., *Evaluation of cytochrome c affinity to anionic phospholipids by means of surface plasmon resonance.* FEBS Lett, 2009. **583**(1): p. 97-100.

162. Bergstrom, C.L., et al., *Cytochrome c causes pore formation in cardiolipin-containing membranes.* Proc Natl Acad Sci U S A, 2013. **110**(16): p. 6269-74.

163. Hanske, J., et al., *Conformational properties of cardiolipin-bound cytochrome c.* Proc Natl Acad Sci U S A, 2012. **109**(1): p. 125-30.

164. Robinson, N.C., *Specificity and binding affinity of phospholipids to the high-affinity cardiolipin sites of beef heart cytochrome c oxidase.* Biochemistry, 1982. **21**(1): p. 184-188.

165. Youle, R.J. and D.P. Narendra, *Mechanisms of mitophagy.* Nat Rev Mol Cell Biol, 2011. **12**(1): p. 9-14.

166. Kim, I., S. Rodriguez-Enriquez, and J.J. Lemasters, *Selective degradation of mitochondria by mitophagy.* Arch Biochem Biophys, 2007. **462**(2): p. 245-53.

167. Mann, S.S. and J.A. Hammarback, *Molecular characterization of light chain 3. A microtubule binding subunit of MAP1A and MAP1B.* J Biol Chem, 1994. **269**(15): p. 11492-7.

168. Kissova, I., et al., *Uth1p is involved in the autophagic degradation of mitochondria.* J Biol Chem, 2004. **279**(37): p. 39068-74.

169. Narendra, D., et al., *Parkin is recruited selectively to impaired mitochondria and promotes their autophagy.* J Cell Biol, 2008. **183**(5): p. 795-803.

170. Liu, L., et al., *Mitochondrial outer-membrane protein FUNDC1 mediates hypoxia-induced mitophagy in mammalian cells.* Nat Cell Biol, 2012. **14**(2): p. 177-85.

171. Johansen, T. and T. Lamark, *Selective autophagy mediated by autophagic adapter proteins.* Autophagy, 2011. **7**(3): p. 279-96.

172. Kanki, T., et al., *Atg32 is a mitochondrial protein that confers selectivity during mitophagy.* Dev Cell, 2009. **17**(1): p. 98-109.

173. Sugawara, K., et al., *The crystal structure of microtubule-associated protein light chain 3, a mammalian homologue of Saccharomyces cerevisiae Atg8.* Genes Cells, 2004. **9**(7): p. 611-8.

174. Huang, W., et al., *Crystal structure and biochemical analyses reveal Beclin 1 as a novel membrane binding protein.* Cell Res, 2012. **22**(3): p. 473-89.

175. Sun, Y., et al., *Voltage-dependent Anion Channels (VDACs) Recruit Parkin to Defective Mitochondria to Promote Mitochondrial Autophagy.* J Biol Chem, 2012. **287**(48): p. 40652-60.

176. Geisler, S., et al., *PINK1/Parkin-mediated mitophagy is dependent on VDAC1 and p62/SQSTM1.* Nat Cell Biol, 2010. **12**(2): p. 119-31.